Honours Thesis

Research School of Astronomy and Astrophysics

The Australian National University

Characterising Variability of Galaxy Lightcurves from NASA/ATLAS Data to Search for CLAGN

Neelesh Amrutha

Supervised by A/Prof. Christian Wolf

and Dr. Christopher Onken

Submitted in part fulfilment of the requirements for the degree of Bachelor of Science (Advanced) (Honours) at the Australian National University

October 26, 2022

Acknowledgements

First and foremost, I would like to acknowledge and express deep gratitude to my supervisor Associate Professor Christian Wolf. Chris has provided immense support and guidance during my Honours year. He has been an outstanding mentor and set me on the right track for both this project and research in general. Without his close supervision this thesis would not exist.

I would like to thank my co-supervisor Dr. Christopher Onken for providing support on the technical details of my project, and for valuable ideas during our brainstorming sessions.

I would like to acknowledge Professor John Tonry for providing the lightcurve data, which is the cornerstone of my thesis. I would also like to thank PhD student Wei Jeat (Jack) Hon from University of Melbourne for allowing access to his 6dFAGN catalogue, an integral part of this project. Jack has also helped me compare and analyse spectra from different epochs.

Special thanks to PhD student Samuel Lai for observing the targets presented in this thesis at Siding Spring Observatory during the inclement weather affecting Australia in May/June. I would like to thank Chris Onken again for setting up a `PyWiFeS` pipeline and providing me with reduced data cubes.

I would also like to express my gratitude to other members of our AGN collaboration group for helping me understand more about AGN over the course of the year through our weekly discussions. I would also like to thank fellow Honours student Douglas Thompson for the joint discussions of our projects with our supervisor Chris Wolf.

Interacting with other Honours students has been a blast and has also helped me keep up with both research and coursework during my Honours year. So thank you Hank Hua, Jim Chung, Erin Holdorf, Isaac Kanowski, and Douglas Thompson, for making it an enjoyable year.

Finally, I would like to thank my family friends for always being there for me. The Honours year would not be as smooth sailing as it has been without their constant support and care.

Statement of Originality

This thesis is an account of research undertaken between February 2022 and October 2022 at The Research School of Astronomy and Astrophysics, The Australian National University, Canberra, Australia. Except where acknowledged in the customary manner, and listed below, the material presented in this thesis is, to the best of my knowledge, original and has not been submitted in whole or part for a degree in any university.

- 6dFAGN Catalogue: Catalogue of AGN types obtained from 6dFGS spectra that is yet to be published. Work of PhD student Wei Jeat (Jack) Hon from University of Melbourne in our AGN collaboration group. A description of the catalogue has been submitted (Hon, Webster & Wolf, 2022).

- ANU 2.3m Observations: Spectroscopic follow-up of selected CLAGN candidates. Observed by PhD student Samuel Lai and raw images reduced via `PyWiFeS` pipeline by my co-supervisor Dr. Christopher Onken.

<div style="text-align: right">

_____

Neelesh Amrutha

October, 2022

</div>

Abstract

Active Galactic Nuclei (AGN) have been observed increasingly over the past century. However, their origin and evolution are not well constrained. AGN are classified into different types based on the strength of broad emission lines in their spectra. Broad emission lines are expected to appear or disappear on accretion disk viscous timescales ($> 10^3$ years). Contrary to predictions, observations in the past few decades have shown that some AGN vary their broad line emissions on timescales as short as few years or months. These new Changing-look AGN (CLAGN) are a mystery partly due to their rarity. Only ~ 200 CLAGN are currently known, as large scale systematic searches involve years of monitoring AGN. In this thesis, we use NASA/ATLAS lightcurves of extragalactic sources from the past 5 years to classify variability of AGN at $z < 0.1$. We present a variability threshold that classifies AGN types based on stochastic variability of accretion luminosity. The threshold identifies variable lightcurves from a sample of AGN with 87% completeness and 77% purity. We use this classification to select 258 CLAGN candidates from a sample of 2336 AGN. We also observe 72 CLAGN candidates selected by eyeballing the lightcurves, and use spectroscopic evidence to confirm six new CLAGN. The variability threshold method recovers these CLAGN, and 15 of 19 previously known AGN within the search sample. Lightcurves of the four known CLAGN missed by the candidate selection method and one new CLAGN from this work are analysed in detail as they catch the changing look event within the lightcurve. Their lightcurves suggest a relation between accretion luminosity and AGN type assignment, implying that changing look events are continuous, short term variations in accretion. We notice a flare before turn-off events and a gradual increase in flux for turn-on events. On this basis, we provide a model for CLAGN mechanism where an event or instability destroys the innermost region of the accretion disk (turn-off event), and the gradual refilling of the innermost region restarts accretion (turn-on event). To assess the validity of the model, we require time resolved spectroscopic monitoring of a large sample of AGN, which can be made possible with upcoming surveys such as the Legacy Survey for Space and Time.

Contents

List of Figures

List of Tables

Chapter 1

Introduction

Within the cores of most massive galaxies, there lies a supermassive black hole (Marconi & Hunt, 2003). These black holes grow by accreting matter and in the process form accretion disks. Magneto-rotational instabilities (MRI) increase the viscosity of the accretion disk (Balbus & Hawley, 1991; Balbus, 2003). These viscous accretion disks are one of the most luminous and stable compact objects in the known universe. Such actively accreting entities are called Active Galactic Nuclei (AGN, singular: Active Galactic Nucleus - AGN).

AGN are detected by their luminosity, which cannot be explained by even the brightest starburst galaxies for their respective sizes. These AGN were first detected in the first half of the 20th Century. Several studies found strong emission lines at the nucleus of "spiral nebulae". But the first systematic study of emission lines was performed by Seyfert (1943). AGN were further pushed into the spotlight by the start of quasar discoveries from radio observations in the 1950s. Since then, AGN have been widely studied due to their complex nature which contain new insights into fields such as relativistic particles, magnetic fields, hydrodynamics and gravity.

AGN are studied in the entire range of the electromagnetic spectrum, from radio to gamma rays. Over the years, more interesting and remarkable discoveries pertaining to AGN phenomena have been observed, which leave more questions to be answered. For example, the fraction of Kerr (rotating) black holes relative to Swarzschild (non-rotating) black holes as the central engine of AGN and its effect on the broad lines observed in AGN spectra is not well constrained (Fabian et al., 2000). The standard model of an accretion disk is described by axisymmetric accretion, but some AGN do not show signs of an accretion disk, requiring other explanations for accretion (Narayan & Yi, 1995; Nemmen et al., 2009). It is difficult to directly resolve the accretion disk due to both distance and obscuration.

While we know that radio jets from AGN are driven by magnetic fields, the structure of the field is not well constrained. In a recent work, Laha et al. (2022) showed the inversion of magnetic field lines in 1ES 1927+654. This was followed by large variations in the accretion rate, with a timescale of few months.

J1007+2115 (Yang et al., 2020), a quasar powered by a 1.5×10^9 $\mathsf{M}_\odot$ black hole at $z \sim 7.5$, is an example of super-Eddington accretion. Such a massive black hole cannot exist just 700 million years after the Big Bang according to current models of black holes and theories on their growth in the early universe. The first black holes are expected to have formed around 400 Myr after the Big Bang, which is around the time of Epoch of Reionisation. J1007+2115 may provide a better estimate on the age of the universe during the Epoch of Reionisation.

These discoveries of rare and unique AGN phenomena emphasises our lack of understanding on the origin, evolution and mechanism of AGN. This thesis aims to gain insight into the evolution of AGN by searching for an interesting subset of AGN: Changing Look AGN. This chapter provides a summary of known AGN properties. Sections 1.1 and 1.2 explain the structure and classification of AGN. Section 1.3 introduces Changing Look AGN, the object of interest for this thesis. Section 1.4 outlines the project and thesis structure.

1.1   Structure of an AGN

Present literature agrees that AGN are powered by material falling into a super massive black hole, forming an accretion disk which releases tremendous amounts of energy due to releasing gravitational potential energy. The AGN also consists of a broad line region, narrow line region, a dusty torus and potentially powerful jets. This section describes each of these to present the general structure of an AGN.

1.1.1   Accretion Disk

Material tends to spiral towards the event horizon rather than fall directly into the black hole, due to its angular momentum and infall trajectory, forming an accretion disk. Simple orbital physics predicts that rotational velocities increase towards the event horizon. The dissipation of kinetic energy due to the extremely high viscosity of the disks results in emission of enormous amounts of electromagnetic radiation from the accretion disk. This accretion luminosity is roughly capped by the Eddington luminosity limit, which balances out the inward gravitational energy of material falling in against the radiation pressure of the accretion disk. Cases of super-

Eddington accretion have been found, where black holes are more massive and younger than expected by Eddington accretion (Abramowicz et al., 1988; Begelman, 2002). These cases force us to look for other explanations that allow for large black holes in the early universe such as primordial black holes or larger black hole seeds. Studies on accretion disk models have shown that the accretion disk is optically thick, but physically thin (Shakura & Sunyaev, 1973; Laor & Netzer, 1989; Hubeny et al., 2001). However, these models work only up to an Eddington ratio of ~ 0.3. Other models, such as a slim disk model proposed by Abramowicz et al. (1988), are required to explain the stability of the disks at higher Eddington ratios.

The accretion disk mostly emits in the UV and optical bands. Observing the disk directly is dependent on orientation, as the torus can block the line of sight to the central black hole. This orientation-dependence is one of many criteria that classify AGN. It is the accretion disk which is the source of luminosity for the AGN (Padovani, 2017).

1.1.2   Broad Line Region

The spectra of accretion disks in AGN with the right orientation may contain broad emission lines with widths of few thousand kilometers per second in the UV/optical bands. These broad emission lines originate from the broad line region (BLR), a key characteristic of AGN. The orientation dependency of BLR observations suggest proximity of the BLR to the accretion disk. The current AGN structure locates the BLR between the central black hole and the dusty torus (Padovani et al., 2017).

BLR studies make use of reverberation mapping. Light from the accretion disk is scattered by the dusty torus and the distance between the disk and torus produces an offset when observing light from the two regions. The scattered (reverberated) light contains additional information of the medium it travels through, which in this case passes through the BLR. Reverberation mapping has shown that the BLR is stratified, which is based on differences in the reverberation of different emission lines (Peterson et al., 2004). The BLR is photo-ionised by the accretion disk, but a recent study, Guo et al. (2020), uses reverberation mapping to show that broad MgII lines may be from collisional excitation. However, the results from reverberation mapping are ambiguous. Different models can recreate the results from reverberation studies, which allow for the structure of the BLR to be either spherical clouds disjointed from the accretion disk, or clouds adjacent to the surface of the disk. This ambiguity also extends to the kinematics of the BLR gas (Baldwin, 1997).

Reverberation mapping studies constrain the radius of the BLR to a region where the radiation

from the accretion does not evaporate dust. This temperature is approximately 1200 K. The BLR is predicted to form when the local temperature in the accretion disk is below the 1200 K limit which allows the formation of dust. However, the formed dust evaporates due to the radiation from the central engine, if it is accelerated to regions beyond the local temperature pocket due to mass outflows. Some of the material then falls back onto the disk, which results in a chaotic cycle of outflow and inflow of material through the disk (Czerny & Hryniewicz, 2011; Temple et al., 2021). This "boiling" or "failed wind" model along with the rapid rotation of the disk could allow for the observed broad emission line spectra.

1.1.3   Narrow Line Region

The Narrow Line Region (NLR) is the region around an AGN that envelopes it and extends to more than 100 pc away from the central black hole. It is much further out than the BLR, with narrow lines between 300 to 1000 kilometers per second emitted by slow moving gas clouds (Padovani, 2017). Like all other parts of an AGN, it is illuminated by the accretion of the central black hole. However, its position is favourable for direct observation. High spatial resolution spectroscopy traces the narrow line emission to a cone shaped region approximately perpendicular to the plane of the accretion disk/dust torus. This suggests that the NLR is gas present in the host galaxy that has been photoionised by radiation from the accretion disk. The gas density of the NLR is low enough ($n_e < 10^7$ cm^{-3}) to allow forbidden line transitions, such as the OIII and NII lines. We do not see broad forbidden lines due to the density ($n_e > 10^7$ or 10^8 cm^{-3}) of the BLR (Davidson & Netzer, 1979). Therefore, the forbidden lines are usually used as identifiers of AGN if the obvious broad lines are not visible (Groves, 2007).

1.1.4   Torus

The central engine is surrounded by a dusty torus. It sits in the plane of the accretion disk, at a distance away from the central black hole cool enough to allow dust formation. The UV radiation from the black hole accretion heats the dust, which emits in near-infrared thermal band. Initial estimates of the size of the outer radius varied between 5-10 pc but were later believed to be within another structure that is more than 100 pc in radius. IR observations with better instruments once again showed that the torus is a compact object within the 15 pc range which happens to be the current consensus (Elitzur, 2006). Suganuma et al. (2006) present a reverberation mapping method to learn about the inner radii of the dusty torus in AGN. They show that the lag time between infrared and UV/optical radiation, which is the

light travel time from the core to the inner radius of the torus, is strongly correlated with the optical luminosity. However, there was no such correlation between lag time and the mass of the central engine. This implies that the inner radius of the dusty torus depends on the luminosity of the accretion disk set by infall rate, rather than the mass of the black hole.

1.1.5   Jets

AGN can shoot accreting material perpendicular to the plane of the accretion disk via jets. The rotational energy of a black hole provides the energy to accelerate magnetised particles in the accretion disk. The rotation of black holes rotates the space-time around it, which in turn rotates the magnetic fields into helices. This allows for acceleration of particles from magnetised accretion disks (Blandford & Znajek, 1977). The jets are focused streams of ionised particles moving along the axis of rotation. These jets emit mostly in the radio due to synchrotron radiation, but can occasionally emit in the optical (Uchiyama et al., 2006) or high energy X-ray or γ-ray wavelengths (Tavani et al., 2009), which are considered to be sources for high energy cosmic rays and neutrinos. These jets undergo relativistic effects when the ejected particles approach the speed of light. The jets may also cause enough disturbance to modify the growth of their host galaxies (Blandford et al., 2019).

1.2   Types of AGN

The numerous differences in observed AGN at different luminosities and orientations have led to a 'zoo' of AGN within the literature. These AGN are mostly classified based on their observed spectra. But these spectra do not provide information on the entirety of the observed AGN due to obscuration of different parts. For example, AGN can be generalised as either radio loud AGN or radio quiet AGN, depending on the presence of jets or lobes in the radio band. A rather arbitrary grouping mostly attributed to radio quiet AGN is based on host galaxy visibility. Active nuclei that outshine the host galaxies are called quasars, or Quasi-Stellar Objects (QSO) due to their star-like appearance in optical observations in the mid 20th Century. Active nuclei with visible host galaxies are called Seyfert galaxies, which make up $\sim 10\%$ of all galaxies (Maiolino & Rieke, 1995).

Seyfert galaxies are further differentiated into types based on broad emission lines. From a recent review (Netzer, 2015), these types can be agreed as follows:

- **Type-1:** These Seyfert galaxies show all features of the AGN, including broad emission lines from the BLR and forbidden narrow emission lines. Some narrow lines, which have a broad line underneath or close to them, such as the NII lines, get so heavily blended that they are not easily seen at high luminosity, but are visible at low to intermediate luminosity.

- **Type-2:** These sources are distinguished from their type-1 counterparts by their lack of broad emission lines in their spectra. The width shows that the narrow emission lines are created due to powerful outflows driven by the radiation from the AGN and not due to simple dynamically stable gas clouds. Type-2 AGN are differentiated from starburst galaxies by their relatively higher BPT line ratios (OIII/Hβ and NII/Hα, Baldwin et al. (1981)).

However, this is not a hard classification, as there is a variety in the intensity of the broad emission lines relative to the narrow emission components. An intermediate sub-type classification (type- 1.2, 1.5, 1.8 and 1.9) specific to broad Balmer lines is used to characterise this variety (Osterbrock, 1981). The line ratio Hβ/OIII decreases as the type changes from type-1 to type-2, resulting in weak or undetectable higher order Balmer lines in type-1.8 and 1.9 galaxies. This typing of Seyfert galaxies may also apply to quasars, but quasars are dominated by type-1 AGN.

In addition to these subgroups, there are other groups of AGN such as the Low-ionization nuclear emission-line region (LINER) galaxies and Lineless AGN. While it is still not known if the LINER spectra are formed from AGN or starbursts, Lineless AGN are classified by their lack of detectable emission lines and a detectable non-stellar central engine. In some cases, Lineless AGN also show continuum variability, and are classified as BL Lacertae objects (Netzer, 2015).

Early works, such as Antonucci (1993) and Urry & Padovani (1995), attempted to show that all these sub groups are the same objects and can be classified in an unification scheme based on inclination and source luminosity. The unification scheme is a simple characterisation which shows that type-2 AGN are type-1 AGN with broad emission lines obscured by the dusty torus, due to their orientation to our line of sight (see Figure 1.1). However, there are cases where the BLR is just not present in type-2 AGN. NGC 3147 is currently one of the best examples where X-ray spectrum show lack of absorption in the dusty torus, and simultaneous optical spectrum show no broad lines (Bianchi et al., 2008). This implies that there are differences other than simple orientation that are truly present in type-1 and type-2 AGN.

Tran (2001) show the spectropolarimetric survey results on a sample of type-2 Seyfert galaxies.
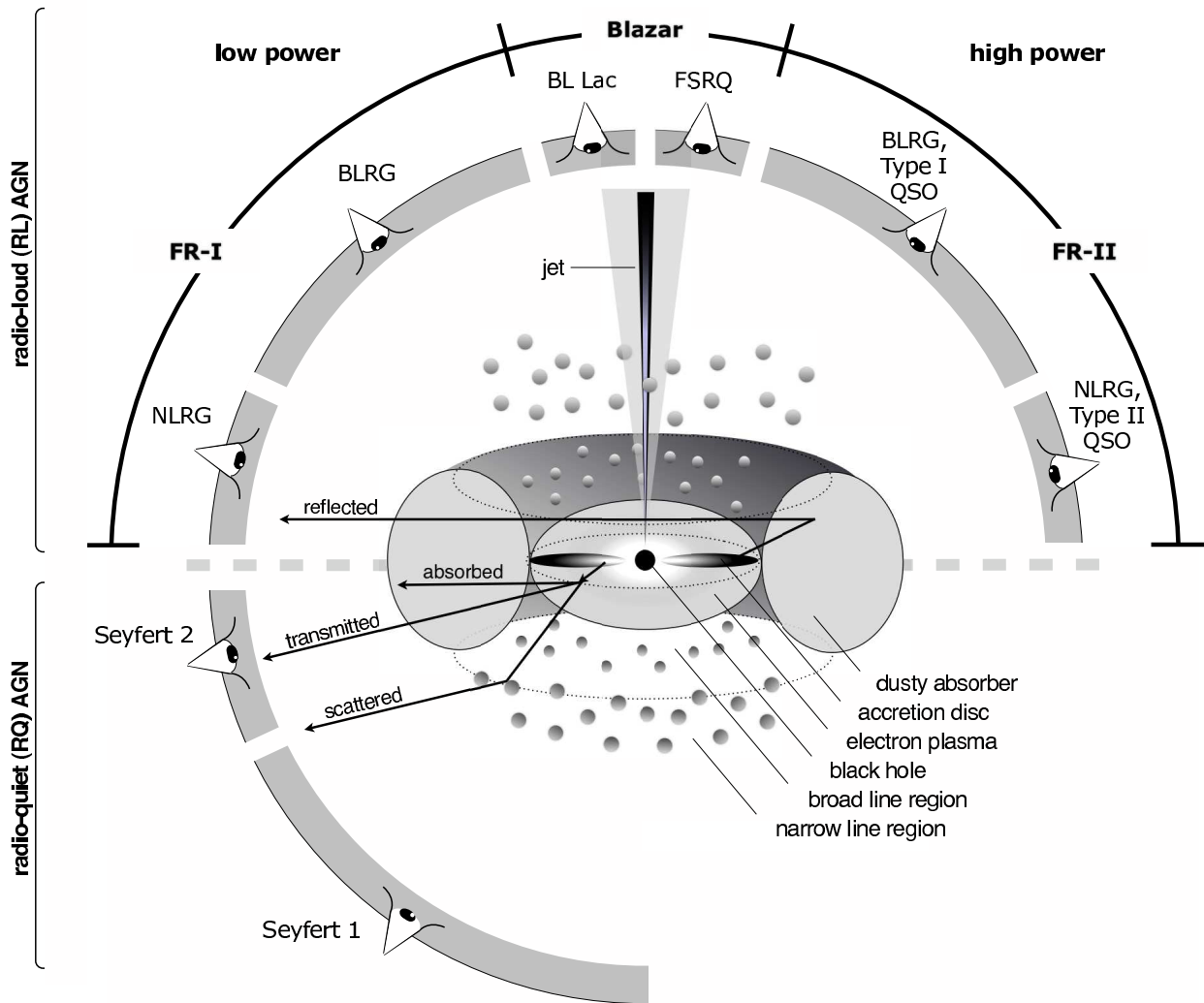
Figure 1.1: Schematic representing different AGN classification based on viewing angle. The image summarises the AGN unification model. Note that radio jets are symmetric across the plane of the torus, but are cut-off to show differences in the image. Source: Beckmann & Shrader (2012)

Cases where the BLR was hidden were found via polarisation of light. All the type-2 galaxies in the sample had similar levels of obscuration. Galaxies where the hidden BLR were detected had higher radio intensity relative to their FIR intensity compared to galaxies where a BLR was not detected. In a follow-up work (Tran, 2003), further evidence of the differences between type-2 AGN with and without a hidden BLR was presented. The central engine of type-2 AGN without hidden BLR were inherently weaker than their type-2 hidden BLR counterparts. This discrepancy is not due to the level of obscuration or dominance due to starburst. Both these works imply that while some type-2 galaxies may be hidden type-1 galaxies due to orientation, as suggested by the unification scheme, there are "true" type-2 galaxies which have a weaker central engine and a true lack of BLR. Tran (2003) also speculated that there may be evolution between type-1 and type-2 galaxies. Another explanation for the observed BLR in polarised light may be that the broad emission lines are echoes of past type-1 activity, and the BLR itself may not exist when the AGN is observed as type-2 (Hutsemékers et al., 2019).

While the lack of a BLR has been shown in certain cases, there is no real evidence as to why the BLR does not exist in "true" type-2 galaxies. Laor (2003) theorises a natural explanation based on the luminosity-radius relation for the broad line region. The relation shows broader lines at lower luminosity for a fixed mass of the central black hole. The maximum velocity of broad line emission caps at around 25,000 km s^{-1} beyond which the BLR shrinks to a radius where it is not possible for the BLR to survive, due to the large tidal forces close to the black hole. This corresponds to a minimum luminosity:

$$L_{\min} \sim 10^{41.8} \left(\frac{M_{\mathrm{BH}}}{10^8 M_\odot} \right)^2 \mathrm{ergs\ s}^{-1}$$

AGN with luminosity lower than $L_{\min}$ simply can not have an accretion disk that extends far enough for the BLR to survive. Also, in some of the weaker AGN, the accretion is too low to form a disk. In such cases, not much of the energy is radiated away as luminosity, and without the accretion disk, a BLR may not form.

1.3   Changing Look Active Galactic Nuclei (CLAGN)

In addition to the complex diversity of AGN subgroups, there are recent cases where individual AGN vary significantly more than the bulk of the population. Tohline & Osterbrock (1976) noticed the disappearance and re-emergence of the broad Hβ emission line in the type-1 galaxy NGC 7603, which happened over timescales of a year. They speculated the cause to be passing dust clouds, or change in density and optical depths of this individual AGN. However, more cases of extremely variable AGN spectra were detected in the following decades, and the idea that dis-/appearing broad emission lines may be chance encounters of obscuration has diminished.

An example of a more recent extremely variable AGN is NGC 2617, where the optical-UV continuum flux increased by about an order of magnitude and the spectrum changed from type-1.8 in 2003 to type-1 in 2014 (Shappee et al., 2014). A stronger example is Mrk 590, a classic type-1 AGN. The continuum luminosity had decreased by about a factor of 100 in less than 40 years (Denney et al., 2014). Both these works labelled these AGN as "Changing Look". These changing look events are currently mysterious phenomena as the accretion variability timescale is much shorter than expected timescales, such as the accretion disk viscous time (Lawrence, 2018). The first Changing Look Quasar (CLQ) was observed within the past decade by LaMassa et al. (2015). The CLQ, SDSS J015957.64+003310.5, is a $z = 0.31$ quasar that changed from type-1 to type-1.9 between 2000 and 2010. This quasar discovery is significant as the type

changing also affects the continuum. The host galaxy is visible as the quasar dims during its type-1.9 phase, and the quasar dominates again during its type-1 phase, allowing a clear look into both the quasar and host galaxy.

There have been tens of such CLAGN detected so far, mostly within the last decade. The cause of this variability is not known, nor are there proper constrains on the timescale of this variability. The timescales in the previous three examples range from a year to tens of years. The sample size is also not enough to statistically determine the expected fraction of CLAGN among AGN in general, or if there are other factors that determine the timescale, and whether all AGN are CLAGN when observed at short timescales. However, MacLeod et al. (2019) showed that statistically, CLAGN are more likely to be detected at low luminosity AGN with lower mass central black holes. This can be interpreted as smaller AGN having the proper physical size to allow for such short term variability, although there is no explanation for the CLAGN mechanism.

The increase in CLAGN discoveries in the early 2010s calls for systematic searches. MacLeod et al. (2016, 2019) searched for changing look QSO using SDSS photometric and spectroscopic data from different epochs. In their 2016 work, they found 10 CLQs from a sample of 1011 CLQ candidates. In their 2019 work, they found 17 new CLQs and release a candidate list of 200 objects. Even more recently, the same group (Green et al., 2022) has found 15 new CLQs by comparing past and present SDSS spectroscopic data. Yang et al. (2018) also used repeated SDSS spectra to find 21 new CLAGN with changing look timescales between 0.9 and 13 years. Graham et al. (2020) used optical and mid-IR-photometric variability to confirm 111 CLQs, but label them as "changing state quasars" to differentiate their sample which has higher luminosity and variability than previously known CLQs.

Wolf et al. (2018) used the SkyMapper Southern Sky Survey (SMSS) to report three CLAGN by scanning for brightness decline of type-1 galaxies identified by the Hamburg-ESO Survey (Wisotzki et al., 2000). In following works, Wolf et al. (2020) and Hon et al. (2022) searched for changing look Seyfert galaxies in the southern sky using previous Six-degree Field Galaxy Survey (6dFGS) spectra from the 2000s, and found 29 new CLAGN. For recent behaviour, they used SMSS photometric colours to check for discrepancies from the AGN type determined by 6dFGS spectra. Spectroscopic follow up of selected candidates revealed dis-/appearance of broad lines, if any, to identify true CLAGN. Since Seyfert galaxies are usually closer and have lower luminosity than quasars, we see a larger fraction of possible CLAGN candidates in Seyfert galaxies. Past systematic CLAGN searches have resulted in a sample of around 100-1000 candidates, but only tens of CLAGN have been confirmed in each study. Currently the

total CLAGN sample in the literature is ~ 200. Future surveys, such as the Legacy Survey for Space and Time (LSST), can further extend CLAGN sample size due to repeated observations over long time periods. A larger CLAGN sample size is essential to better understand the mechanism and evolution of AGN.

1.4   Research Goals and Thesis Outline

In this thesis, the main goals are to:

- search for new CLAGN candidates using lightcurves of Seyfert galaxies in the southern sky with $z < 0.1$ by quantifying lightcurve variability,

- follow up with spectroscopic observations on CLAGN candidates,

- compare current spectra with previous 6dFGS spectra to confirm CLAGN candidates,

- compare our CLAGN candidate list with the SkyMapper photometric study (Hon et al., 2022) which also uses a similar AGN sample from 6dFGS, and

- attempt to explain the mechanism of CLAGN phenomena using our results and other theories in the literature.

The thesis is presented as follows. In Chapter 2 we introduce NASA/ATLAS lightcurves and 6dFGS spectra, along with refining processes used on the lightcurves. Next, we present two selection methods used to identify potential CLAGN and present a CLAGN candidate list in Chapter 3. In Chapter 4, we analyse followed-up spectra of visually selected CLAGN candidates observed using ANU 2.3 WiFeS instrument to confirm true CLAGN. We discuss our results and list future directions beyond this work in Chapter 5. Finally, we summarise the thesis Chapter 6.

Chapter 2

ATLAS Lightcurves and 6dFGS Spectra

This chapter introduces NASA/ATLAS lightcurve data (Section 2.1) and the 6dF Galaxy Survey (Section 2.2). The chapter also presents our lightcurve sample (Section 2.3) and the process used to clean the lightcurve data (Section 2.4).

2.1 Asteroid Terrestrial-impact Last Alert System (AT-LAS)

In 4th Century BC, Aristotle wrote about the "unchanging heavens". We now know the night sky contains a plethora of variable objects such as asteroids, variable stars and transients. Time domain astronomy is the study of these objects by repeated observations and comparisons. This is getting easier as technology to scan the sky gets more accessible. The NASA Asteroid Terrestrial-impact Last Alert System (ATLAS)[1] (Tonry et al., 2018) is a time domain system that surveys the sky, searching for potential objects on a collision course to earth.

The system was first operational in 2015 with a single 0.5-meter telescope. A second telescope was added in 2017, and two more were added in early 2022. The first two are located at Haleakala (ATLAS-HKO) and Mauna Loa (ATLAS-MLO) observatories in Hawaii. The newer two telescopes are located at Sutherland Observatory in South Africa and El Sauce Observatory in Chile. Data from the newer two telescopes are not used in this work, and only the details of the first two telescopes will presented in the following paragraphs.

---

[1]Data available at https://fallingstar-data.com/forcedphot/

11

The geographical latitude of the Hawaiian telescopes allow observations with a declination range of $-45°$ to $+90°$. A single unit can scan the night sky in this range within a night with 900 exposures, with 30 seconds exposure time and 28.9 square degrees field of view. The pixel scale of the unit is 1.86" with mosaic dimensions of $10,560 \times 10,560$ pixels. The primary mission is to find moving asteroids, and predict their trajectories. To fulfill this mission, each unit scans a quarter of the observable sky four times a night. Before the addition of the newer two telescopes, four scans of the night sky took two days.

The two filters of interest for this work are the cyan (c) and orange (o) filters. These broad band filters cover wavelength ranges of 420-650 nm for the cyan filter and 560-820 nm for the orange filter. The orange filter is fitted in both units as it produces sharper images. The ATLAS-HKO unit switches to the cyan filter during the half of the lunar cycle surrounding the new moon. With 30 seconds exposure, sources as faint as $m \sim 20$ can be detected using the orange filter on dark nights with good seeing.

2.2   6dF Galaxy Survey (6dFGS)

The Six-degree Field Galaxy Survey[2] was a redshift survey conducted between 2001 and 2009 (Jones et al., 2004, 2009). The survey used the 1.2m UK Schmidt Telescope at the Siding Spring Observatory. It was one of the largest redshift surveys at the time, with 110,256 new redshifts of extragalactic sources determined, along with a catalogue of 125,071 galaxies. The survey almost covered the entire southern sky, and went up to $z \sim 0.15$.

6dFGS captures its spectrograph using the Six-degree Field (6dF) multi-object fibre spectroscopy facility. The system can capture up to 150 spectra using 150 science fibres and an additional four guide fibres. Spectra are obtained by positioning the fibres on pre-configured targets on a field plate, and directing the light to a fibre slit block in the spectrograph. The light-collecting end of the fibres holds a prism that splits and deflects light into the fibres. A drawback to this is that targets cannot be closer than 5.7', as the apertures need to be physically separated to prevent interference.

Wei Jeat (Jack) Hon, a PhD student from University of Melbourne in our AGN collaboration, has worked on a subset of 6dFGS spectra to measure emission lines, and classified galaxies into AGN of types 1, 1.2, 1.5, 1.8, 1.9, 2, and SF (star-forming galaxies). The broad lines are measured by fitting the Balmer lines, Hα and Hβ, to obtain the full width at half maximum (FWHM). This new catalogue (yet to be published) of AGN types will be referred to as the

---

[2]Data available at http://www-wfau.roe.ac.uk/6dFGS/

6dFAGN catalogue for the remainder of this work. The type classification in the 6dFAGN catalogue is used as a reference for the type of the observed AGN at the time of the 6dFGS operation.

2.2.1   6dFGS Fibre Cross-talk

We noticed cases where the 6dFGS spectra of broad line objects had been assigned incorrect redshifts, or had broad Hβ lines but no Hα emission. This is due to astigmatism near the edges of the 6dFGS spectrograph. Bright features, such as broad line emission of AGN, can leak through and contaminate adjacent spectra through fibre cross-talk (e-mail correspondence with 6dFGS PI Heath Jones). Some broad line AGN in the 6dFAGN catalogue are therefore not true AGN as they show blended spectra of different sources within the field of view. These objects need to be removed from the sample.

To remove these contaminated objects, we search through all type 1-1.9 spectra and select candidate cross-talk pairs/groups with the following criteria: (1) position in the sky within six degrees to account for the six degree field of view on the spectrograph, (2) assigned redshift within c$z < 500$ km s^{-1} as contaminated spectra would be assigned redshift similar to the true AGN, and (3) adjacent spectrum ID, as cross-talk affects adjacent fibres in the spectrograph. Although cross-talk can contaminate any source, we limit our search to broad line AGN as the contaminants would only have broad lines appearing in them, but existing broad lines do not vanish. None of the type-2 AGN in the 6dFAGN catalogue would be marked as type 1-1.9 even if they are contaminated, as they do not have broad lines. We find 9 groups of possible candidates, of which 7 were visually confirmed to have cross-talk (see Table 2.1), producing fake broad lines.

True AGN spec-ID	True AGN name	Contaminant spec-ID	Contaminant name
7520	g0105388-141614	7519	g0101488-163843
15574	g0230055-085953	15573	g0239545-082404
24755	g0414527-075540	24756	g0414221-082044
55640	g1139017-374419	55641	g1138589-380042
127974	g1145405-182715	127975	g1148026-184952
59993	g1231372-475802	59994	g1238285-490138
82765	g1638309-205525	82764	g1636268-211835

Table 2.1: 6dFGS spectra with visually confirmed cross-talk contamination. The spec-ID columns refer to the column of the same name in the 6dFGS catalogue.

2.3 Lightcurve Selection

Over the past six years, ATLAS has scanned the sky and recorded lightcurves of millions of sources in the night sky. These objects include asteroids, stars, transients and extragalactic sources including Seyfert galaxies. The ATLAS observations cover the north sky and go down to a declination of $-45°$ while 6dFGS only contains galaxies in the southern hemisphere. We therefore select galaxies with declination of $-45° < \delta < 0°$. Our lightcurve sample has 84,376 galaxies from the 6dFGS catalogue and 24,426 additional galaxies from external catalogues, totalling 108,802 lightcurves. We also limit redshift to $z < 0.1$ to maintain lightcurve quality at a consistent level as apparent magnitude increases with distance. At $z \sim 0.1$, the OIII emission line approaches the 5577Å sky emission line, which is difficult to subtract and can hinder AGN spectra comparison. For our CLAGN search algorithm, we thus limit the lightcurve sample to 2,698 AGN and 13,534 SF sources obtained from the 6dFAGN catalogue.

2.4 Cleaning Lightcurves

2.4.1 Error cut-off

The ATLAS lightcurves are obtained using difference image photometry. Each subsequent observation is subtracted from an initial reference image, called the wallpaper. The lightcurve is expected to be constant at zero for static sources, positive for brightened sources, and negative for dimmed sources. Both the wallpaper and subsequent observations contain errors, which are carried forward in the subtraction. The data provides the difference flux and subtraction error in microJanskys (μJy).

From our initial look at the lightcurves, it was evident that some difference flux measurements with large errors were not meaningful. These measurements needed to be removed from the lightcurves. In order to determine a cut-off for large errors, we compiled a list of errors from a 10% subset of our sample. We then cut-off errors via iterative sigma-clipping of errors beyond three standard deviations from the mean error, until the new mean changed by less than 1 μJy from the previous iteration. The errors from the raw lightcurves went up to 10^9 μJy with a small fraction of errors larger than 10^3 μJy. After sigma-clipping, the error was capped at 45 μJy after rounding up (see Figure 2.1) and $\sim 15\%$ of the measurements were clipped. We use the 45 μJy error cut-off to filter bad measurements from the entire data set. As the measurements with low errors are reliable, our sigma-clipping process is limited to the positive direction.
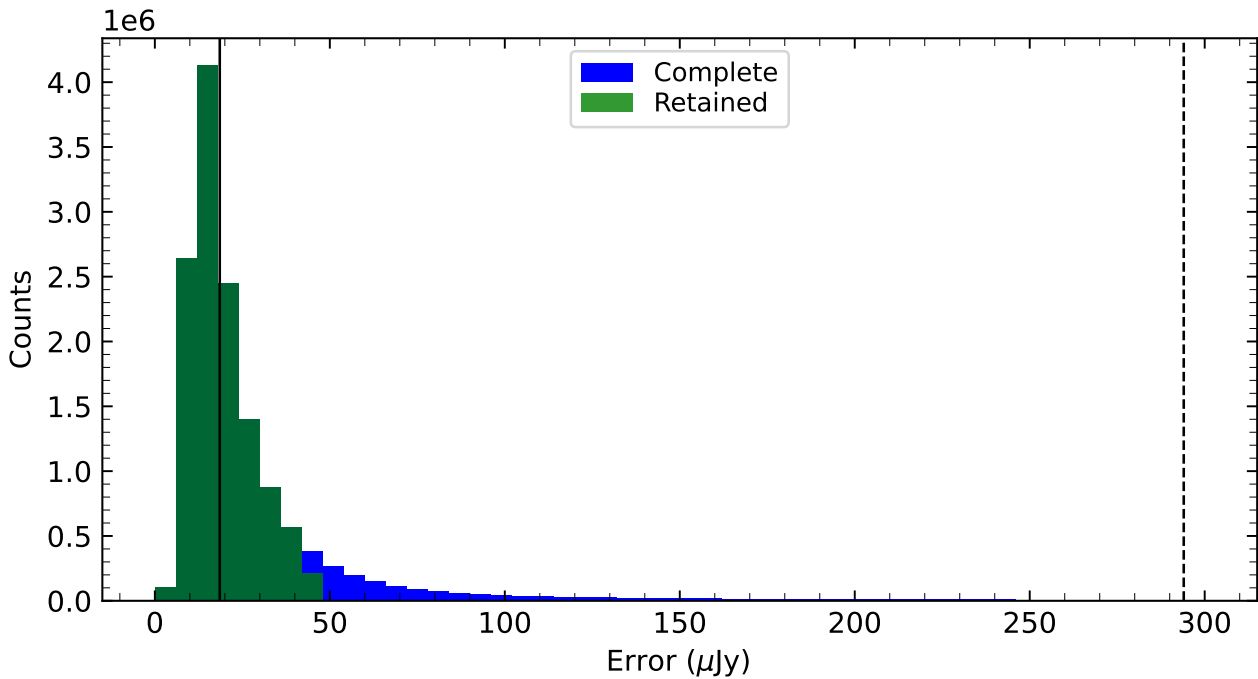
Figure 2.1: A histogram of errors from each difference flux measurement from a 10% lightcurve sample. The dashed vertical line represents the initial mean and the solid vertical line represents the mean after clipping. The range of the plot is limited to 300 μJy but the complete errors (blue) continue onward to $> 10^9$ μJy. The retained points (green) have the errors capped at 45 μJy.

2.4.2 Stacking

ATLAS lightcurves contain multiple measurements per night, and these measurements are inherently noisy. To reduce noise, we stacked and averaged measurements over a fixed period. The period was set rather arbitrarily, long enough to reduce noise, but not too long that true variations are lost. We chose a seven-day period for the orange filter measurements. The cyan filter measurements were relatively scarce, and only carried out in dark time of the lunar cycle. Hence, we stacked the measurements based on the lunar cycle. As a result, the orange stacks contained a maximum of 12 measurements (7 nights, 4 measurements every two nights), while the cyan stacks could reach up to ~ 30 measurements per stack, depending on the weather.

Each stack is represented by the median value of measurements in the stack, as the mean is sensitive to outliers in a small sample. Since our aim is to characterise the variability of the lightcurves, we can retain some information of the variability of the measurements within the stacked period, by setting the inter-quartile range (IQR) as the error over the stacked period. Hence, each stack is presented as a box-plot of difference flux measurements. This would mean that stacks with fewer than 3 points needed to be ignored, but the stacking period was long enough that such cases were minimal.

In rare cases, coincident measurements may lead to an IQR that is smaller than the expected

measurement error of the stack, and would then incorrectly represent the validity of the stacked measurement. To prevent this, we compute the error of the stack points from the following:

$$\text{stacked error} = \max\left(\frac{\text{IQR}}{2}, \text{ mean measurement error}\right) \tag{2.1}$$

The mean measurement error does not include a $1/\sqrt{N}$ term, because once again, we require our stacked errors to be comparable to the variability of the measurements within the stacked period, similar to the IQR. The stacked points were further refined by following a similar recipe of sigma-clipping large errors. The stacked error cut-off was once again determined from the same 10% lightcurve sample used to clip measurement errors. Figures 2.2 and 2.3 provide histograms of the clipped errors. The maximum stacked errors before clipping reaches $\sim 10^6 \, \mu\text{Jy}$ as the IQR with a sample of $N < 5$ can depend heavily on outliers. The final stacked errors after clipping are capped at 50 μJy for orange and 35 μJy for cyan.
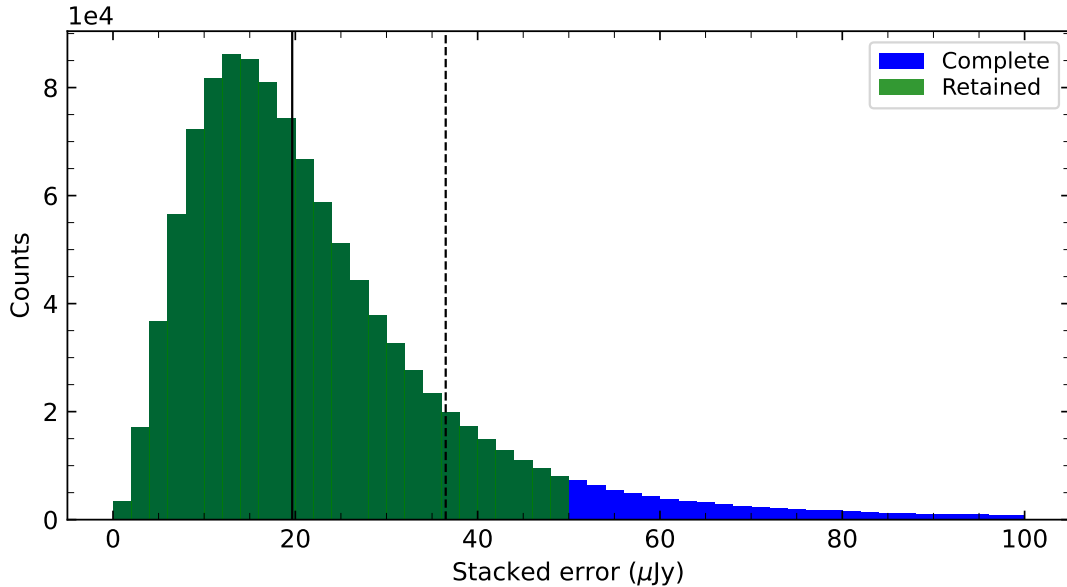
Figure 2.2: A histogram of errors for the **orange** stacked data from the 10% lightcurve sample. The dashed vertical line represents the initial mean and the solid vertical line represents the mean after clipping. The range of the plot is limited to 100 μJy but the complete errors (blue) continue onward to $> 10^6 \, \mu$Jy. The retained points (green) have error capped at 50 μJy.

2.4.3   Wallpaper and Sensible Dates

The reference image for difference photometry, called the wallpaper, was updated in two occasions. The wallpaper transitions happened around MJD 58417 (26 Oct 2018) and MJD 58882 (03 Feb 2020). The change in wallpaper can lead to step discontinuities in the lightcurve, especially for variable sources and galaxies with previous transient events. Figure 2.4 provides an example of such a discontinuity from a Tidal Disruption Event (TDE). These wallpaper
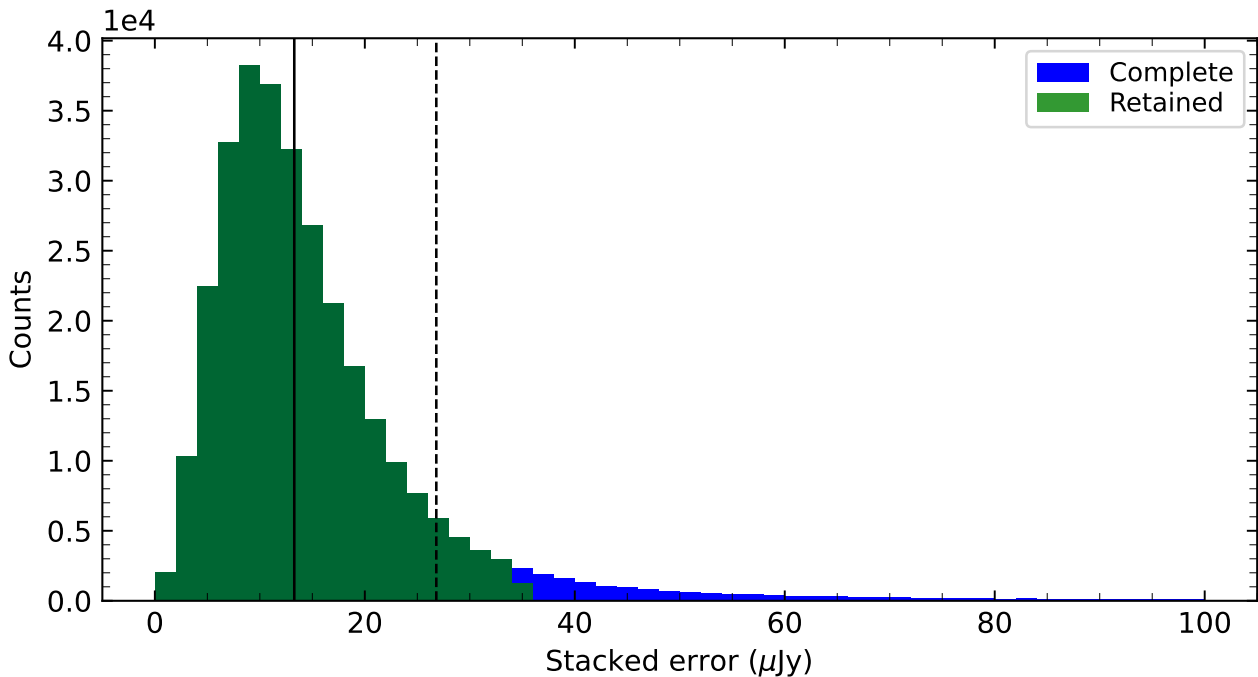
Figure 2.3: Same as Figure 2.2, but for **cyan** filter stacks. The retained points (green) have error capped at 35 μJy.

changes are not expected to affect non-variable lightcurves. However, any quantity that measures variability of a lightcurve would be affected by the step discontinuities. In this work, we only look for a threshold that classifies variable lightcurves from non-variable lightcurves, and not a measure of variability. Therefore, the wallpaper effect can be largely ignored.

Note: All following lightcurve plots in this work will include vertical grey lines marking the two wallpaper changes.

After error sigma-clipping, stacking and stacked error sigma-clipping, we compiled a single averaged lightcurve of the whole sample to check for instrumental or seasonal trends, plotted in Figure 2.5. Although we did not find any obvious seasonal trends, we discovered a lack of consistency in the measurements until March 2017 (MJD < 57900). Correspondence with ATLAS PI John Tonry revealed that these points could be due to the PSF not being centered on the target. The change after March 2017 was a replacement of Schmidt correctors, but the difference image pipeline uses the plate solution for the new corrector, even for images taken with the old corrector. For this thesis, measurements before MJD 57900 will be ignored. Another outlier is the week centered around MJD 59199 (16 Dec 2020). There is a consistent dip in brightness of all lightcurves during the week, which could be due to a long period of bad seeing or other problems. This stacked measurement is removed in the cleaned lightcurves.
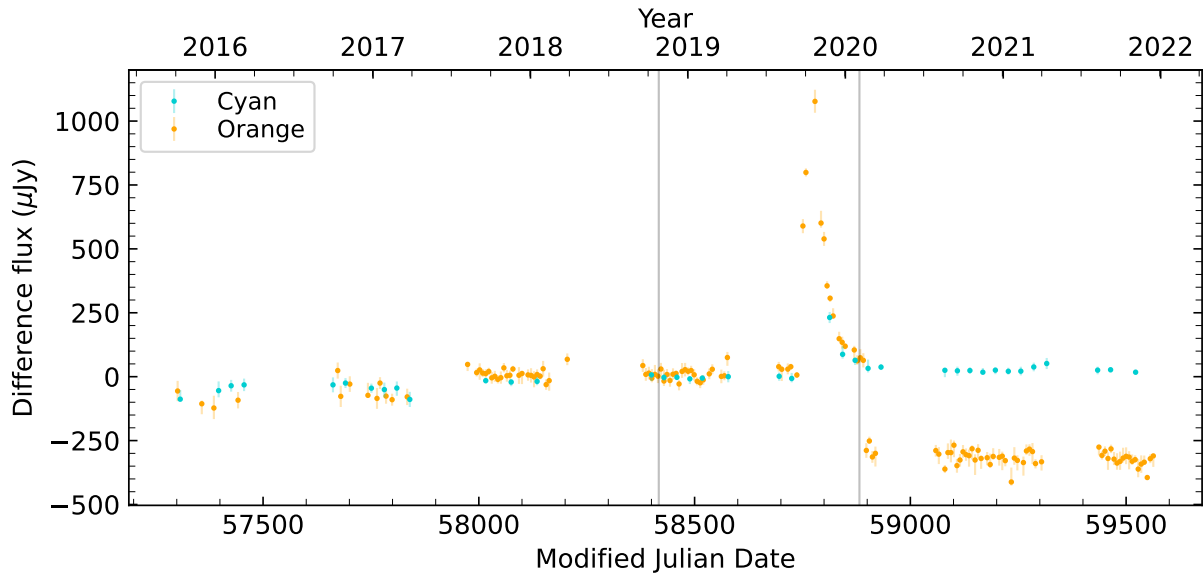
Figure 2.4: Tidal Disruption Event (TDE) *2019qiz* (Nicholl et al., 2020), 6dFGS object: g0446379-101335. The vertical grey lines represent the major wallpaper changes. The TDE occurs at the end of 2019. There is a notable step discontinuity at the second wallpaper change. Only the orange measurements are affected.
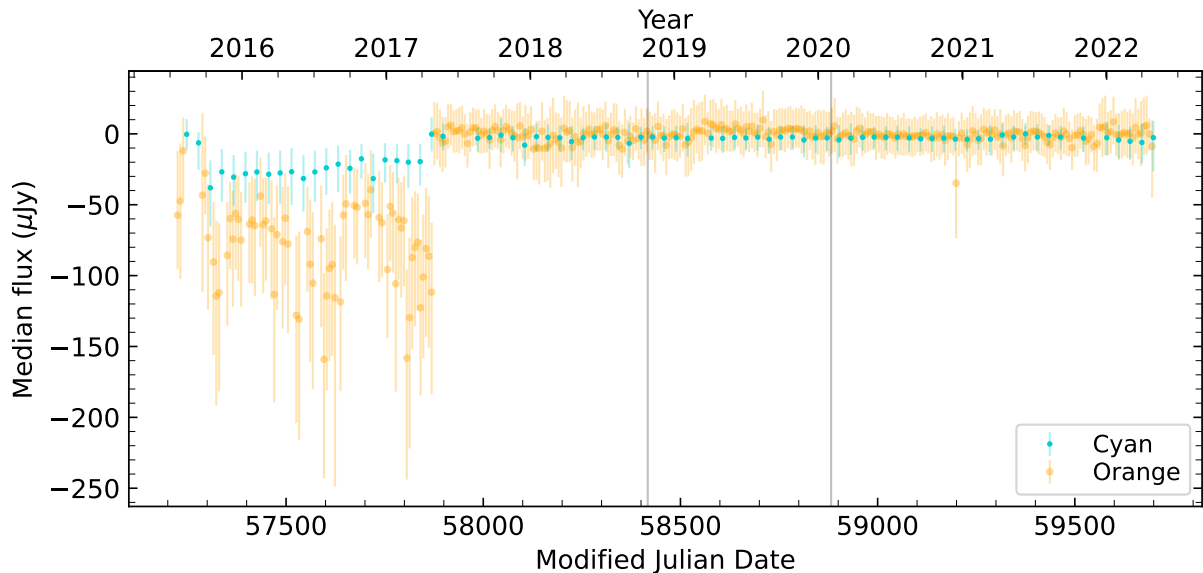
Figure 2.5: The total averaged lightcurve of the complete lightcurve set. The points are medians with IQR error of each stack. Orange measurements are stacked weekly while cyan measurements are stacked around new moon. There is a significant inconsistency in the lightcurve for measurements before March 2017. An outlier is observed in the week around MJD 59199.

Chapter 3

CLAGN Candidates

Past works on systematic CLAGN selection mostly used photometric approaches (see references in Section 1.3). An AGN is selected as a candidate if its observed flux in a particular band changes significantly within two epochs. Spectra of these candidates compared over similar epochs confirmed whether these candidates are true CLAGN. In contrast, we use a lightcurve variability approach to select our candidates. We exploit the stochastic variability of AGN emission from the accretion disk in an attempt to infer the type of an AGN.

Variability studies in literature lean towards type-1 AGN, as the variable accretion disk is obscured in type-2 AGN according to the unification model. In this work, we assume that AGN of types 1.8-2 do not show the variable accretion disk. We expect their lightcurves to be analogous to that of non-active or star forming galaxies, i.e., non-variable over the lightcurve period of ~ 5 years. This is a reasonable assumption, as we see the distribution of our type-2 variability measure overlaps with the distribution of star-forming galaxies (to be explained in Section 3.2 and illustrated in Figure 3.5). An example of the expected lightcurve behaviour for each type is presented in Figure 3.1. We identify CLAGN candidates by selecting lightcurves that do not show the expected variability behaviour for their respective 6dFAGN type. Following the convention in literature, we define turn-on CLAGN as AGN that change from a higher type to a lower type (eg. $2 \to 1$) and the inverse type transition (eg. $1 \to 2$) is defined as turn-off CLAGN.

We provide CLAGN candidate lists via two different approaches using the variability of the lightcurves. In Section 3.1, we provide details on the first method, searching for CLAGN from a known AGN sample by eyeballing lightcurves. In Section 3.2, we present the second approach: quantifying a variability threshold to mark lightcurves as either variable or non-variable. The results for the variability classification of both approaches are presented in Section 3.3.
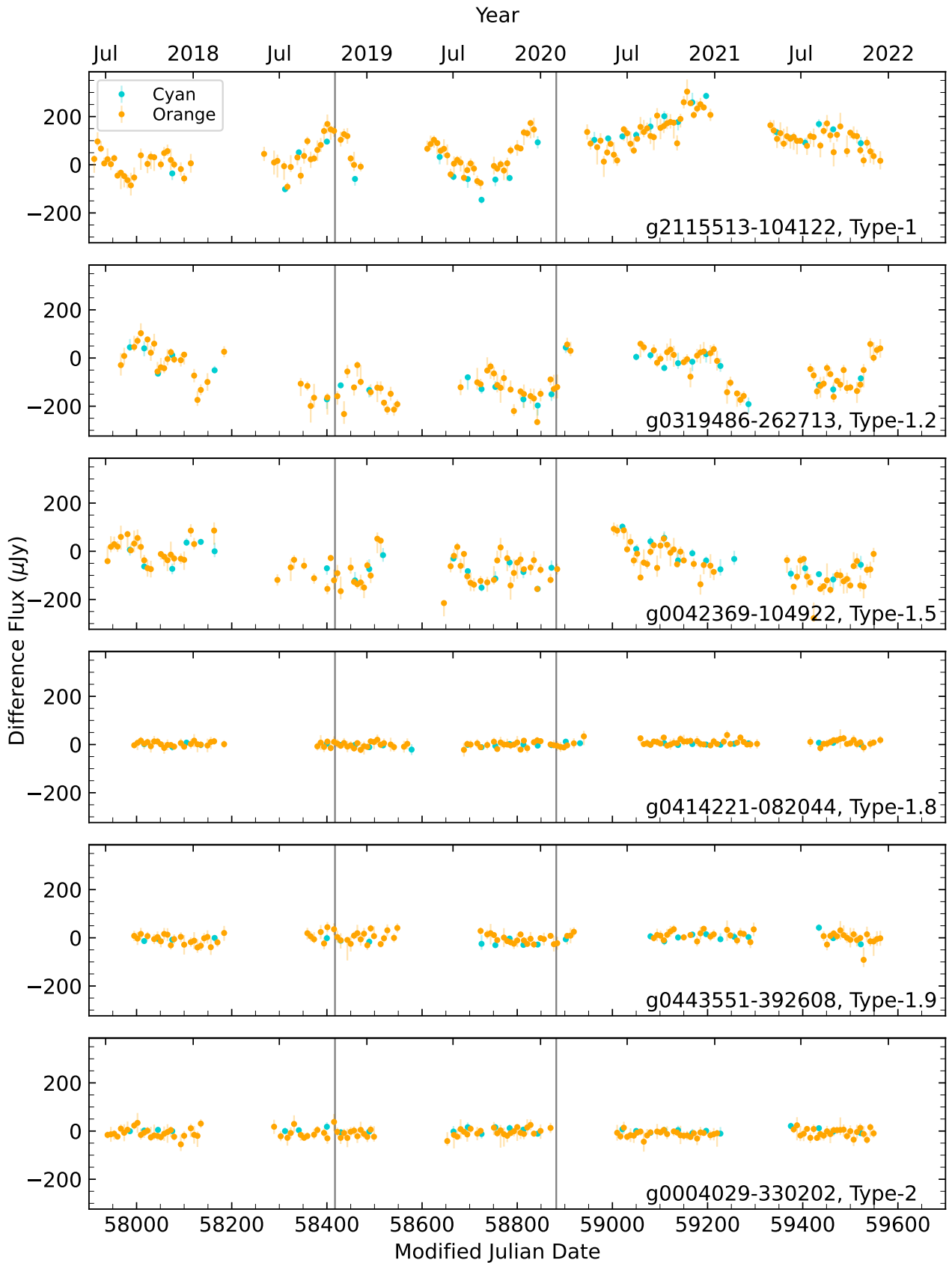
Figure 3.1: Six lightcurves of Seyfert galaxies representing expected behaviour for their respective types. The representatives are selected at random and show non-CLAGN behaviour. Types-1, 1.2 and 1.5 show flux variations, while the remaining three do not. There is no expectation for greater variability of type-1 Seyferts compared to type-1.2 and 1.5 since the flux measurements are not normalised for distance. Note the step discontinuity at the second wallpaper update (vertical grey line) for the type-1.2 example.

3.1 CLAGN Candidate Selection I: Visual classification

For this candidate selection process, we manually browse through each lightcurve and check for conspicuous flux variations. AGN that have lightcurves that deviate from their expected behaviour for their respective types are selected as CLAGN candidates. We cannot procure the AGN-host decomposition from the lightcurves as the lightcurves provide difference photometry fluxes. Therefore, we do not know the relative AGN flux change, and thus, we cannot provide a robust candidate selection criteria using the visual method. In addition, our visual classification is generous in selecting CLAGN candidates, that is, ambiguous cases of variability are also selected as candidates, which makes our candidate list more complete but less pure in selecting true CLAGN.

3.2 CLAGN Candidate Selection II: Quantitative Variability Threshold

The visual method is not reliable in providing a CLAGN candidate list from a large AGN sample. The candidate list may vary each time the visual classification is conducted due to the lack of a robust variability measure to classify ambiguous variability in lightcurves. Hence, we introduce a quantitative variability threshold that can reliably provide a CLAGN candidate list. In order to define a threshold, we must first define a variability measure.

Based on the difference in variability of the different AGN types in Figure 3.1, we can estimate a simple variability quantity such as the root-mean-squared error (RMSE) of the lightcurve. We start by median-shifting the lightcurve to the origin for both convenience and consistency, as the difference flux fluctuates around the origin in most lightcurves. We then divide each flux measurement by its error obtained from Equation 2.1, which over-weights measurements farther from the origin, but with minimal variability within the stacked measurements. We then compute the RMSE from the origin separately for both the o and c bands, providing two RMSE quantities: Q^c_{RMSE} and Q^o_{RMSE}. We define the complete RMSE quantity as:

$$Q_{\mathrm{RMSE}} = \log(Q^c_{\mathrm{RMSE}}) + \log(Q^o_{\mathrm{RMSE}}) \tag{3.1}$$

However, we notice a few lightcurves with outliers in the general lightcurve pattern, which survive the error-elimination outlined in Section 2.4. Q_{RMSE} is sensitive to these outliers in the lightcurve. Furthermore, it is difficult to account for different variability amplitudes due

to different observed magnitudes. We also notice that the o-band measurements are much better sampled and the number of c-band flux measurements is significantly inconsistent across different lightcurves. To prevent the cyan measurements from decreasing the sensitivity of the variability measures, we ignore c-band measurements altogether.

Taking these points into consideration, we introduce a new variability measure that ignores the shape of variability and can be easily corrected for apparent magnitude:

$$Q_{\mathrm{var}} = \log\left(\frac{R^o_{98-2}}{\langle X_{err}\rangle}\right) \tag{3.2}$$

where R is the percentile range denoted in its subscript, while the superscript is the filter band. $\langle X_{err}\rangle$ is the mean of the errors given by Equation 2.1. Once again, the division over-weights larger ranges with smaller mean error. We also remove lightcurves with less than 90 weeks' worth of o-band measurements, as they may not completely capture source variability. For reference, the light curve period is ~ 235 weeks and most lightcurves have ~ 120 weeks populated. The 90 week cut-off removes 5% of the total AGN and SF sample.

To account for differences in variability amplitude due to distance, we can correct for the observed magnitudes. Since the mean o-band magnitude is not available, we use r-band PSF magnitudes (r_{psf}) from the SkyMapper Southern Sky survey (SMSS DR3, Wolf et al. (2018)) to correlate observed magnitudes with Q_{var}. The SMSS r-band data is valid as there is significant overlap between o-band and r-band wavelength ranges and the observations were made within the period of the lightcurves.

With a variability quantity defined, we can introduce a threshold that classifies lightcurves as either variable or non-variable. To do so, we first require a reference of either variability or non-variability. The 6dFAGN catalogue indeed contains a sample of star forming (SF) galaxies, whose lightcurves are non-variable. Since we expect the lightcurves of type-2 AGN to be analogous to those of SF sources, we can use the distribution of Q_{var} of SF sources as a reference for non-variable AGN. Thus, we can define the threshold as the upper-limit of r_{psf}-corrected Q_{var} distribution of SF sources. However, we must first clean the non-variable SF sample from any transient events that could affect the threshold. We also include 6dFAGN type-2 sources in our event search sample to prevent incorrect selection of event contaminated type-2 lightcurves as CLAGN candidates.

3.2.1 Eliminating Events

Stochastic variability in AGN emission is not the only feature that is visible in lightcurves. Transient events, such as supernovae (SNe) and Tidal Disruption Events (TDE), result in a quick rise, followed by an exponential decay in emitted light over time. TDEs are observed in the nucleus of galaxies, as a black hole tears apart a compact object, producing temporary emission across many wavelengths. For TDEs, the luminosity decays as $t^{-5/3}$ (eg. see Figure 2.4, van Velzen et al. (2020)). On the other hand, SNe can be observed in any part of a galaxy, and since ATLAS centres the PSF onto the nucleus itself, flux measured from an SN at the edge of the galaxy can be underestimated. In both cases, the transient events can increase the variability measure Q_{var}. To prevent these events from contaminating our variability classification, we identify and remove the most distinct TDE/SNe from our sample.

In an ideal case, a lightcurve containing an event will be non-variable, apart from the event itself, which would show a distinct spike. In such cases, the number of flux measurements over the time of the event is smaller than the number of measurements over the entire period of the lightcurve. The inter-quartile range (IQR) is a rough measure for the variability amplitude of the object excluding the event. The ratio of the complete flux range of the lightcurve and the IQR is then an indicator for an event. To remove any outliers, that can exaggerate the flux range of the lightcurve, we use the 2-98th percentile range (R_{98-2}) in place of the complete range. The event indicating quantity, Q_E, is then

$$Q_E = \frac{R_{98-2}^o}{R_{75-25}^o} \tag{3.3}$$

where the subscript of R is the percentile range, and the superscript is the band. We once again ignore the c-band measurements.

While lightcurves with high Q_E values indicate spikes, the significance of the spikes separates events from non-variable or weakly variable but noisy lightcurves. To differentiate the significant spikes from a noisy lightcurve, we use the Q_{RMSE} quantity. Note that we do not use Q_{var} here as we need a general variability quantity that is more sensitive to outliers and spikes in the lightcurve, and Q_{RMSE} is the better choice.

In Figure 3.2, we plot the two quantities for SF and type-2 sources, and mark the candidate events and confirmed events. A cut-off is visually determined to separate outliers from the main cloud of points. The candidates are sources that sit above the line, and each candidate is individually checked for events. We also find that the confirmed events are blended with false candidates of the distribution closer to the cut-off. As the event candidates are confirmed

visually, lowering the cut-off would include more contaminants, and accordingly, more ambiguous cases of events. To prevent any cases of false event assignment, we look for only the most obvious signs of event flares. Our search finds 63 events from 305 candidates, which are then removed from the SF and AGN sample.

We plot Q_{var} as a function of r_{psf} of the event-eliminated SF sources in Figure 3.3. The percentile contour lines are linear and almost parallel within the most complete magnitude range, but the contour lines get noisy with increasing percentiles. A linear fit to a contour line within the most complete region provides a fixed slope, and the intercept can be adjusted to obtain a threshold, T_{SF}, which is the fraction of SF sources that are below the line. This linear fit is a binary classification threshold. Sources that lie above the threshold line are marked as variable, and sources that lie below are marked non-variable.
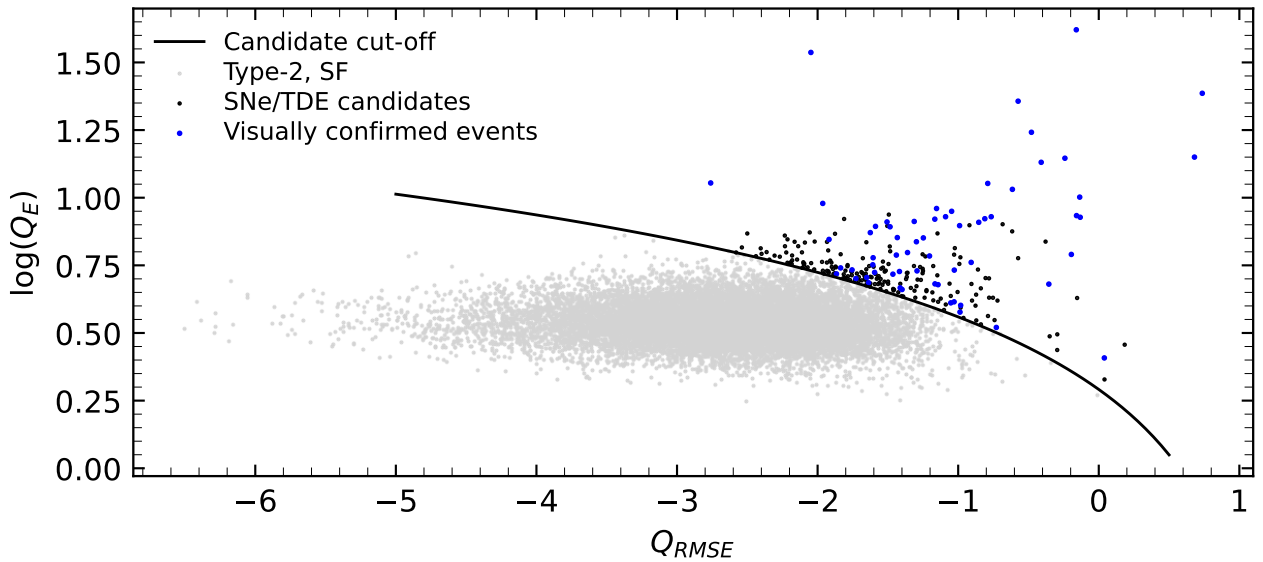
Figure 3.2: Event indicating quantity and RMSE quantity of SF and type-2 sources. The cut-off for candidate selection was visually determined from the plot. Most of the outlying sources are visually confirmed to contain events in the lightcurves. There are a few visually confirmed events near the cut-off, which indicates more lightcurves affected by events can be found within the non-candidates.

3.2.2   Optimising Cut-off Threshold

The problem now is to choose a suitable slope and T_{SF}, such that we obtain a complete and pure separation of variable sources within the AGN sample. We choose the 90th percentile contour line of the SF sources to obtain the gradient. This maximises proximity to the upper edge of the cloud of points while retaining the smoothness of the contour line, as noise increases at higher percentiles due to smaller sample size at the upper edge. The slope of our cut-off line is thus fixed at -0.134, which corresponds to the gradient of the linear fit to the 90th percentile
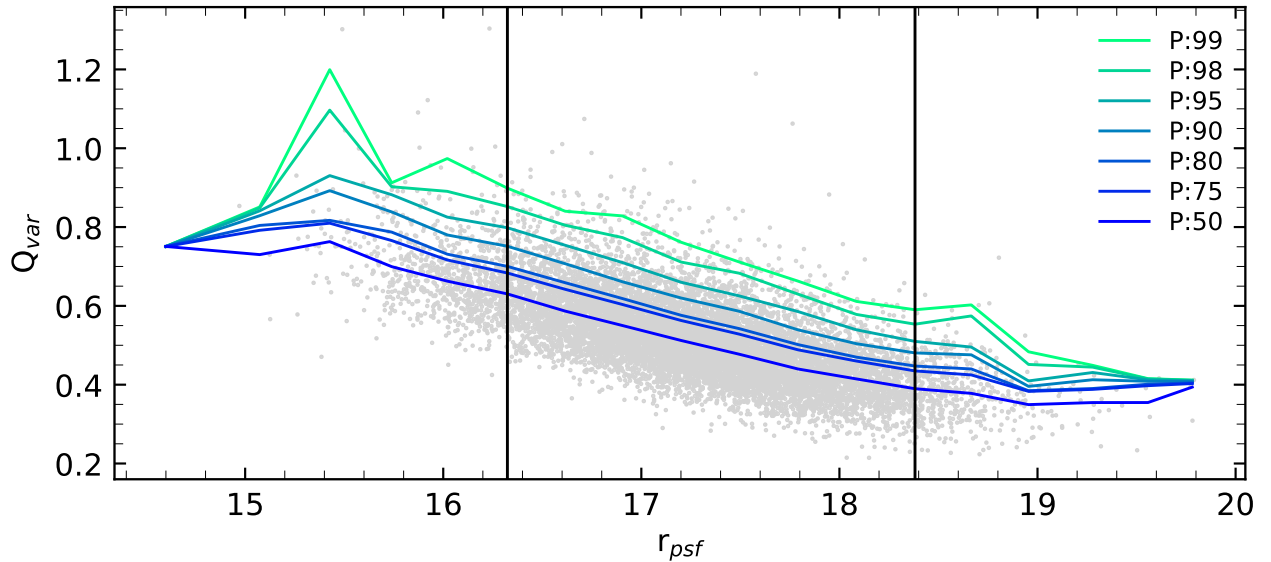
Figure 3.3: Effect of observed brightness of the source on Q_{var}. The grey points are the SF sources after eliminating transient events. The cyan-blue lines mark the percentile contours of SF sources in each r_{psf} bin with bin width of 0.3 dex. The region enclosed by the vertical black lines represent the r_{psf} range that is most complete, and we see discontinuities in the percentile lines beyond this region. We also see some noise at higher percentiles due to smaller sample size above the threshold contour lines.

contour line. We then iterate through different intercepts for the cut-off line, and compute the completeness and purity of the sources marked as variable as follows.

Variability Completeness

We define completeness as the fraction of truly variable objects that sit above the variability threshold. We start off the reference completeness list by selecting all AGN with 6dFAGN types 1-1.5 from the 6dFAGN catalogue, as these are expected to have stochastic variability in their lightcurves. We then clean this list for any known CLAGN that are spectroscopically confirmed over the period of the lightcurves. That is, we remove known turn-off CLAGN and add known turn-on CLAGN from Wolf et al. (2020), Hon et al. (2022), and from the spectroscopically confirmed CLAGN from the visual method (see Chapter 4). We also remove objects with 6dFGS spectra contaminated by cross-talk, listed in Table 2.1.

The reference list has 248 sources that are expected to show variability. We do not modify the list to account for candidates selected using the visual method, as the visual method classifies variability by eye without a robust threshold. Unknown turn-off CLAGN, if any, are still included in the reference list. Our completeness fraction is therefore marginally underestimated.

Variability Purity

We check for purity by once again assuming none of the SF sources show variability in lightcurves. The complement of T_{SF} is the fraction of SF above the threshold line which are marked incorrectly as variable. We exploit this information to compute a contamination rate for the AGN marked as variable. The total number of true non-varying AGN (of all types 1-2), $N_{\text{non-var, AGN}}$, in the AGN sample is given by

$$N_{\text{non-var, AGN}} = \frac{1}{T_{SF}} n_{\text{non-var, AGN}} \tag{3.4}$$

where $n_{\text{non-var, AGN}}$ is the number of AGN that lie below the threshold line. The fraction of $N_{\text{non-var, AGN}}$ that lie above the line is $(1 - T_{SF})$. Contamination rate of sources marked as variable, C_{AGN}, is then the fraction of true non-variable objects that lie above the threshold line:

$$C_{AGN} = (1 - T_{SF}) \frac{N_{\text{non-var, AGN}}}{n_{\text{var, AGN}}} \tag{3.5}$$

where $n_{\text{var, AGN}}$ is the number of AGN that lie above the threshold line. The purity is the complement of the contamination rate,

$$\text{Purity} = 1 - C_{AGN} \tag{3.6}$$

We plot the completeness and purity for different T_{SF} in Figure 3.4 and mark three threshold values (see Table 3.1) where the the completeness and purity are suitable. A summary of the three T_{SF} values is presented below:

- $T_{SF} = 0.90$ has far too less purity to use as a reasonable cut-off.

- $T_{SF} = 0.95$ is the balancing point between purity and contamination.

- $T_{SF} = 0.98$ has far too less completeness to use as a reasonable cut-off. However, we obtain a much purer turn-on CLAGN candidate list, that is, candidate AGN that change types from 1.8-2 to 1-1.5.

For this work, we choose the threshold line, $T_{SF} = 0.95$, which corresponds to the equation

$$Q_{\text{var}} = -0.134 \cdot r_{\text{psf}} + 2.973 \tag{3.7}$$

with a completeness of 0.87 and purity of 0.77. We lean towards higher completeness rather than purity as lower completeness would miss true CLAGN in our candidates, which would be

detrimental to our aims.
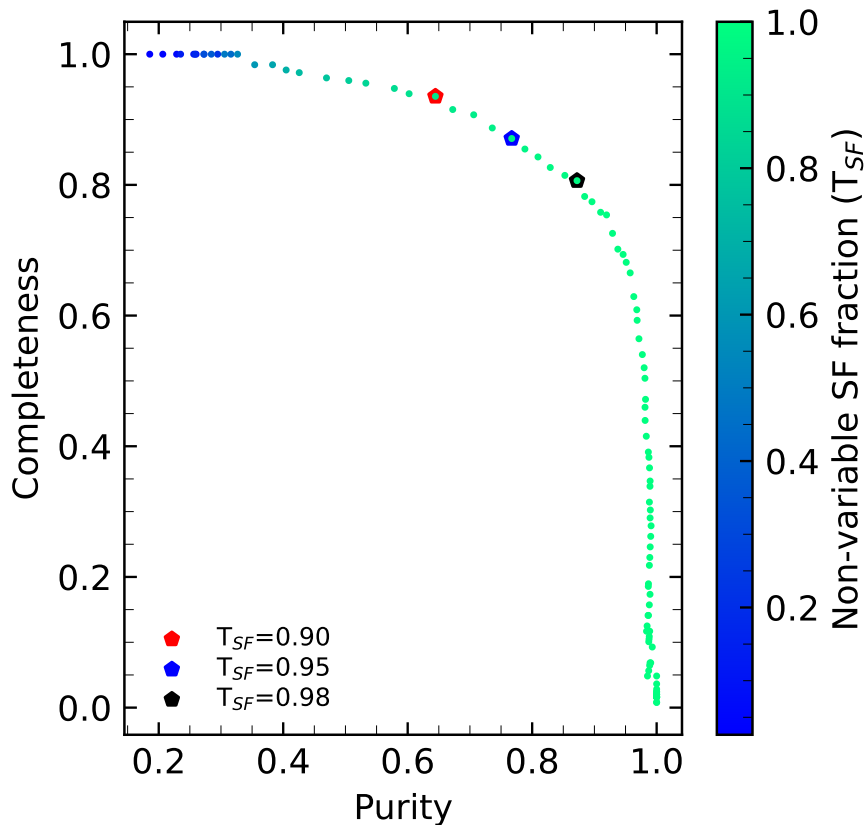
Figure 3.4: Completeness and purity for different T_{SF}. The three marked points outline a reasonable region for the both completeness and purity, which is used to choose an optimal T_{SF}.

T_{SF}	Missed Variables*	Completeness	Variable	Non-Variable	Contaminants	Purity
0.90	16	0.935	549	1787	195	0.645
0.95	32	0.871	424	1912	99	0.767
0.98	48	0.806	335	2001	43	0.872

Table 3.1: Completes and purity table for the three marked T_{SF} in Figure 3.4.
*The number of truly variable sources that are marked as non-variable, which may include unknown turn-off CLAGN. We consider 248 AGN in our sample as truly variable.

3.3 Classification Results

The number of variable candidates of each 6dFAGN type is presented in Table 3.2 for the visual and variability threshold methods where the latter uses uses the $T_{SF} = 0.95$ threshold line. The sample size for CLAGN candidate selection is 2,698 AGN for the visual method, and 2,336 AGN and 12,159 SF sources for the variability threshold method. Since we remove low

resolution lightcurves and sources without r_{psf} in the SMSS data, we obtain a discrepancy in the AGN sample size for the two methods. Overall, $\sim 10\%$ of known AGN were selected as possible CLAGN candidates. After removing known CLAGN and already observed candidates (see Chapter 4), we present two CLAGN candidate lists with 28 turn-off candidates and 172 turn-on candidates respectively. The candidate lists are available in Appendix A.

6dFAGN Type	Visual Method			Variability Threshold			
	AGN Count	CLAGN candidates	CLAGN Candidate Fraction	AGN Count	Variable	Non-variable	CLAGN Candidate Fraction
1	37	6	0.135	25	17	**8**	0.320
1.2	92	4	0.043	65	57	**8**	0.123
1.5	173	9	0.052	144	126	**18**	0.125
1.8	8	5	0.625	7	**7**	0	1.000
1.9	176	99	0.563	153	**78**	75	0.510
2	2212	157	0.071	1942	**139**	1803	0.072
Total	2698	279	0.103	2336	424	1912	0.110

Table 3.2: CLAGN candidates per AGN type for both methods. For the variability threshold method with $T_{SF} = 0.95$, non-variable 6dFGS type 1-1.5 and variable 6dFGS type 1.8-2 AGN are selected as CLAGN candidates (marked in bold font).

6dFAGN Type	Visual Method only	Both Methods	Threshold Method Only
1.0	1	3	5
1.2	1	1	7
1.5	1	6	12
1.8	0	4	3
1.9	15	71	7
2.0	56	65	74

Table 3.3: CLAGN candidates selected by either methods. The visual method sample has been modified to keep only the AGN used in the threshold method.

A table comparing CLAGN candidates obtained from the two methods using the AGN sample for the variability threshold method is presented in Table 3.3. We find a significant discrepancy in the type-2 turn-on CLAGN candidate list between the visual and threshold methods. However, the visual method is not a reliable measure of the variability as ambiguous lightcurves can be classified as either variable or non-variable, depending on the human classifier, and the result can also change when repeated after a break in time. The visual classification was done to provide an expedient candidate list for observation, before the more robust variability threshold method was developed. Therefore, we use the results from the visual classification

for spectroscopic follow up of the candidates, and use the results from the variability threshold method for analysis.

Figure 3.5 plots the different AGN types, with SF sources and the $T_{SF} = 0.95$ line as a reference. A few AGN of types 1-1.5 are well within the cloud of SF sources, which are strong turn-off CLAGN candidates. The distribution of type 2 AGN is tight below the line, with an extended region above the line sparsely populated, which are strong turn-on CLAGN candidates. Surprisingly, none of the type 1.8 AGN lie below the threshold line. We also see similar fraction of type 1.9 above and below the line. The distribution of types 1.8 and 1.9 AGN is not clear from the plot, which is in part due to the small sample size. A further discussion on these two types is presented in Chapter 5.
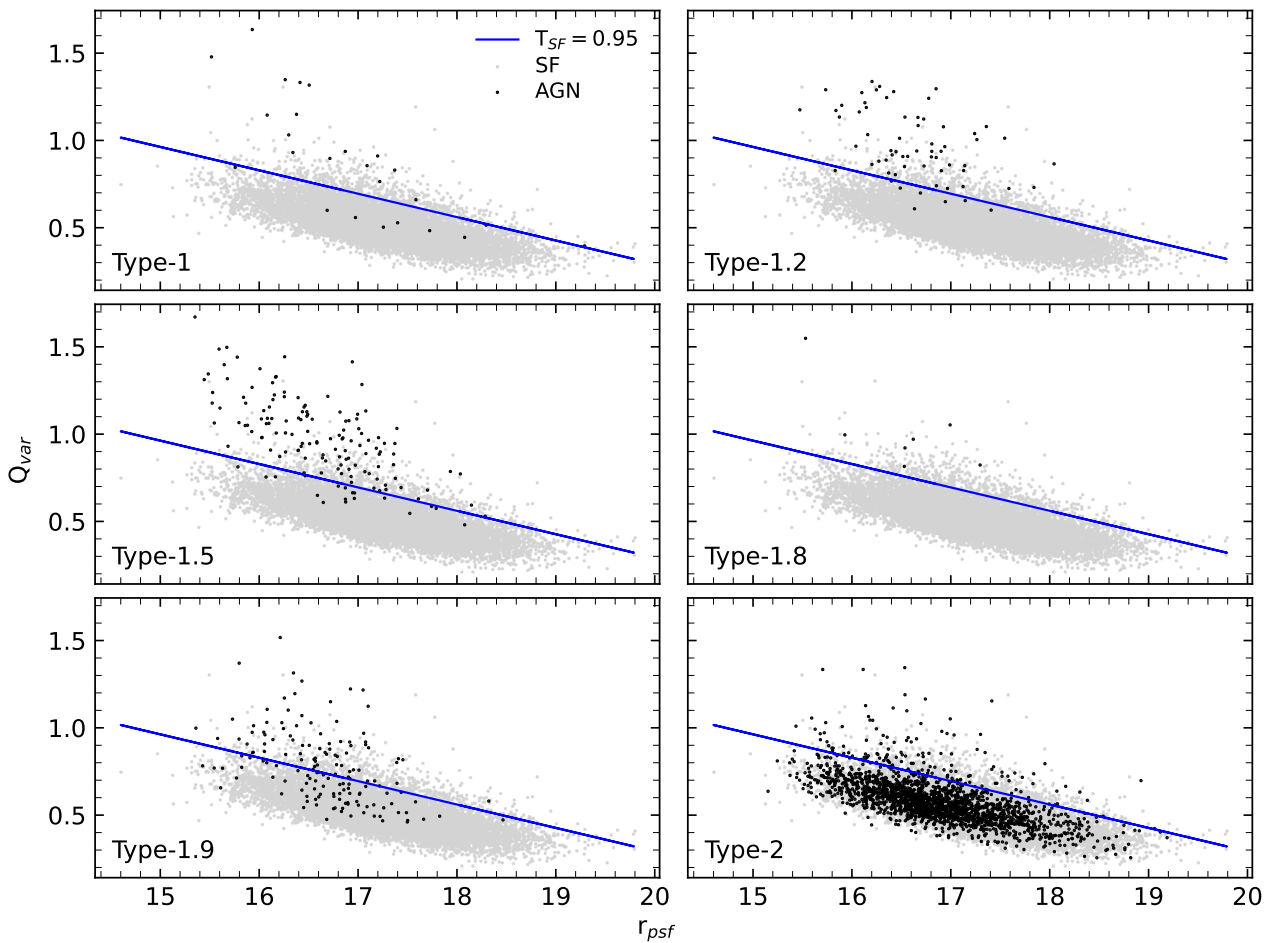

Figure 3.5: All six Seyfert types overlaid over SF sources and the threshold line corresponding to $T_{SF} = 0.95$ (Equation 3.7). AGN points above the line are marked as variable sources, and AGN points below the line are marked as non-variable sources.

Chapter 4

Spectroscopic Observations and Comparison

The selected CLAGN candidates are just that, candidates. The next step would be to compare spectra from different epochs to verify changes in broad emission line width and intensity. This work compares spectra from 6dFGS (2001-2009) with current day (May-June 2022) follow up spectra. In this chapter, we list the observed targets (Section 4.1), outline the method used to extract spectra from current day spectra (Section 4.2), and present spectroscopic evidence of confirmed CLAGN (Section 4.3).

4.1 Observed Targets

PhD student, Samuel Lai, observed 72 CLAGN candidates between 26th May and 2nd June that have been presented in this thesis. The observations were made using the ANU 2.3m Wide-Field Spectrograph (WiFeS) instrument, using $R_{3000} + B_{3000}$ gratings. The data reduction via the `PyWiFes` pipeline was performed by Dr. Christopher Onken. The observed targets are listed in Table 4.1. These targets range between RA of 9h and 20h and are a subset of the CLAGN candidate list from the visual method (see Section 3.3).

Table 4.1: Observation log

SkyMapper Object ID	6dFGS Name	RA	Dec	mag r_{psf}	z	6dFAGN Type	Epoch	Exp Time (s)
80589899	g0913233-255925	138.3471	-25.9901	17.2560	0.0546	1	20220601	900
81060549	g0916467-242042	139.1947	-24.3449	16.6126	0.0368	1.9	20220601	750

Table 4.1 continued from previous page

78772924	g0922229-340343	140.5955	-34.0619	16.7216	0.0442	1.9	20220601	750
89797277	g0951550-064923	147.9793	-6.8229	14.9746	0.0145	1.9	20220526	400
89851276	g1001422-103331	150.4258	-10.5585	16.1397	0.0333	2	20220602	600
433498538	g1007009-430328	151.7538	-43.0576	15.4051	0.0208	2	20220602	400
79479845	g1007450-411954	151.9379	-41.3317	16.1669	0.0194	2	20220602	600
89958962	g1007504-090445	151.9602	-9.0792	16.7823	0.0669	1.9	20220526	750
80294510	g1007550-351347	151.9790	-35.2296	15.5980	0.0148	2	20220602	400
90985522	g1014116-124043	153.5483	-12.6787	16.5366	0.0681	1.8	20220526	750
92349617	g1038209-100660	159.5869	-10.1167	16.1136	0.0289	2	20220602	600
412521822	g1049464-434050	162.4433	-43.6805	16.4817	0.0448	2	20220602	600
82828658	g1051463-415947	162.9429	-41.9964	17.0933	0.0905	2	20220602	900
83012942	g1054326-413625	163.6358	-41.6070	17.1629	0.0579	2	20220602	900
92403414	g1101298-122659	165.3744	-12.4495	15.9024	0.0259	2	20220601	400
92852613	g1103168-065417	165.8199	-6.9047	16.2550	0.0260	1.9	20220601	600
84733217	g1105372-364750	166.4052	-36.7972	16.6003	0.0915	2	20220601	750
93248265	g1123323-083931	170.8845	-8.6585	15.5496	0.0120	2	20220601	400
86734596	g1134475-361011	173.6981	-36.1698	17.7903	0.0095	1.5	20220526	1200
91621777	g1138510-232135	174.7125	-23.3598	15.5888	0.0272	1.9	20220526	400
85043405	g1138589-380042	174.7455	-38.0117	18.2697	0.0090	1	20220526	1500
91991082	g1148026-184952	177.0111	-18.8311	18.2929	0.0335	1.5	20220526	1500
91694847	g1156158-205430	179.0660	-20.9082	15.7208	0.0423	2	20220601	400
94852591	g1211143-393327	182.8096	-39.5575	16.5427	0.0609	2	20220601	750
97275597	g1235322-345447	188.8843	-34.9131		0.0533	2	20220601	1800
106382562	g1238084-091412	189.5350	-9.2366	16.9943	0.0707	2	20220601	750
97547124	g1246107-314836	191.5445	-31.8098	16.3307	0.0564	2	20220602	600
106327166	g1249104-114925	192.2934	-11.8236	16.7147	0.0746	1.9	20220526	750
104764983	g1251324-141316	192.8849	-14.2212	15.3599	0.0148	1.9	20220526	400
98156119	g1254564-265702	193.7348	-26.9505	15.5311	0.0592	1.8	20220526	400
105169587	g1344330-225801	206.1374	-22.9671	17.2661	0.0796	2	20220527	900
108087534	g1349195-230042	207.3310	-23.0117	16.3690	0.0405	2	20220527	600
99700135	g1354154-374633	208.5642	-37.7759	15.6813	0.0509	2	20220602	400
102266781	g1356131-274458	209.0546	-27.7495	16.5088	0.0500	2	20220602	750
109721266	g1401018-111223	210.2577	-11.2064	16.2471	0.0365	2	20220602	600
101686253	g1401157-322943	210.3154	-32.4952	16.6811	0.0600	1.9	20220602	750
101744667	g1405106-310335	211.2940	-31.0597	16.6485	0.0232	1.5	20220526	750
102689258	g1410293-241748	212.6219	-24.2966	16.4122	0.0417	2	20220527	600
108339531	g1412197-214708	213.0820	-21.7855	15.4517	0.0441	2	20220527	400
108449290	g1412348-185625	213.1450	-18.9403	16.5756	0.0416	2	20220527	750
108349978	g1415440-220050	213.9334	-22.0138	17.4323	0.0494	2	20220527	900
110399311	g1423582-050009	215.9925	-5.0024	16.9088	0.0558	2	20220527	750
101281975	g1428588-313935	217.2449	-31.6597	15.3514	0.0233	2	20220527	400
103030136	g1437457-271803	219.4403	-27.3009	16.8829	0.0649	1.9	20220526	750

Table 4.1 continued from previous page

308543986	g1452310-422625	223.1293	-42.4402	15.7940	0.0496	1.9	20220526	400
109225918	g1453235-182615	223.3480	-18.4376	16.4039	0.0650	1.9	20220526	600
307104697	g1457221-401359	224.3421	-40.2329	16.5704	0.0326	1.9	20220526	750
307616075	g1459014-423454	224.7560	-42.5815		0.0099	2	20220527	1800
310181797	g1508046-424445	227.0192	-42.7457	16.8939	0.0565	2	20220527	750
310630678	g1515380-440648	228.9083	-44.1131	16.0719	0.0315	2	20220527	600
309557752	g1526342-402821	231.6426	-40.4724	16.5612	0.0498	2	20220527	750
120649442	g1550338-254349	237.6411	-25.7304		0.0461	1.9	20220526	1800
115496036	g1554002-365535	238.5008	-36.9263	18.2943	0.0934	1	20220526	1500
167632502	g1556253-202829	239.1054	-20.4746	16.8333	0.0618	1.9	20220526	750
119612141	g1558468-320020	239.6951	-32.0054	16.4285	0.0257	1.9	20220602	600
194300354	g1630074-001136	247.5309	-0.1935	16.9622	0.0466	1.5	20220526	750
171475200	g1636268-211835	249.1115	-21.3097	17.7659	0.0266	1.2	20220526	1200
192952618	g1646104-112404	251.5433	-11.4012	16.0689	0.0741	1.5	20220526	600
194988540	g1658419-031417	254.6746	-3.2380	16.9275	0.0826	1.9	20220526	750
195000846	g1700567-030646	255.2363	-3.1128	17.3939	0.0802	1.9	20220526	900
193620585	g1703359-101227	255.8996	-10.2074	17.7235	0.0989	2	20220526	1200
200359164	g1709224-014012	257.3433	-1.6700	17.6476	0.0930	2	20220601	1200
196785035	g1721290-070956	260.3706	-7.1654	17.9519	0.0365	2	20220601	1200
211838425	g1902376-375847	285.6567	-37.9797	16.5065	0.0317	1.9	20220526	750
211581293	g1907504-392332	286.9605	-39.3919	15.7977	0.0726	1.9	20220526	400
262141668	g1920272-162915	290.1133	-16.4876	16.6024	0.0860	1.9	20220527	750
263996974	g1922540-185543	290.7249	-18.9284	16.7426	0.0394	2	20220602	750
232036773	g1944275-291211	296.1147	-29.2031	15.8775	0.0246	1.9	20220602	400
234731593	g2010499-310931	302.7080	-31.1585	17.4081	0.0857	1.9	20220602	900
233071576	g2015255-373043	303.8560	-37.5117	15.7047	0.0208	2	20220602	400
487178631	g2018181-444825	304.5755	-44.8068	14.9030	0.0084	2	20220602	400
298010857	g2038102-203149	309.5423	-20.5302	16.3926	0.0362	1.9	20220602	600

4.2   Extracting WiFeS Spectra

Comparing spectra from different instruments is not straightforward, as the instruments have different specifications and observational techniques. For example, the 6dFGS spectra has a lower spectral resolution than the WiFeS spectra, which may make narrow lines in WiFeS spectra more pronounced compared to 6dFGS spectra. Since the 6dFGS is a past survey, we need to mimic the new observations to be as similar as possible to the 6dFGS observations.

WiFeS has a pixel scale of 1", while 6dFGS used optical fibres of 6.7" diameter. WiFeS can provide a spectrum of just the nucleus of a target galaxy with its small pixel scale at our

sample range of $z < 0.1$. This ignores stellar light from the extended regions of the host galaxy. 6dFGS spectra includes some light from these extended regions in its spectra, which means some emission lines specific to AGN, such as Hα or Hβ, can appear to be stronger in the WiFeS spectra. To prevent this, light from a circular aperture with 6.7" diameter is added to obtain the spectra. See Figure 4.1 for a representation of the difference in pixel scale and approximation of the circular aperture.

WiFeS has a slight offset in the wavelength domain over different slits (columns in Figure 4.1) due to its curved wavelength solution. Selecting the area for sky subtraction that is on a slit far from the target can result in an offset in subtraction. We therefore try to use an area of sky that is on the same column of the target object for sky subtraction. We do not use an annulus around the target for subtraction as it may subtract stellar light from the host galaxy.
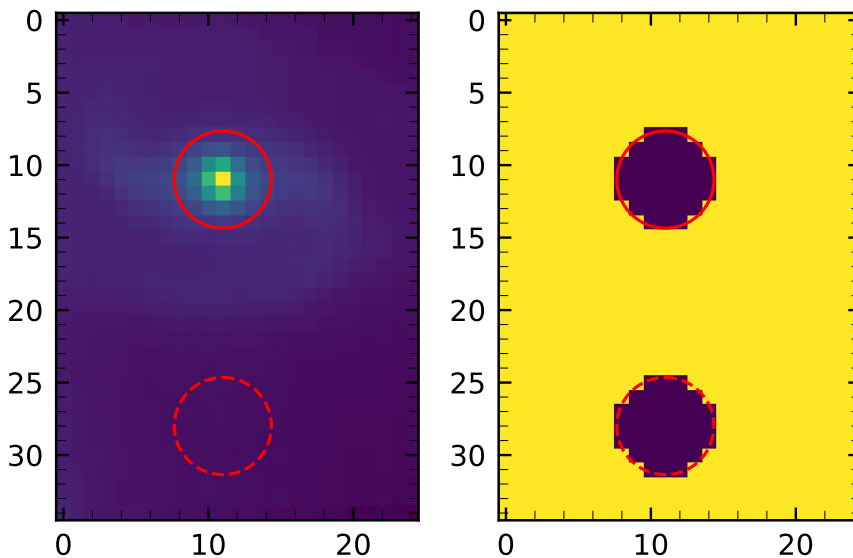
Figure 4.1: Left: Image of an AGN (**g1007504-090445**) from WiFeS red wing. Pixel scale for the image is 1". The solid red circle mimics 6dFGS aperture size of 6.7". The dashed red circle is the area of sky used for sky subtraction. **Right:** Translation of an ideal circular aperture to an approximate mask (dark pixels).

The flux measurements of the the WiFeS and 6dFGS spectra are not of similar units. Since the comparison is inherently relative, we normalise spectra to the OIII line flux. The OIII line is not expected to change within the ~15 year timescale between the two epochs.

4.3 Confirmed CLAGN

The emission lines used to look for comparing spectra are the Balmer lines, Hα, Hβ and occasionally Hγ and higher transitions if available. Recall that 6dFAGN types of AGN are determined from the FWHM of Hα and Hβ lines. We can identify true CLAGN from the can-

didate list by visually comparing the Balmer lines. We confirm six CLAGN from the observed targets (see Table 4.2), and label them as either turn-on or turn-off depending on whether the Balmer lines in the WiFeS spectra broaden or weaken with respect to the 6dFGS spectra. We go through each of the confirmed CLAGN below. We also provide an estimated WiFeS type by eyeballing the new spectra. Lightcurves and 6dFGS+WiFeS spectra of the remaining 66 observed targets are listed in Appendix B.

6dFGS Name	SMSS ID	6dFAGN Type	z	WiFeS Type	CLAGN Type	Figure
g0913233-255925	80589899	1.0	0.0546	2	Turn-off	4.2
g1630074-001136	194300354	1.5	0.0466	1.9	Turn-off	4.3
g1007504-090445	89958962	1.9	0.0669	1.5	Turn-on	4.4
g1038209-100660	92349617	2.0	0.0289	1.2/1.5	Turn-on	4.5
g1415440-220050	108349978	2.0	0.0494	1.2/1.5	Turn-on	4.6
g1254564-265702	98156119	1.8	0.0592	1.9	Turn-off	4.7

Table 4.2: CLAGN confirmed with spectroscopic evidence. The WiFeS types are estimated by eye. A robust determination of the new CLAGN would involve spectral line fitting of the Hβ and OIII lines.

g0913233-255925 (Figure 4.2): The 6dFAGN catalogue has marked this source as a type-1 AGN as the 6dFGS spectrum has broad Balmer lines, including a strong Hγ. However, the ATLAS lightcurve does not show stochastic variability from late 2017. The current day WiFeS spectrum does not even have a Hβ feature, and the Hα line has weakened significantly. This source is a clear turn-off CLAGN, with the type change occurring before late 2017.

g1630074-001136 (Figure 4.3): This source is marked as a type-1 AGN in the 6dFAGN catalogue. The 6dFGS spectrum has broad Hα and Hβ lines, but the lines are weaker than that of type-1 AGN. In the lightcurve, we see weak variability, almost periodic, between mid-2017 and end of 2019. The variability stops in early 2020, and the broad lines vanish in the WiFeS spectrum. This is a turn-off CLAGN, with the type change occurring within the lightcurve period. Therefore, any spectra of the AGN during its weakly variable phase would shed more light on the type change process.

g1007504-090445 (Figure 4.4): This source, marked as type-1.9 in the 6dFAGN catalogue, shows clear variability in its lightcurve. The WiFeS spectrum also shows stronger and broader Hα line compared to the 6dFGS spectrum and also a newly emerged broad Hβ. This source is a turn-on CLAGN, but the exact epoch of type change is not available from the lightcurve.
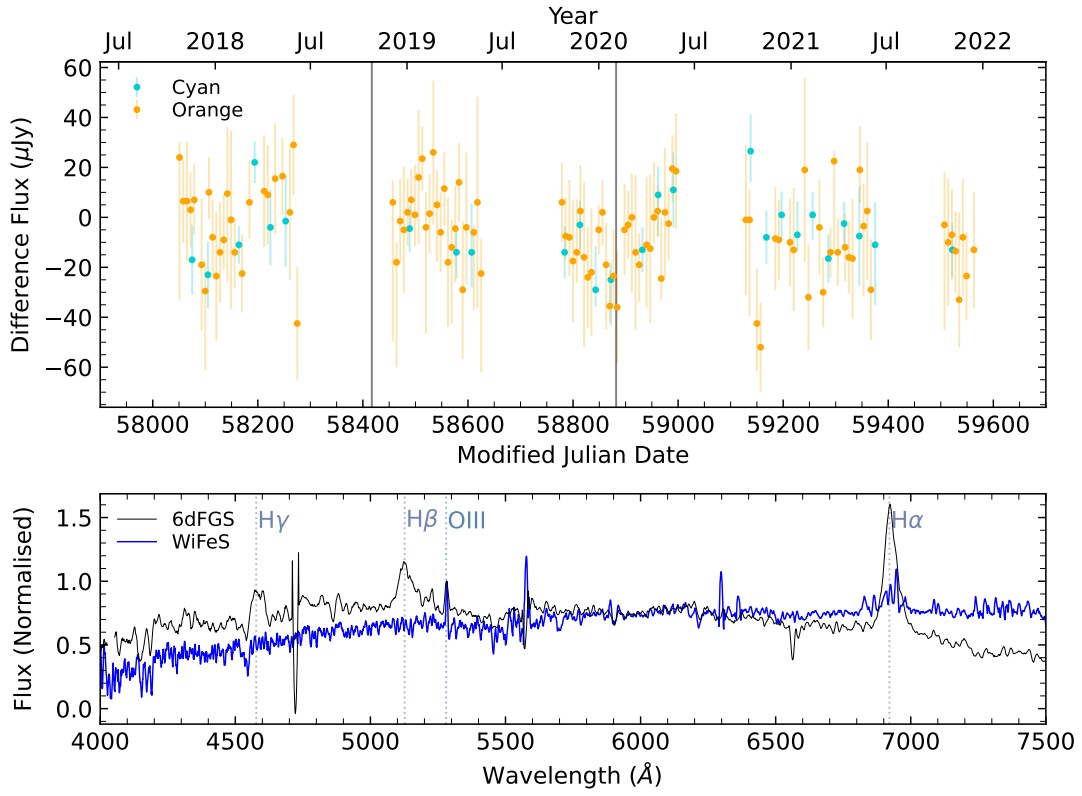
Figure 4.2: ATLAS lightcurve (top) and 6dFGS+WiFeS spectra (bottom) for **g0913233-255925** with **6dFAGN type-1**. Confirmed Turn-Off CLAGN.
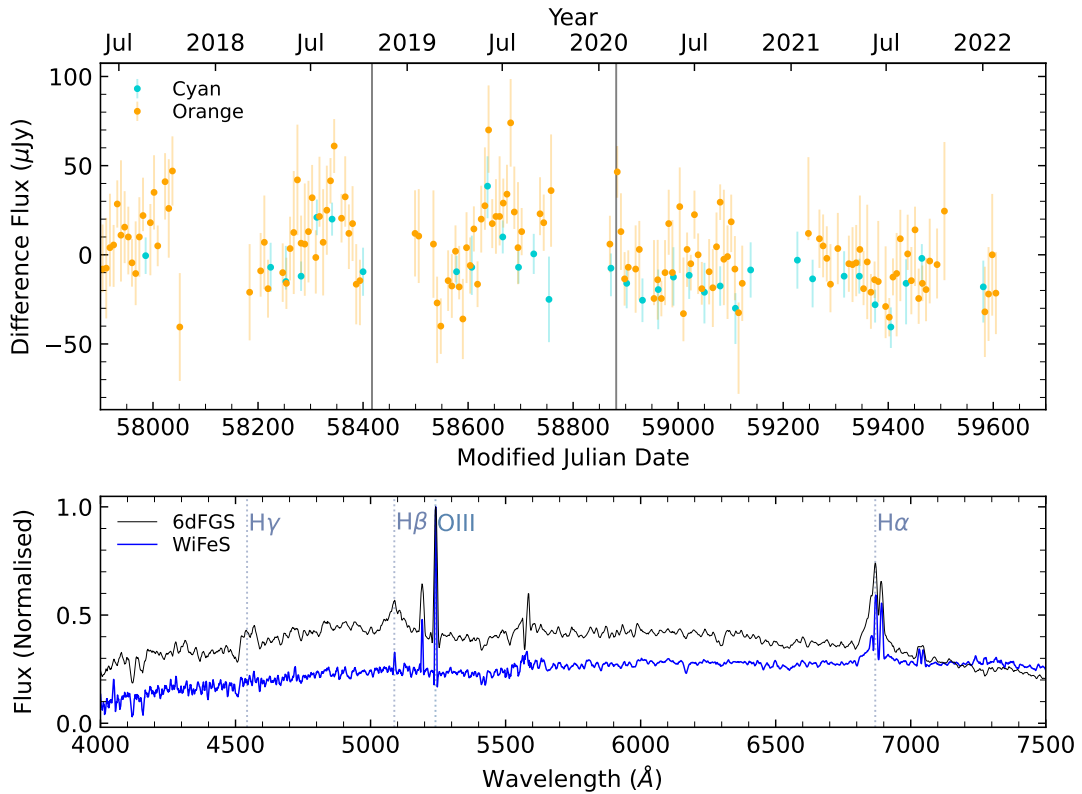

Figure 4.3: ATLAS lightcurve (top) and 6dFGS+WiFeS spectra (bottom) for **g1630074-001136** with **6dFAGN type-1.5**. Confirmed Turn-Off CLAGN.
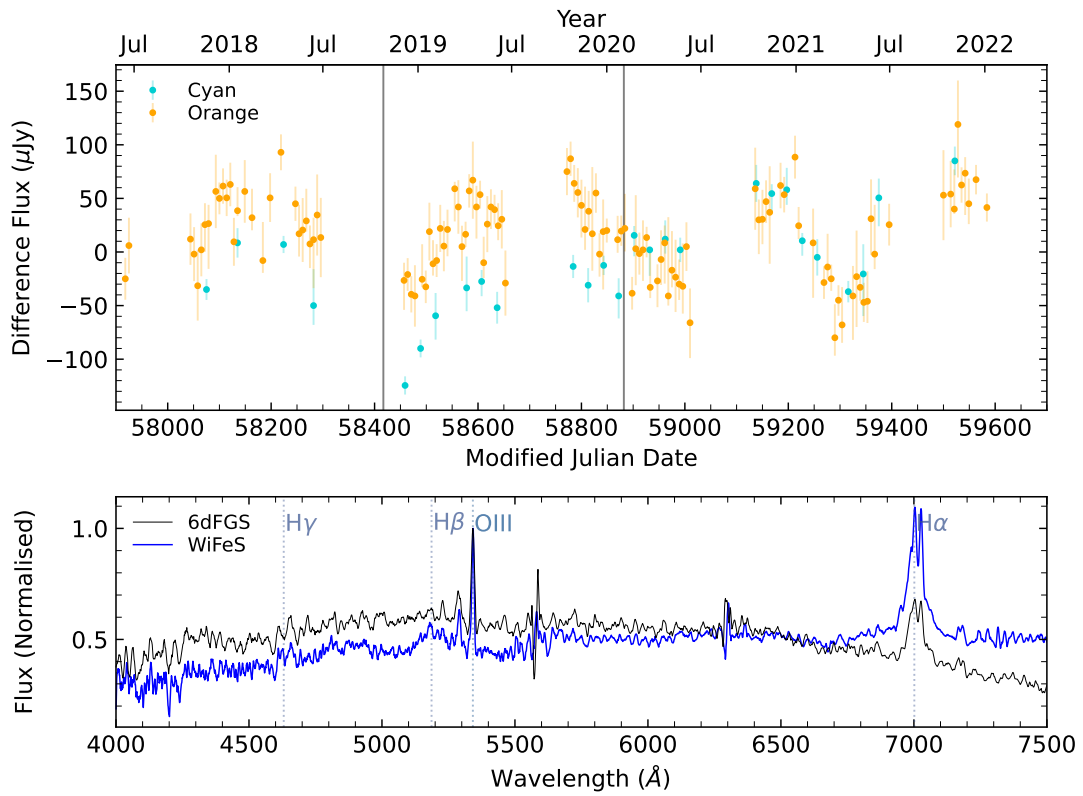
Figure 4.4: ATLAS lightcurve (top) and 6dFGS+WiFeS spectra (bottom) for **g1007504-090445** with **6dFAGN type-1.9**. Confirmed Turn-On CLAGN.
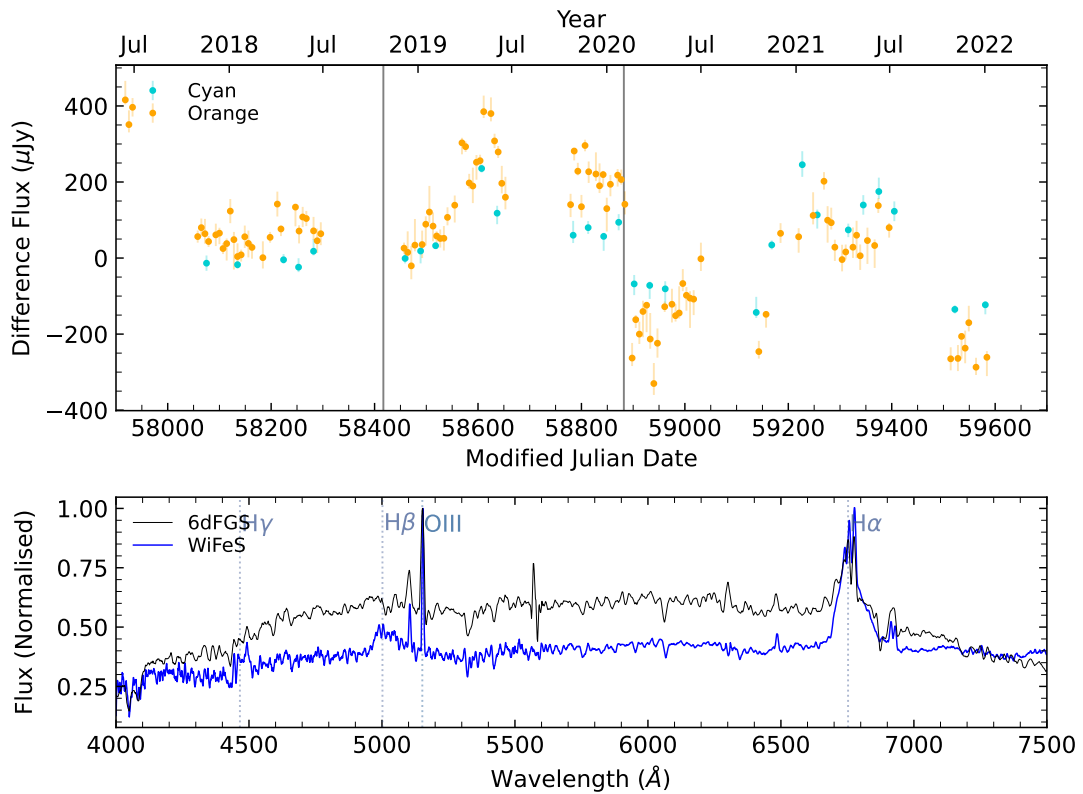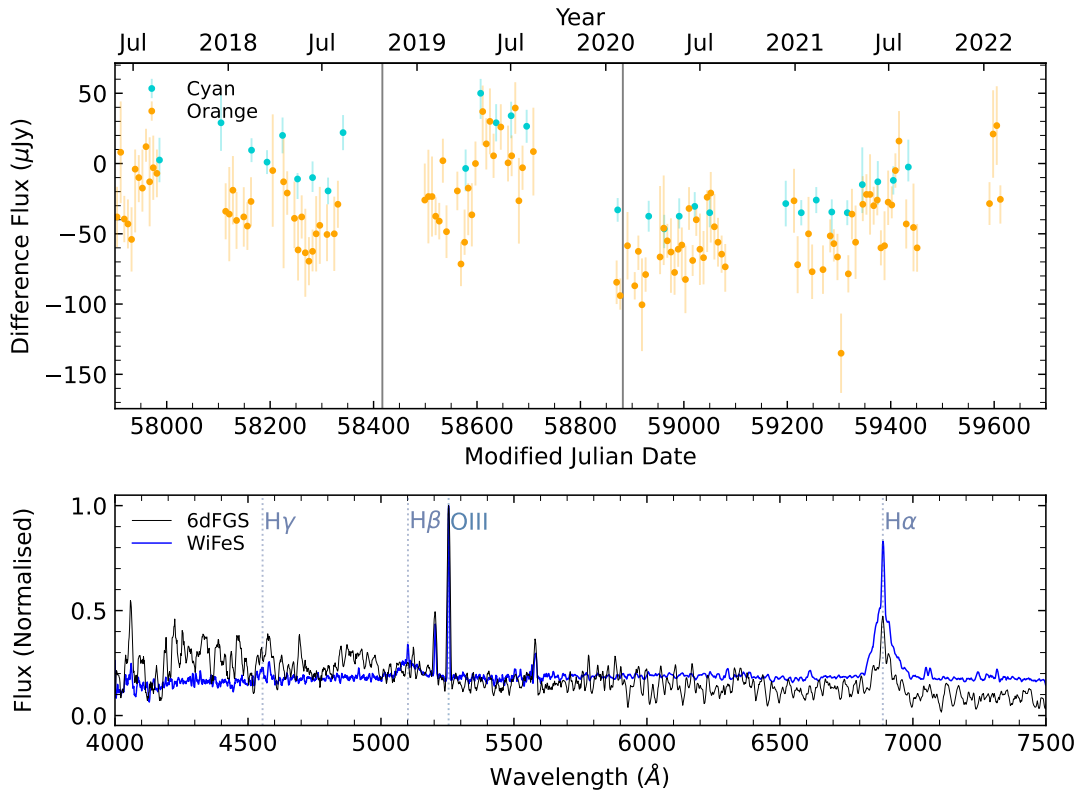

Figure 4.5: ATLAS lightcurve (top) and 6dFGS+WiFeS spectra (bottom) for **g1038209-100660** with **6dFAGN type-2**. Confirmed Turn-On CLAGN. Note step-discontinuity at second wallpaper change.

g1038209-100660 (Figure 4.5): The source is marked as a type-2 AGN in the 6dFAGN catalogue. The lightcurve has a step discontinuity at the second major wallpaper change, which must be accounted for when looking for the variability pattern. We notice stronger Hα in WiFeS spectrum compared to the old 6dFGS spectrum. However, the weak but broad Hβ that has appeared in the newer spectrum is strong evidence that this source is a true turn-on CLAGN.

g1415440-220050 (Figure 4.6): Another source marked as type-2 in the 6dFAGN catalogue. We once again see discontinuity around the second wallpaper, but the most recent measurements show a steady increase in flux. The spectrum also shows a much stronger and broader Hα in the WiFeS spectrum relative to the OIII line, and an additional broad Hβ line. This is a clear case of a turn-on CLAGN.

Figure 4.6: ATLAS lightcurve (top) and 6dFGS+WiFeS spectra (bottom) for **g1415440-220050** with **6dFAGN type-2**. Confirmed Turn-On CLAGN. Note possible step-discontinuity at second wallpaper change.

g1254564-265702 (Figure 4.7): This source is an interesting case as the CLAGN type change occurs within the lightcurve period. The source was marked as type-1.8 in the 6dFAGN catalogue, but the spectra shows weaker and narrower Hα and weaker Hβ and Hγ relative to the OIII line. The lightcurve shows variability from mid-2017 to mid-2018, and a transient event (Transient *2019hsf*, Delgado et al. (2019)) between the two major wallpaper changes. However, there is no variability after the second major wallpaper change, and it continues to be

non-variable throughout. This would explain the lack of broad lines in the WiFeS spectra. The variability before 2019 suggests the AGN was possibly type 1-1.5, but spectroscopic evidence would be required. The AGN type change could have been caused by the transient event itself (see Section 5.3).
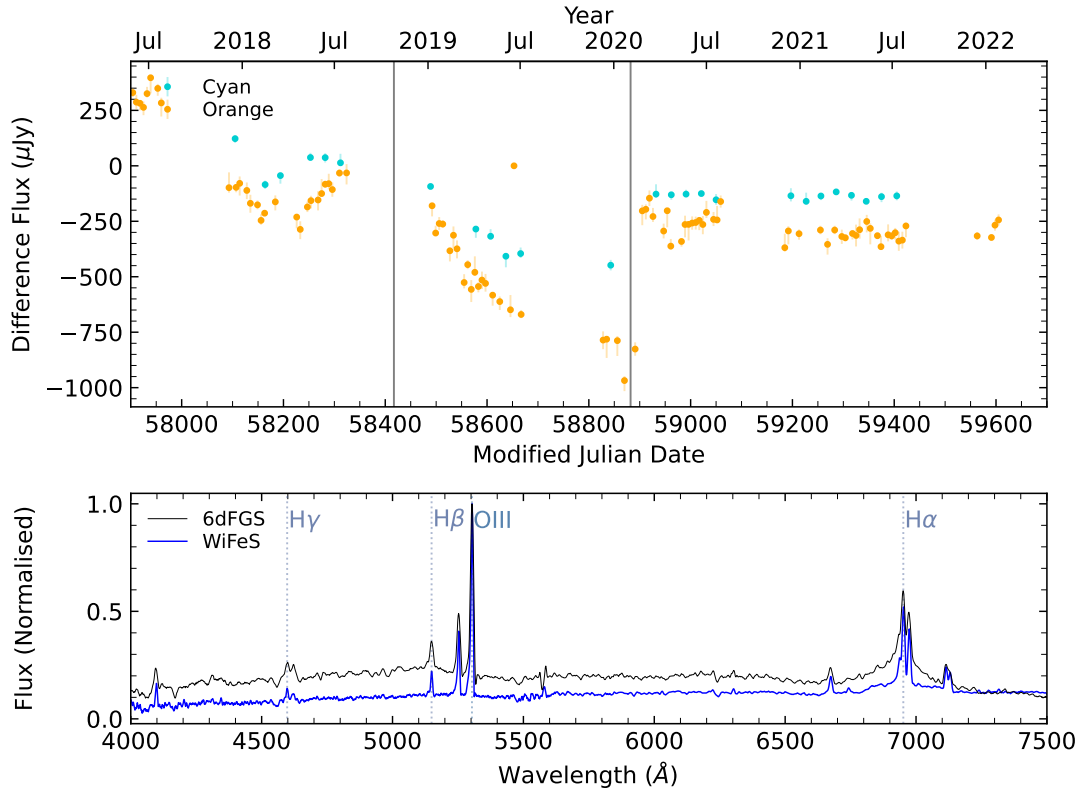

Figure 4.7: ATLAS lightcurve (top) and 6dFGS+WiFeS spectra (bottom) for **g1254564-265702** with **6dFAGN type-1.8**. Confirmed Turn-Off CLAGN. Note step-discontinuity at both major wallpaper changes.

Chapter 5

Discussion

In this chapter, we reflect on the results presented in this work. In Section 5.1, we discuss the limitations of our method and compare our results with the SkyMapper colour method of finding CLAGN. We also discuss the lightcurve variability of AGN types 1-1.5 (Section 5.2.1), AGN types 1.8-1.9 (Section 5.2.2) and compare the variability of type-2 AGN and SF sources (Section 5.2.3). Finally, we discuss the relation between AGN type changes and their lightcurves in Section 5.3.

5.1 Reliability of the Variability Threshold

5.1.1 Limitations

The variability threshold method is ultimately a binary classification that marks each source as either variable or non-variable. The threshold line, T_{SF}, divides the variability distribution by selecting a single variability range beyond which the lightcurve is marked variable. This does not distinguish weakly variable objects from non-variable objects below the line. The SF sources are a good proxy for a non-variable AGN, as we see from the distribution of non-variable type-2 AGN overlaid on SF sources in Figure 3.5. However, we do not have a similar proxy for variable extragalactic objects as stochastic variability itself is unique to AGN. If such a proxy for variable sources does exist, we do not know the extent of overlap between the variable and non-variable distributions. As a result we use existing typing of types 1-1.5 to estimate the distribution of variable AGN, which has a much lower sample size compared to SF. A direct consequence of this is that the variability threshold method is more reliable in finding variable sources from a sample of non-varying sources, but not vice versa. That is, the turn-on

candidate list is more pure compared to the turn-off candidates. This asymmetric candidate selection efficiency mostly affects sources that lie close to the T_{SF} line.

The threshold also does not distinguish between sources that vary throughout the lightcurve period and sources that have periods of both variability and non-variability across the lightcurve period. We have seen such an example with 6dFGS source **g1254564-265702**, where the lightcurve has a variable period, a TDE period, and a non-variable period within 5 years. The threshold classifies this source as a variable object, and marks it as a turn-on candidate, but the spectroscopic comparison (Figure 4.7) reveals this as a turn-off CLAGN. This further amplifies the asymmetric effect of incomplete turn-off CLAGN candidates, as turn-off CLAGN that show variability only in the first few years of the lightcurve would still be marked as variable, but short flares in type-2 AGN would be marked as a CLAGN candidate. We remove SNe/TDEs from SF and type-2 AGN only to prevent the events contaminating these flares. Removing event-contaminated type 1-1.5 AGN would not change the turn-off candidate list.

The CLAGN candidate selection is also dependent on the lightcurve period. The older 6dFGS spectra are from more than ten years before the start of the lightcurve period. Due to limited lightcurve data, we miss any CLAGN that changed type and reverted back to the previous type before the lightcurve period.

5.1.2   Comparison with SkyMapper $u - v$ Colour Method

We compare our method to previous work by Wolf et al. (2020); Hon et al. (2022) (colour method). They select CLAGN candidates from the 6dFAGN catalogue and then confirm CLAGN by comparing 6dFGS spectra and recent WiFeS spectra. The difference between the colour and variability methods is the candidate selection. The colour method searches turn-on AGN by inspecting the recent $u - v$ colour of 6dFAGN types 1.8-2, using the SMSS survey data. Sources with colours similar to type 1-1.5 were marked as candidates. The observations on WiFeS date between December of 2017 to November of 2020, with a few cases of repeat observations. The colour method also favours turn-on CLAGN over turn-off CLAGN in selecting candidates.

The two colour method papers provide a sample of 36 CLAGN, including CLAGN from other methods. We do not exclude CLAGN from other methods in our comparison so as to obtain a more comprehensive test of our method. We have lightcurves for 22 of the known CLAGN due to the redshift limitation of $z < 0.1$. Moreover, we include seven additional CLAGN not listed in the papers as they were confirmed after Hon et al. (2022) was published. Ten CLAGN are

absent in our sample as the lightcurves have less than 90 weeks' worth of data, or the SkyMapper r_{psf} magnitude is unavailable. We compare the remaining 19 CLAGN in our sample and plot them in Figure 5.1. All 15 known turn-on CLAGN are marked as CLAGN candidates by the variability threshold method. However, none of the four known turn-off CLAGN are among our candidates.

Furthermore, we compare unobserved candidates from the colour method with the candidate list from the variability method. We find that 42 candidates from the colour method overlap our search sample, of which the variability method identifies only 7 turn-on and 5 turn-off candidates. Of the remaining 30 candidates from the colour method, 25 are turn-off candidates. This discrepancy in the candidate list is because the colour method identifies turn-off candidates by changes in the $u - v$ colour at distinct epochs, while the variability method marks turn-off candidates only if there is no variability throughout the lightcurve period.
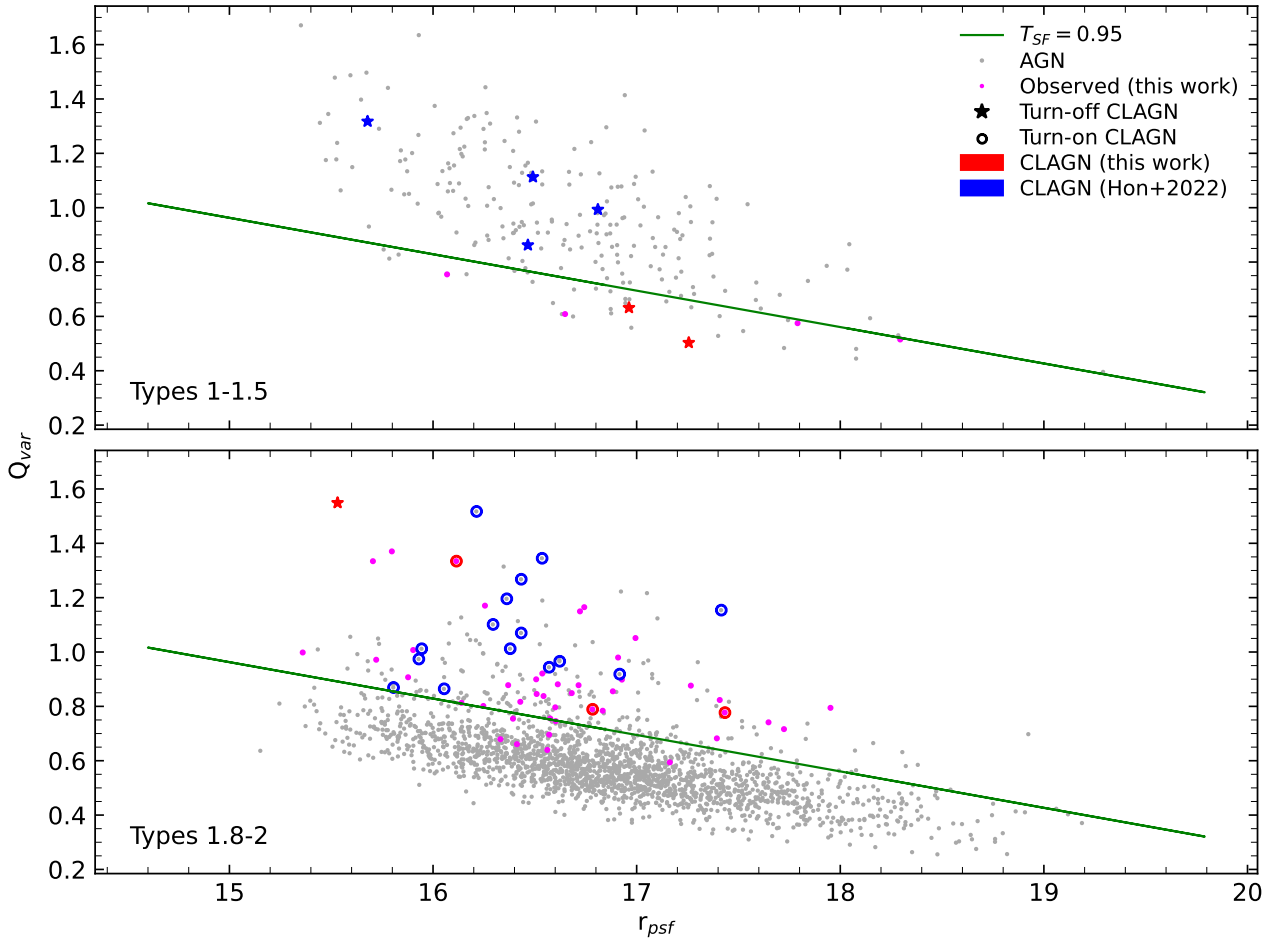
Figure 5.1: 12 known CLAGN from Hon et al. (2022) and 7 newer unpublished CLAGN by Wei Jeat (Jack) Hon, which overlaps with the search sample in this work. The $T_{SF} = 0.95$ line is shown for reference. The AGN are grouped into 6dFAGN types 1, 1.2, 1.5 and 6dFAGN types 1.8, 1.9, 2. The turn-on and turn-off CLAGN are marked differently, which points out the position of **g1254564-265702**, the lone turn-off CLAGN in the second panel. The observed CLAGN candidates are from the visual method listed in Section 4.1. The four turn-off AGN above the threshold line in the top panel are CLAGN that are not in our turn-off candidate list.

These four sources have 6dFAGN type-1.5, and are expected to vary. Their lightcurves pre-

sented in Figure 5.2 indeed show variability. We notice that the first two lightcurves follow a similar pattern of weak variability until around MJD 59000. In the recent two years, both sources undergo a period of brightening. These sources have at least one spectrum taken before MJD 59000, which coincides with the non-variable period of these sources. Hon et al. (2022) observed **g1340153-045332** with type-1.9 at MJD 58906 and again type-1.5 at MJD 59016 and MJD 59308. The second source, **g1839358-354124**, is observed twice at the period of weak variability, both resulting in type-1.8. We have caught these two sources in the act of a turn-on changing look event. As both of these sources are variable, our method does not mark them as CLAGN candidates as the variability threshold only notices variability after MJD 59000. This is a direct consequence of using a single variability parameter for the entire period of the lightcurve, which affects only turn-off CLAGN.

The bottom two 6dFAGN type-1.5 AGN in Figure 5.2 are from newer (yet to be published) results from the colour method. These show a pattern of a flare followed by a steady decline into non-variability. The new spectroscopic observations were completed after the latest available lightcurve measurement, but the lightcurve suggests these two AGN are in a low accretion state over the past two years. In order to confirm whether we have captured these AGN in a turn-off changing look event, we would need spectroscopic evidence of type 1-1.5 during the flare at around MJD 58600.

By comparing the two methods, we find that the variability threshold method is not efficient in finding turn-off CLAGN, in exchange for a more reliable turn-on CLAGN candidate list. Any signs of brightening in types 1.8-2 AGN within an AGN's history provided by the lightcurve will be marked as a CLAGN candidate. The 6dFGS reference for AGN types is disjointed from the ATLAS lightcurves by more than a decade. This is longer than the timescale of AGN type changes, as suggested by the handful of true CLAGN discussed in this work. While we have evidence that the variability threshold method does include true CLAGN in its candidate list, more recent typing of AGN or a much longer lightcurve is required to improve our CLAGN candidate list. Furthermore, the variability threshold method is not equipped to catch the type change in action and a different approach is required to analyse variability history using a lightcurve.

5.2 Variability Analysis

Stable fluctuations in emission over short timescales is a characteristic unique to AGN in extragalactic astronomy and the variations can be detected across the entire electromagnetic
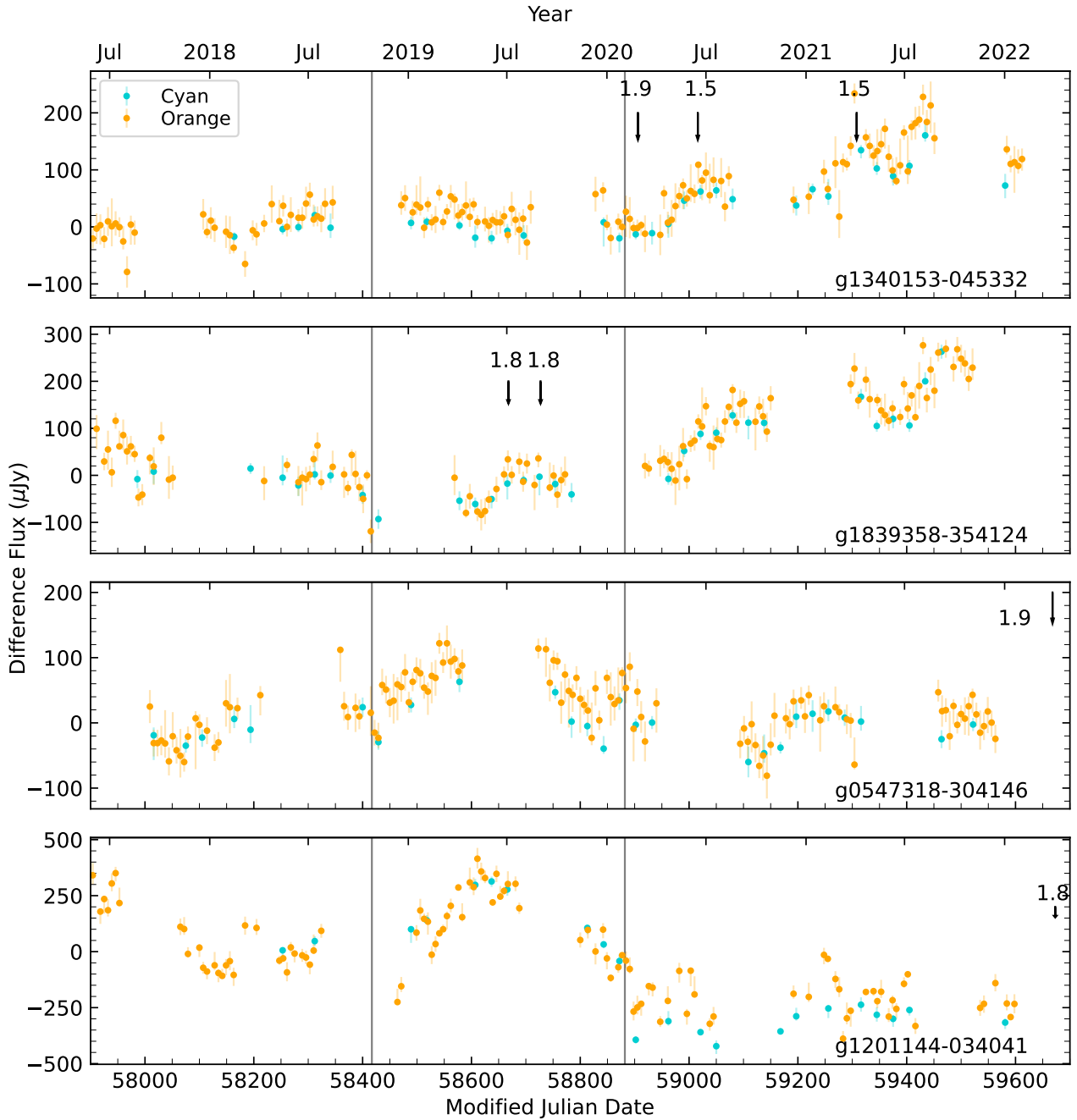
Figure 5.2: 6dFAGN type 1.5 CLAGN from Hon et al. (2022) that are not marked as a CLAGN candidates in this work. The arrows mark the MJD of observation, and the annotated text marks the corresponding observed type.

spectrum. Long term variability is also used as an identifier for low mass active galaxies (Baldassare et al., 2018, 2020). AGN variability was first discovered in quasars and played a role in determining the size of the powerful central light source. The short variation timescales would constrain the size of the variable source based on light travel distance (Collier et al., 1999). In contrast, SF galaxies are not expected to show short term variability, as consistent flux variation must originate from a coherent source and star forming regions are spatially extended. It is unlikely that all star forming regions of a galaxy collectively increase or decrease in brightness in timescales of days or weeks. Inconsistent variability of different star forming

regions and stellar sources are expected to average out over the entire galaxy.

The quasar variability is often modelled as a damped random walk (Kelly et al., 2009; Zu et al., 2013). These variations do not show signs of periodicity and have stochastic amplitude. However, the physical mechanism that allows large amplitudes in accretion disk emission variability is still a topic of research (Dexter & Agol, 2011). Edelson & Nandra (1999) provide a list of timescales for a compact variable source. The list starts with the fastest light crossing timescale followed by orbital timescale. Other timescales specific to the accretion disk include thermal, sound crossing and viscous timescales. These timescales depend on the mass of the black hole and distance from the singularity. The theories on AGN variability include magneto-hydrodynamic instabilities, varying accretion, dust obscuration from various regions of the host galaxy and maybe even microlensing due stars (Peterson, 2001). In the following subsections, we go through our results of variability of different types, referring to Figure 3.5.

5.2.1 Variability of Types 1-1.5

Most of the AGN variability is attributed to variations in accretion rate, as the accretion disc is the most luminous part of an AGN. The AGN types 1-1.5 are assigned to AGN with higher Hβ/OIII ratio, where the Hβ emission line is an indicator of the current accretion. Therefore, we expect variability in the flux emission of types 1-1.5 and the variability threshold method does indeed classify most of the type 1-1.5 AGN as variable. However, we do not see a large difference in the overall distribution of these types in Figure 3.5. The snapshot of 6dFAGN types sample the sources at one instance in time, while the variability measure, Q_{var}, provides an upper limit of the variability amplitude over the past five years. Therefore, we speculate that AGN frequently fluctuate between the three types, but Q_{var} only measures variability of the highest accretion type, which could explain the lack of difference in the distribution of the three types.

5.2.2 The Peculiarity of Types 1.8 and 1.9

AGN with low Hβ/OIII line ratios are marked as type 1.8/1.9, but the literature has not presented a coherent picture of the role of AGN types 1.8/1.9. The lower line ratio can be due to a current low in accretion rate, or host galaxy dust extinction (eg. see Maiolino & Rieke (1995)). In this work we assume that type 1.8/1.9 AGN are weakly accreting and expect non-varying lightcurves. In Figure 3.5, we find that our variability threshold divides the population of these AGN types by roughly a half. This questions our assumption of non-variability. Type

1.8 and 1.9 could be a transition phase when changing type from 1 to 2 or vice versa. This also agrees with the speculation that type 1.2 and 1.5 are different rates of accretion of type-1 AGN.

We must also take into account that type labels used here are from the 6dFAGN catalogue, followed by a "blind decade" before the ATLAS lightcurve era. In Figure 5.2, we notice the transition phase has a timescale of few months, much shorter than the 6dFGS-ATLAS time delay. Thus, the labels of 6dFAGN type 1.8/1.9 would be largely irrelevant in the ATLAS lightcurves, if the average AGN of type 1.8/1.9 changes type in a decade.

5.2.3   Variability of Type 2 AGN and Star Forming Sources

This work is the first to compare the variability of such a large sample of type-2 AGN lightcurves with SF sources. The distribution of type-2 AGN is marginally brighter than SF sources (Figure 3.5), as AGN hosts are usually more massive than SF galaxies. The similarity in the Q_{var} distribution validates our use of SF sources as a reference for non-variable sources in our method.

We see a clear difference of variability distribution on either side of the threshold. Once again, we are not aware if these AGN have changed their types between the 6dFAGN typing and ATLAS era, and we miss any CLAGN that have changed type twice, reverting back to type-2. Moreover, the relatively large sample of type-2 AGN contain AGN labelled as type-2 due to orientation dependent obscured BLR. Hence, we would not be able to observe the type changes of these obscured AGN. However, the "true type-2" AGN where the broad lines do not exist could either be weakly accreting AGN that are more stable without changing types for more than a decade, or AGN that quickly revert to their type-2 phase after a short (few years) burst into higher accreting types.

5.3   Lightcurves and CLAGN Mechanisms

The structure of an AGN and the physical mechanisms that drive changes in accretion rates are not well constrained. The premise of using a single variability threshold to classify the types would be misguided if variations in the flux correspond variations in AGN types. All of the 6 CLAGN we find have a delay between the latest measurement in the lightcurve and WiFeS observation by at least 3 months, while fluctuations in variability could be shorter than a month. Ideally, to estimate a relation between AGN-type and variability, we would need

time-resolved spectroscopic observations of the AGN similar to the repeated observations by
Hon et al. (2022) in Figure 5.2.

To better understand the CLAGN mechanism, we can gain incremental clues from each CLAGN
that we find in the act of changing type. For example, Ricci et al. (2020) find **1ES 1927+654**,
initially marked as a type-2 AGN, start accreting $1-3$ months after a star is tidally disrupted
in the gravity field of the black hole. The X-ray luminosity of the source gradually increases
as accretion rate increases. Ricci et al. (2020) present a model wherein the TDE causes rapid
accretion of the innermost region of the accretion disk. Once material closest to the black
hole has been consumed, the accretion disk has a hole and thus loses its bright, hot parts.
Thereafter, the remaining material slowly move inwards, refilling the innermost region and
accretion ramps up again. We find a similar situation in **g1254564-265702**, **g0547318-
304146** and **g1201144-034041** (Figures 4.7 and 5.2) where the AGN show variability, followed
by a flare or TDE as the innermost material rapidly breaks off into the black hole. Unlike **1ES
1927+654** which restarts accretion in a few months, the three AGN continue without accreting
or weakly accreting for at least two years. Following the reasoning of this model, the time before
restarting accretion could depend on factors such as infall rate or black hole mass.

Merloni et al. (2015) also relate CLAGN to TDEs. They present a model where the accretion
of a large tidally disrupted star itself causes flares, similar to the ones we see in **g0547318-
304146** and **g1201144-034041**, detected in type 1-1.5 AGN lightcurves. Runnoe et al. (2016)
find a counter-example to the TDE argument as the prolonged flares before the turn-off event
is not similar to the rapid brightening of a TDE. They support the idea that turn-off changing
look events are caused by drop in accretion rate using repeated spectroscopic observations of
CLQ **J1011+5442**. In addition, Hutsemékers et al. (2017) support this varying accretion rate
argument by measuring the polarisation to provide evidence that dimming of **J1011+5442** is
not due to obscuration.

It has been established that AGN flux is correlated with accretion rate, which translates to
AGN type. For example, Kollatschny et al. (2000) present a relation where the continuum
flux of **NGC 7603** observed over 20 years is directly correlated with the intensities of Balmer
lines. Elitzur et al. (2014) also find the relation between accretion luminosity and AGN types.
They provide a model where the evolution of AGN follows types $1 \rightarrow 1.2/1.5 \rightarrow 1.8/1.9 \rightarrow 2$,
as the accretion weakens over time. The reduction in the broad emission lines is explained by
a disk-wind scenario, where clouds of material are transferred via hydro-magnetic disk winds.
As luminosity decreases, more clouds fall from high altitude trajectories (BLR), following the
motion of disk, which in turn reduces the broad emission lines. Our work agrees with this

correlation between AGN flux and spectroscopic types as seen in Figure 5.2. However, the evolution sequence of the disk-wind model does not explain turn-on CLAGN phenomena, as seen in **g1340153-045332**, where the type evolves from $1.9 \rightarrow 1.5$ in 110 days.

Conversely, Dexter et al. (2019) argue that there is no evidence that the BLR structure changes as the type changes. They hypothesise that changes in AGN types could be variations in the accretion disk itself, and the timescale can be feasible if the origin of variation is from the innermost edge of a geometrically thick disk. Such a disk would be held together by magnetic pressure, could have its scale height decoupled from thermal properties and have the same disk structure at varying accretion luminosity (Dexter & Begelman, 2019). CLAGN are then just high variation extremes of otherwise perpetually stochastic variations in AGN emission.

We make note of one similar work that was published during the time of the Honours year project. López-Navas et al. (2022) present a similar candidate selection method which involves variability classification to select turn-on CLAGN. They use lightcurves from Zwicky Transient Facility (ZTF) alert stream (Bellm et al., 2019) to obtain a sample of 22,380 type-2 sources. Variable lightcurves are identified using Automatic Learning for the Rapid Classification of Events (ALeRCE) broker lightcurve classifier (Sánchez-Sáez et al., 2021). Their method finds 30 candidates, and they observe six candidates, all of which are turn-on CLAGN.

5.4 Future Directions

The search for CLAGN is far from finished. There is much to learn about the mechanisms of AGN evolution. We identify a few avenues to continue the work presented in the thesis:

- The immediate next step is to follow up on CLAGN candidates presented in this work so as to increase the sample of known CLAGN. Monitoring known CLAGN can help constrain the timescale of AGN type changes.

- Following the limitations of the variability threshold method, a new search algorithm can be developed, such that it analyses lightcurves to identify AGN shifts from non-variable to variable or vice versa. A starting point on this endeavour would be to use multiple variability measures on different sections of the time axis of the lightcurve, and select lightcurves with larger spread in the variability measures.

- Of the 72 observed CLAGN candidates selected from the visual method, only six have been confirmed to change type. However, the remaining 66 do not show change in Balmer line

widths and intensities. The visual method is not reliable in selecting CLAGN candidates, but following our results, it can be checked if the incorrectly marked CLAGN candidates have been observed at a time at which the flux corresponds to its 6dFAGN type. This can be done by updating the ATLAS lightcurves to the present day and checking observed flux at the time of WiFeS observations.

- Our results question the reliability of the AGN type classification. The current classification scheme uses two types (1 and 2), and four sub-types (1.2, 1.5, 1.8 and 1.9) while the intensity of the Balmer lines vary on a continuous domain. Frequent spectroscopic observations of line width and accretion luminosity, similar to Kollatschny et al. (2000) but on shorter timescales, can resolve concerns on using discrete AGN typing. We can start by comparing existing repeated spectroscopic observations of sources within the literature, with updated ATLAS lightcurves or wait for future surveys of the transient sky (eg. LSST).

- To further understand the CLAGN mechanism, we can monitor all known CLAGN. This is feasible as only ~ 200 CLAGN are confirmed as of 2022. While spectroscopic or multi-band photometry is preferred, due to limited observational time, high time resolution optical lightcurves (such as ATLAS) with occasional spectroscopic typing may be sufficient.

Chapter 6

Conclusion

We present a new method to search for CLAGN using AGN lightcurves. The method exploits the differences in observed stochastic variability of AGN types. We select non-variable type 1-1.5 AGN and variable type 1.8-2 AGN as CLAGN candidates. We searched 2336 AGN and marked 258 as CLAGN candidates. We recover 15 known turn-on CLAGN within our search sample, while we fail to identify all four known turn-off CLAGN. The lightcurves of these four AGN show variability in the past, but are weakly accreting in the last two years, when the most recent spectroscopic types were observed. This is a limitation of the variability method, making it more efficient in selecting turn-on CLAGN compared to turn-off CLAGN, until we examine lightcurves for sub-epochs showing changes.

Due to available observing time before development of our variability method, we perform an expedient visual selection of CLAGN candidates. We observe 72 candidates and find six new CLAGN, three turn-on and three turn-off. All six CLAGN are once again recovered in the variability method. We find a turn-off CLAGN that changes type from $1.8 \rightarrow 1.9/2$, but is marked as a turn-on candidate. This is similar to the missed CLAGN, where the lightcurve history shows signs of variability, but the spectrum was obtained during the non-variable phase.

We analyse the lightcurves of the four missed CLAGN, and the incorrectly marked turn-off CLAGN in detail. These five lightcurves have captured the AGN during their type change, a rarity in the literature. Our results advance the argument that AGN types are linked to their luminosity, and variability in lightcurve translates to variability in AGN types. Previous work on CLAGN use time-separated spectroscopic measurements of AGN types to estimate an upper limit for the changing look event timescale, with timescales varying between a few months to a few tens of years. However, our results show fluctuations in AGN types at timescales as low as a few weeks. On this basis and arguments supported by other works in literature, we speculate

the following sequence to explain the CLAGN mechanism:

Stochastic variability: Accreting AGN show strong variability in their lightcurves. The variability could be caused by non-uniform accretion rate onto the accretion disk. This variability directly changes the broad line emissions of Balmer lines, and we assign the type labels 1-1.5 based on the Hβ/OIII line ratio. AGN without the Hβ emission line is labelled as type-2 AGN.

Disk Breaking: The lightcurves of three turn-off CLAGN we have caught in the act of changing type show a strong flare, or a tidal disruption event, before switching to a weaker accretion rate (Figures 4.7 and 5.2). We speculate that instabilities which affect the innermost region of the accretion disk (eg. TDE or magneto-hydrodynamic instabilities at the inner edge of the disk) can explosively increase the accretion into the black hole for a short time, depleting the material closest to the event horizon. We perceive these AGN with scarce accretion fuel as type-2 AGN.

Disk Refilling: As material gradually refills the accretion disk, the accretion restarts. Depending on the environment, the refilling rate dictates the strength of accretion luminosity and the time period it shows this "restarting accretion" phase. AGN in this phase are perceived as type 1.8 and 1.9. The lightcurves of two turn-on CLAGN we analyse (Figure 5.2) show this gradual increase in accretion luminosity. We have spectroscopic evidence from previous studies that show the increasing brightness phase has Balmer line widths corresponding to types 1.8 and 1.9.

To confirm our speculative model, the next step is to develop a new search algorithm that finds ATLAS lightcurves of AGN in the act of changing types. In the long run, we would need to monitor known CLAGN to constrain type-change timescales. Like most previous works on CLAGN, we emphasise the importance of time-resolved multi-band observations in understanding the transient nature of AGN. Fortunately, upcoming surveys such as the LSST are equipped with the capability of long term monitoring of the sky. Capturing the mechanism that turns black hole accretion on/off is pivotal in understanding the evolution of AGN.

Bibliography

Abramowicz M. A., Czerny B., Lasota J. P., Szuszkiewicz E., 1988, ApJ, 332, 646

Antonucci R., 1993, ARA&A, 31, 473

Balbus S. A., 2003, ARA&A, 41, 555

Balbus S. A., Hawley J. F., 1991, ApJ, 376, 214

Baldassare V. F., Geha M., Greene J., 2018, ApJ, 868, 152

Baldassare V. F., Geha M., Greene J., 2020, ApJ, 896, 10

Baldwin J. A., 1997, in Peterson B. M., Cheng F.-Z., Wilson A. S., eds, Astronomical Society of the Pacific Conference Series Vol. 113, IAU Colloq. 159: Emission Lines in Active Galaxies: New Methods and Techniques. p. 80

Baldwin J. A., Phillips M. M., Terlevich R., 1981, PASP, 93, 5

Beckmann V., Shrader C., 2012, in Proceedings of "An INTEGRAL view of the high-energy sky (the first 10 years)" - 9th INTEGRAL Workshop and celebration of the 10th anniversary of the launch (INTEGRAL 2012). 15-19 October 2012. Bibliotheque Nationale de France. p. 69 (arXiv:1302.1397)

Begelman M. C., 2002, ApJ, 568, L97

Bellm E. C., et al., 2019, PASP, 131, 018002

Bianchi S., Corral A., Panessa F., Barcons X., Matt G., Bassani L., Carrera F. J., Jiménez-Bailón E., 2008, MNRAS, 385, 195

Blandford R. D., Znajek R. L., 1977, MNRAS, 179, 433

Blandford R., Meier D., Readhead A., 2019, ARA&A, 57, 467

Collier S., Horne K., Wanders I., Peterson B. M., 1999, MNRAS, 302, L24

Czerny B., Hryniewicz K., 2011, A&A, 525, L8

Davidson K., Netzer H., 1979, Reviews of Modern Physics, 51, 715

Delgado A., Harrison D., Hodgkin S., Leeuwen M. V., Rixon G., Yoldas A., 2019, Transient Name Server Discovery Report, 2019-1031, 1

Denney K. D., et al., 2014, ApJ, 796, 134

Dexter J., Agol E., 2011, ApJ, 727, L24

Dexter J., Begelman M. C., 2019, MNRAS, 483, L17

Dexter J., et al., 2019, ApJ, 885, 44

Edelson R., Nandra K., 1999, ApJ, 514, 682

Elitzur M., 2006, New A Rev., 50, 728

Elitzur M., Ho L. C., Trump J. R., 2014, MNRAS, 438, 3340

Fabian A. C., Iwasawa K., Reynolds C. S., Young A. J., 2000, PASP, 112, 1145

Graham M. J., et al., 2020, MNRAS, 491, 4925

Green P. J., et al., 2022, ApJ, 933, 180

Groves B., 2007, in Ho L. C., Wang J. W., eds, Astronomical Society of the Pacific Conference Series Vol. 373, The Central Engine of Active Galactic Nuclei. p. 511 (arXiv:astro-ph/0612309)

Guo H., et al., 2020, ApJ, 888, 58

Hon W. J., Wolf C., Onken C., Webster R., Auchettl K., 2022, arXiv e-prints, p. arXiv:2202.04851

Hubeny I., Blaes O., Krolik J. H., Agol E., 2001, ApJ, 559, 680

Hutsemékers D., Agís González B., Sluse D., Ramos Almeida C., Acosta Pulido J. A., 2017, A&A, 604, L3

Hutsemékers D., Agís González B., Marin F., Sluse D., Ramos Almeida C., Acosta Pulido J. A., 2019, A&A, 625, A54

Jones D. H., et al., 2004, MNRAS, 355, 747

Jones D. H., et al., 2009, MNRAS, 399, 683

Kelly B. C., Bechtold J., Siemiginowska A., 2009, ApJ, 698, 895

Kollatschny W., Bischoff K., Dietrich M., 2000, A&A, 361, 901

LaMassa S. M., et al., 2015, ApJ, 800, 144

Laha S., et al., 2022, ApJ, 931, 5

Laor A., 2003, ApJ, 590, 86

Laor A., Netzer H., 1989, MNRAS, 238, 897

Lawrence A., 2018, Nature Astronomy, 2, 102

López-Navas E., et al., 2022, MNRAS, 513, L57

MacLeod C. L., et al., 2016, MNRAS, 457, 389

MacLeod C. L., et al., 2019, ApJ, 874, 8

Maiolino R., Rieke G. H., 1995, ApJ, 454, 95

Marconi A., Hunt L. K., 2003, ApJ, 589, L21

Merloni A., et al., 2015, MNRAS, 452, 69

Narayan R., Yi I., 1995, ApJ, 452, 710

Nemmen R. S., Storchi-Bergmann T., Eracleous M., Yuan F., 2009, Proceedings of the International Astronomical Union, 5, 313

Netzer H., 2015, ARA&A, 53, 365

Nicholl M., et al., 2020, MNRAS, 499, 482

Osterbrock D. E., 1981, ApJ, 249, 462

Padovani P., 2017, Frontiers in Astronomy and Space Sciences, 4, 35

Padovani P., et al., 2017, A&A Rev., 25, 2

Peterson B. M., 2001, in Aretxaga I., Kunth D., Mújica R., eds, Advanced Lectures on the Starburst-AGN. p. 3 (`arXiv:astro-ph/0109495`), doi:10.1142/9789812811318_0002

Peterson B. M., et al., 2004, ApJ, 613, 682

Ricci C., et al., 2020, ApJ, 898, L1

Runnoe J. C., et al., 2016, MNRAS, 455, 1691

Sánchez-Sáez P., et al., 2021, AJ, 161, 141

Seyfert C. K., 1943, ApJ, 97, 28

Shakura N. I., Sunyaev R. A., 1973, A&A, 500, 33

Shappee B. J., et al., 2014, ApJ, 788, 48

Suganuma M., et al., 2006, ApJ, 639, 46

Tavani M., et al., 2009, Nature, 462, 620

Temple M. J., Banerji M., Hewett P. C., Rankine A. L., Richards G. T., 2021, MNRAS, 501, 3061

Tohline J. E., Osterbrock D. E., 1976, ApJ, 210, L117

Tonry J. L., et al., 2018, PASP, 130, 064505

Tran H. D., 2001, ApJ, 554, L19

Tran H. D., 2003, ApJ, 583, 632

Uchiyama Y., et al., 2006, ApJ, 648, 910

Urry C. M., Padovani P., 1995, PASP, 107, 803

Wisotzki L., Christlieb N., Bade N., Beckmann V., Köhler T., Vanelle C., Reimers D., 2000, A&A, 358, 77

Wolf C., et al., 2018, PASA, 35, e010

Wolf C., Golding J., Hon W. J., Onken C. A., 2020, MNRAS, 499, 1005

Yang Q., et al., 2018, ApJ, 862, 109

Yang J., et al., 2020, ApJ, 897, L14

Zu Y., Kochanek C. S., Kozłowski S., Udalski A., 2013, ApJ, 765, 106

van Velzen S., Holoien T. W. S., Onori F., Hung T., Arcavi I., 2020, Space Sci. Rev., 216, 124

Appendix A

CLAGN Candidates List

This chapter lists the CLAGN candidates obtained via the variability threshold method. Observed targets and known CLAGN are removed from the candidate list, resulting in 28 turn-off and 172 turn-on CLAGN candidates.

A.1 Turn-Off CLAGN Candidates

SkyMapper Object ID	6dFGS Name	RA	Dec	mag r_{psf}	z	6dFAGN Type
13188680	g0009395-021437	2.4148	-2.2437	16.6876	0.0855	1
13148467	g0017034-044723	4.2640	-4.7897	17.7433	0.0987	1.5
11812405	g0043170-222203	10.8207	-22.3674	16.8001	0.0626	1.5
13624525	g0110090-100844	17.5375	-10.1454	16.8724	0.0582	1.5
12615929	g0121499-135810	20.4580	-13.9695	16.1645	0.0540	1.5
14423812	g0203490-124717	30.9543	-12.7879	16.6327	0.0526	1.2
20694896	g0305346-113454	46.3943	-11.5817	16.9444	0.0792	1.5
17326756	g0344253-392702	56.1056	-39.4504	17.7239	0.4576	1
22116718	g0351076-052637	57.7817	-5.4436	16.6924	0.0678	1.2
18032661	g0404433-295323	61.1802	-29.8898	17.2684	0.0601	1.5
22578181	g0444039-222446	71.0163	-22.4128	16.8747	0.0754	1.5
25156608	g0447390-040330	71.9124	-4.0583	15.7573	0.0815	1
23732994	g0515180-160636	78.8250	-16.1100	16.9737	0.0798	1
29060593	g0645395-402129	101.4145	-40.3580	16.8712	0.0352	1.5
86272917	g1053410-291824	163.4208	-29.3066	16.9641	0.0581	1.5
97603824	g1208503-312650	182.2096	-31.4472	17.5231	0.0466	1.5

Table A.1 continued from previous page

SkyMapper Object ID	6dFGS Name	RA	Dec	mag r$_{psf}$	z	6dFAGN Type
98616917	g1342426-335945	205.6776	-33.9959	15.7851	0.0188	1.5
108762361	g1357332-125418	209.3883	-12.9051	16.9447	0.0582	1.2
195610497	g1724226-131446	261.0942	-13.2461	17.1457	0.0921	1.2
487289545	g2027244-411548	306.8515	-41.2632	16.4641	0.0651	1.5
234143384	g2039272-301852	309.8633	-30.3145	15.8308	0.0791	1.2
487995745	g2049332-390204	312.3882	-39.0344	16.5890	0.0413	1.5
3971217	g2147133-120126	326.8053	-12.0238	16.3999	0.0485	1.2
474671	g2205311-373711	331.3795	-37.6198	17.4002	0.0565	1
5158233	g2209558-101449	332.4825	-10.2468	18.0779	0.0833	1.5
1743013	g2238225-353348	339.5939	-35.5632	16.4887	0.0626	1.2
7624194	g2251234-045304	342.8475	-4.8845	17.4076	0.0934	1.2
8118827	g2358169-123311	359.5702	-12.5530	18.0776	1.4286	1

Table A.1: Turn-off CLAGN candidate list.

A.2 Turn-On CLAGN Candidates

SkyMapper Object ID	6dFGS Name	RA	Dec	mag r$_{psf}$	z	6dFAGN Type
13091533	g0010200-061706	2.5832	-6.2849	16.5602	0.0820	1.9
13357160	g0024191-013818	6.0795	-1.6383	16.7091	0.0377	1.9
12953671	g0033169-114121	8.3203	-11.6891	17.0997	0.0263	2
13462045	g0039200-020815	9.8335	-2.1374	16.4107	0.0472	2
13037273	g0040528-074209	10.2200	-7.7024	15.7299	0.0551	1.9
12180811	g0051176-144751	12.8235	-14.7975	17.0506	0.0909	1.9
13004046	g0051258-102645	12.8573	-10.4457	16.9153	0.0550	1.9
13540422	g0053426-010507	13.4277	-1.0851	16.3226	0.0466	2
11743239	g0053544-240437	13.4768	-24.0770	16.7209	0.0565	2
8944455	g0053576-413936	13.4901	-41.6599	16.7700	0.0776	1.9
13420357	g0056006-061418	14.0024	-6.2382	18.3047	0.0193	2
13872465	g0101244-030840	15.3517	-3.1445	16.5686	0.0701	1.9
9146240	g0112363-414241	18.1513	-41.7114	16.1648	0.0335	2
12601354	g0113499-145057	18.4577	-14.8492	17.0123	0.0545	2

Table A.2 continued from previous page

SkyMapper Object ID	6dFGS Name	RA	Dec	mag r_{psf}	z	6dFAGN Type
12323787	g0117112-220904	19.2967	-22.1510	16.9020	0.0895	1.9
13933659	g0117394-025627	19.4143	-2.9409	16.3631	0.0512	2
10038025	g0118256-321712	19.6067	-32.2868	17.1495	0.0764	2
14082548	g0144586-023159	26.2440	-2.5331	16.5552	0.0958	2
14125805	g0149521-222534	27.4671	-22.4260	16.1528	0.0449	2
10529056	g0157106-365123	29.2943	-36.8563	17.0638	0.0552	2
14916845	g0204368-115943	31.1532	-11.9954	16.5447	0.0727	1.9
14500904	g0209537-135321	32.4739	-13.8891	16.7839	0.0726	1.9
10976335	g0218352-305015	34.6467	-30.8376	17.5768	0.0993	2
14610149	g0229289-185554	37.3703	-18.9315	16.1383	0.0924	1.9
15598455	g0240237-024342	40.0989	-2.7283	16.4969	0.0289	2
15638721	g0245455-030450	41.4394	-3.0804	16.9229	0.0747	1.9
14658186	g0247346-201100	41.8940	-20.1834	16.5242	0.0441	1.9
505112536	g0252103-393611	43.0430	-39.6030	16.7685	0.0893	1.9
14681621	g0259401-184736	44.9172	-18.7934	17.1020	0.0697	1.9
21588790	g0304197-021821	46.0822	-2.3060	15.7983	0.0287	2
17741731	g0308528-231311	47.2199	-23.2197	16.9617	0.0777	2
21381829	g0310185-083056	47.5771	-8.5156	16.2534	0.0320	2
21382261	g0311008-082529	47.7533	-8.4246	15.6793	0.0360	2
21499742	g0317067-063008	49.2778	-6.5022	15.7480	0.0133	2
21692504	g0317498-003317	49.4574	-0.5546	16.2803	0.0210	2
17832134	g0321104-212929	50.2933	-21.4914	17.2168	0.0719	1.9
504759777	g0333597-420947	53.4989	-42.1629	16.8388	0.0495	2
17872693	g0343265-314438	55.8605	-31.7439	16.5526	0.0324	2
22005561	g0353010-062327	58.2542	-6.3908	17.0090	0.0762	1.9
22201714	g0358201-053207	59.5837	-5.5352	15.9284	0.0623	1.8
18019672	g0403174-304810	60.8223	-30.8028	17.0956	0.0604	2
17533677	g0409334-372407	62.3890	-37.4019	17.3911	0.0589	1.9
19360507	g0414170-290833	63.5709	-29.1424	17.1912	0.0888	2
24905969	g0418562-023322	64.7343	-2.5561	16.0807	0.0173	1.9
22367469	g0423401-240639	65.9170	-24.1108	17.0070	0.0597	2
24963611	g0428196-015442	67.0815	-1.9116	16.9535	0.0763	1.9
18439522	g0430108-364206	67.5449	-36.7018	17.1060	0.0766	1.9
19242182	g0432173-302358	68.0722	-30.3994	15.9392	0.0549	1.9
19189384	g0432381-332450	68.1586	-33.4138	15.7965	0.0327	1.9

Table A.2 continued from previous page

SkyMapper Object ID	6dFGS Name	RA	Dec	mag r_{psf}	z	6dFAGN Type
18460747	g0435577-355858	68.9905	-35.9827	16.3409	0.0603	1.9
24631101	g0439440-090322	69.9333	-9.0561	16.2682	0.0523	1.9
18479272	g0440459-372906	70.1911	-37.4849	16.3800	0.0401	2
18479921	g0440596-373411	70.2482	-37.5696	16.5994	0.0409	2
25184213	g0457593-061232	74.4971	-6.2089	17.3149	0.0100	2
24764794	g0458126-074649	74.5523	-7.7804	16.0968	0.0132	2
23600940	g0514572-192535	78.7383	-19.4263	17.0023	0.0895	2
18903230	g0517083-371022	79.2845	-37.1727	16.9001	0.0420	2
23289019	g0520582-213520	80.2423	-21.5889	17.3002	0.0836	2
20283783	g0529378-285934	82.4075	-28.9927	16.1483	0.0589	2
19795813	g0529592-340159	82.4967	-34.0329	16.2104	0.0790	2
26891882	g0530482-044044	82.7008	-4.6790	18.3217	0.0658	1.9
19034686	g0541169-382009	85.3203	-38.3359	16.4477	0.0357	2
20050703	g0546563-333742	86.7346	-33.6282	15.9341	0.0349	1.9
24190446	g0553013-163238	88.2556	-16.5438	18.0776	0.1001	2
28334447	g0604151-412707	91.0630	-41.4520	16.6690	0.0413	2
28386705	g0618343-413916	94.6429	-41.6545	16.7175	0.0825	2
28784931	g0622472-402857	95.6968	-40.4826	16.3579	0.0770	2
28975155	g0626586-370559	96.7442	-37.0996	16.6664	0.0386	1.9
29172035	g0629125-373922	97.3021	-37.6562	17.1793	0.0600	2
33069556	g0629315-282007	97.3813	-28.3354	16.7097	0.0420	2
30622993	g0701211-380415	105.3379	-38.0709	16.7269	0.0269	2
74728132	g0757358-013307	119.3991	-1.5519	16.6534	0.0531	2
73579585	g0807108-071723	121.7950	-7.2897	17.0079	0.0526	2
73661627	g0814187-104101	123.5778	-10.6835	16.9927	0.0693	1.8
75828917	g0827341-021247	126.8923	-2.2130	16.0466	0.0394	1.9
75719808	g0828082-050633	127.0343	-5.1091	17.4148	0.0808	2
75423692	g0828376-075020	127.1567	-7.8389	16.3218	0.0416	2
75903696	g0836389-013154	129.1623	-1.5317	15.9147	0.0309	2
75378764	g0843268-095121	130.8616	-9.8557	17.1680	0.0409	1.9
47944802	g0845371-204753	131.4047	-20.7981	16.6977	0.0230	2
47288038	g0856256-244631	134.1068	-24.7752	16.1675	0.0325	2
89227181	g0910208-053058	137.5865	-5.5162	16.5672	0.0560	1.9
89513842	g0915489-042744	138.9536	-4.4622	16.7657	0.0396	2
89572623	g0917289-020452	139.3704	-2.0812	16.8112	0.0536	2

Table A.2 continued from previous page

SkyMapper Object ID	6dFGS Name	RA	Dec	mag r$_{psf}$	z	6dFAGN Type
89683342	g0938322-091803	144.6343	-9.3009	17.6594	0.0944	2
89684561	g0938348-084759	144.6450	-8.7998	16.6706	0.0546	2
88870206	g0939427-120819	144.9280	-12.1386	17.3527	0.0483	2
89693870	g0942400-101937	145.6668	-10.3270	16.1462	0.0185	2
90045293	g0943345-050057	145.8938	-5.0158	15.6814	0.0211	2
90160148	g0944462-004119	146.1924	-0.6885	18.3807	0.0043	2
90162001	g0945119-000712	146.2998	-0.1200	17.0282	0.0305	2
88819184	g0948279-162149	147.1163	-16.3637	17.5896	0.0902	2
88695733	g1001090-192630	150.2875	-19.4415	17.2964	0.0117	1.8
90290354	g1002013-021547	150.5056	-2.2631	18.0544	0.0129	2
89982719	g1007419-070654	151.9246	-7.1150	16.4022	0.0246	2
90347285	g1007575-013617	151.9894	-1.6046	17.4505	0.0426	2
89063991	g1008029-145906	152.0120	-14.9851	16.6201	0.0576	1.8
88998974	g1010428-160834	152.6784	-16.1428	17.0671	0.0945	2
92133502	g1025502-112629	156.4591	-11.4414	16.1822	0.0398	2
82606089	g1027405-394133	156.9189	-39.6926	17.8388	0.0896	2
92304618	g1033555-080228	158.4814	-8.0412	17.6144	0.0643	2
91039288	g1035274-140748	158.8640	-14.1299	15.9184	0.0153	2
86368121	g1041173-260958	160.3223	-26.1662	17.0330	0.0148	2
83717089	g1043029-362145	160.7623	-36.3624	15.9670	0.0100	2
92852286	g1100454-063443	165.1891	-6.5785	15.8103	0.0306	2
87034752	g1107264-302906	166.8599	-30.4849	16.5547	0.0707	1.9
91500543	g1118128-205640	169.5534	-20.9443	16.5682	0.0479	2
93737166	g1119593-024722	169.9969	-2.7895	16.3414	0.0257	2
93740278	g1122554-025656	170.7308	-2.9488	16.2941	0.0465	2
93121017	g1130326-133305	172.6360	-13.5513	18.5412	0.0167	2
93831567	g1132201-050513	173.0837	-5.0869	16.5011	0.0639	2
86793647	g1135044-343612	173.7685	-34.6032	16.7909	0.0316	2
86793159	g1137189-344750	174.3288	-34.7971	17.7866	0.0209	2
85028127	g1137199-380551	174.3328	-38.0976	19.0608	0.0100	2
93814951	g1137209-053607	174.3372	-5.6019	16.2622	0.0379	2
91968305	g1140422-174010	175.1759	-17.6694	16.4272	0.0219	2
91537836	g1142593-251801	175.7473	-25.3002	17.8305	0.0964	2
93862057	g1144288-033415	176.1200	-3.5709	16.3162	0.0490	2
93365344	g1145445-114736	176.4355	-11.7934	16.1242	0.0181	2

Table A.2 continued from previous page

SkyMapper Object ID	6dFGS Name	RA	Dec	mag r_{psf}	z	6dFAGN Type
91554444	g1148019-262558	177.0078	-26.4328	17.1958	0.0625	2
91682989	g1149348-212330	177.3948	-21.3915	16.2453	0.0271	1.9
93513346	g1151356-081913	177.8985	-8.3203	16.7737	0.0756	2
87640270	g1157172-280414	179.3216	-28.0704	16.1371	0.0407	2
103759263	g1203046-243258	180.7690	-24.5495	16.6193	0.0718	2
97626661	g1203287-303000	180.8696	-30.5000	16.6784	0.0664	2
103882553	g1205249-212357	181.3538	-21.3992	16.3475	0.0320	2
106791639	g1218267-000750	184.6113	-0.1306	16.9309	0.0503	2
94390438	g1223434-423532	185.9306	-42.5921	17.9935	0.0267	2
104322606	g1224306-172400	186.1276	-17.4001	16.3701	0.0265	2
97447614	g1229419-315410	187.4247	-31.9028	17.0763	0.0543	1.9
95390047	g1243078-370552	190.7826	-37.0976	17.5181	0.0734	2
104204344	g1247401-203003	191.9169	-20.5007	17.0517	0.0471	2
107242069	g1305301-093748	196.3753	-9.6300	16.7783	0.0450	2
107322162	g1310171-072716	197.5713	-7.4543	15.6282	0.0229	2
98304106	g1311034-340028	197.7643	-34.0077	16.0045	0.0503	2
107818403	g1321353-001306	200.3973	-0.2183	16.5293	0.0822	1.8
105140957	g1337500-235941	204.4581	-23.9948	15.7654	0.0302	2
105167274	g1345017-232341	206.2572	-23.3948	17.2450	0.0971	2
105889489	g1345158-134852	206.3159	-13.8145	16.9673	0.0579	2
102204815	g1420542-280106	215.2257	-28.0183	18.9234	0.0228	2
166647551	g1511595-152614	227.9980	-15.4372	17.0761	0.0890	1.9
167254755	g1548163-175935	237.0680	-17.9931	17.5174	0.0893	2
193892717	g1620217-044341	245.0903	-4.7280	17.0567	0.0725	1.9
194063125	g1631374-033126	247.9060	-3.5238	17.4660	0.0577	2
192295981	g1633412-130039	248.4218	-13.0109	18.1617	0.0487	2
193235745	g1653546-102300	253.4776	-10.3834	17.7089	0.0600	2
259395143	g1930100-223921	292.5416	-22.6557	16.0774	0.0473	1.9
303975787	g2040111-013709	310.0462	-1.6192	15.7348	0.0304	2
298260629	g2051395-175306	312.9146	-17.8849	18.0722	0.0877	2
488173638	g2107400-394124	316.9168	-39.6901	16.2470	0.0505	2
250581	g2107599-295009	316.9997	-29.8358	15.4340	0.0198	2
5035485	g2143549-090811	325.9787	-9.1364	16.4387	0.0554	1.9
3799344	g2155318-205133	328.8827	-20.8591	16.0544	0.0669	1.9
1449694	g2157170-263059	329.3207	-26.5165	16.4166	0.0341	2

Table A.2 continued from previous page

SkyMapper Object ID	6dFGS Name	RA	Dec	mag r_{psf}	z	6dFAGN Type
5581418	g2157531-023924	329.4712	-2.6567	15.5934	0.0552	2
5490536	g2202067-053946	330.5280	-5.6626	16.0581	0.0271	1.9
5553330	g2202590-031812	330.7460	-3.3033	16.3467	0.0445	1.9
489997077	g2218575-432510	334.7397	-43.4196	16.7897	0.0739	1.9
7468691	g2224353-001104	336.1470	-0.1843	16.3148	0.0591	1.9
1659730	g2233176-371911	338.3232	-37.3197	16.2292	0.0441	1.9
2032037	g2236450-335116	339.1874	-33.8544	15.5797	0.0289	1.9
7160335	g2242278-083105	340.6160	-8.5181	17.3469	0.0832	2
2245228	g2253587-330014	343.4945	-33.0038	16.1382	0.0562	2
7608050	g2257312-061443	344.3800	-6.2451	17.4531	0.0902	1.9
7738739	g2258019-021945	344.5080	-2.3291	16.5881	0.0800	1.9
2895741	g2311271-295923	347.8630	-29.9896	16.3565	0.0291	2
8033344	g2330048-071013	352.5199	-7.1703	17.0952	0.0890	1.9
3045668	g2338165-312255	354.5687	-31.3818	16.9182	0.0845	1.9
1909982	g2342053-391259	355.5221	-39.2163	16.4162	0.0428	1.9
6767211	g2347585-151242	356.9937	-15.2117	16.9645	0.0835	2
3099481	g2356326-310124	359.1357	-31.0234	16.5366	0.0616	2
8269479	g2357057-081352	359.2736	-8.2312	16.8235	0.0880	1.9

Table A.2: Turn-on CLAGN candidate list.

Appendix B
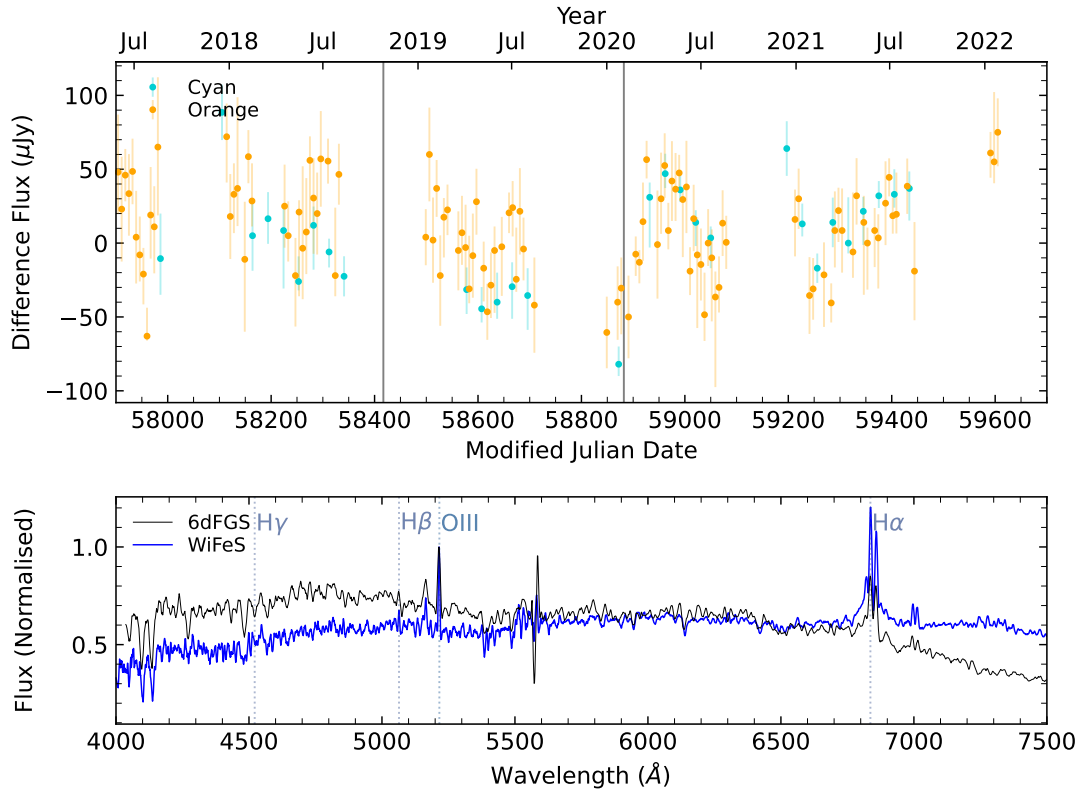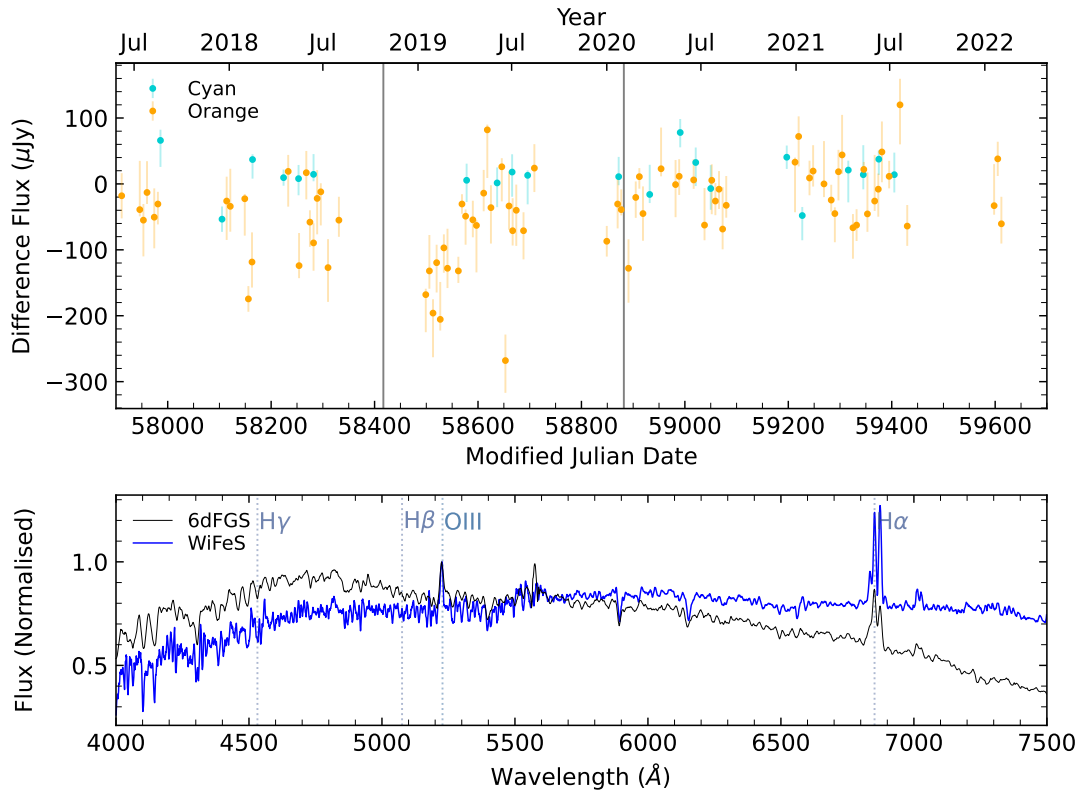
Gallery of WiFeS Spectra
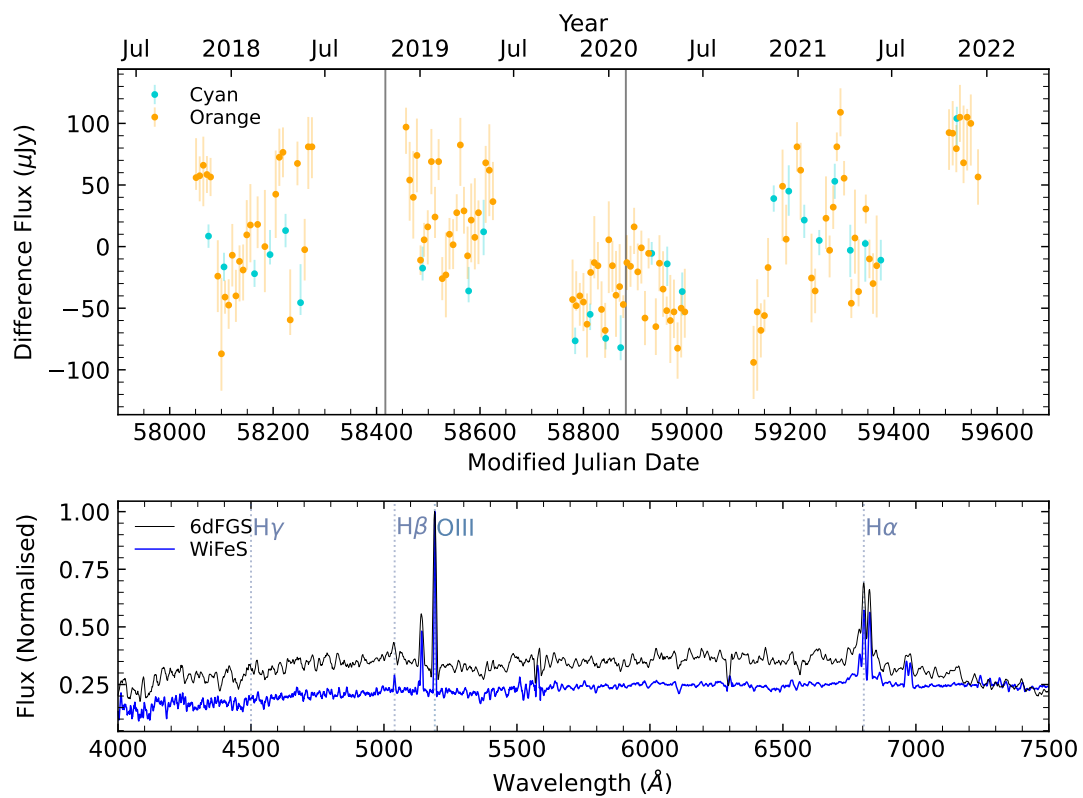
ATLAS lightcurve (top) and 6dFGS+WiFeS spectra (bottom) for **g0916467-242042** with **6dFAGN type-1.9**.
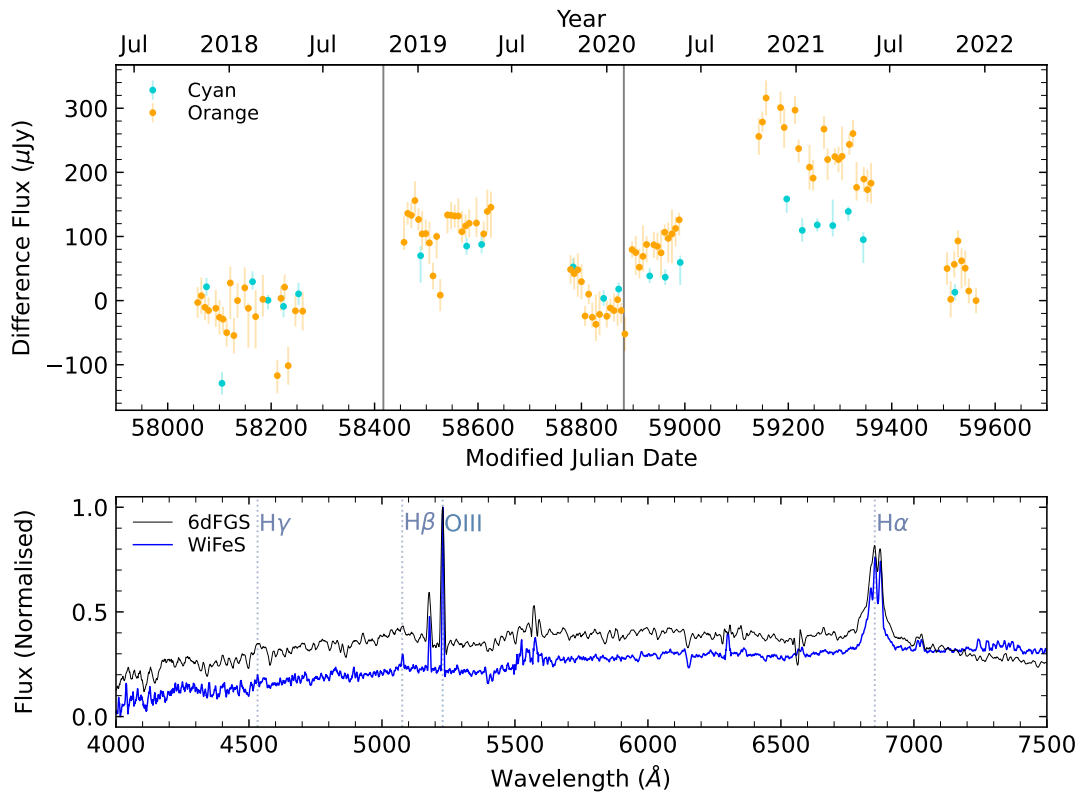
ATLAS lightcurve (top) and 6dFGS+WiFeS spectra (bottom) for **g0922229-340343** with **6dFAGN type-1.9**.
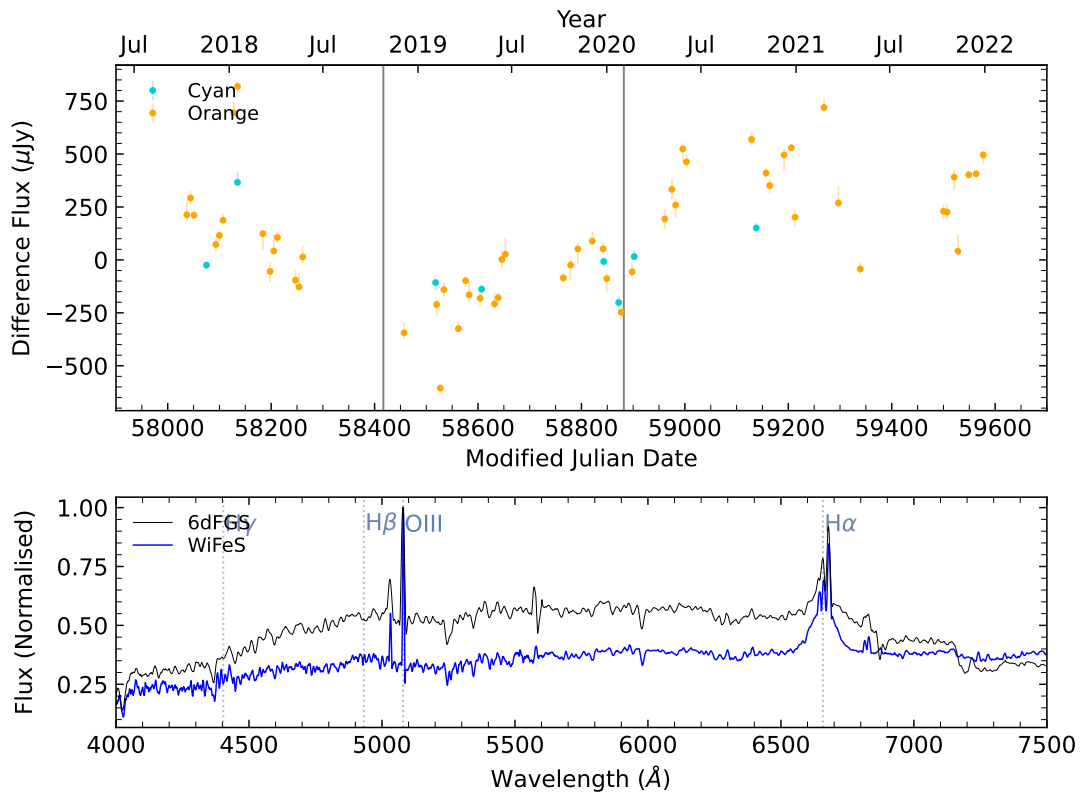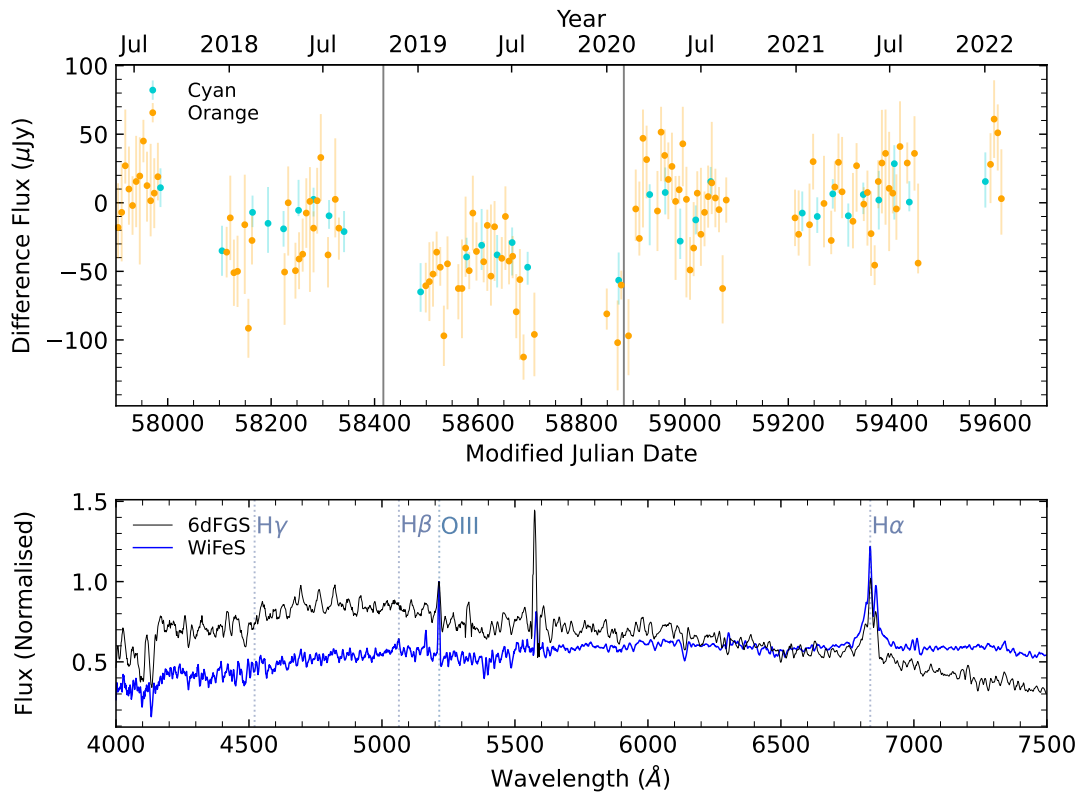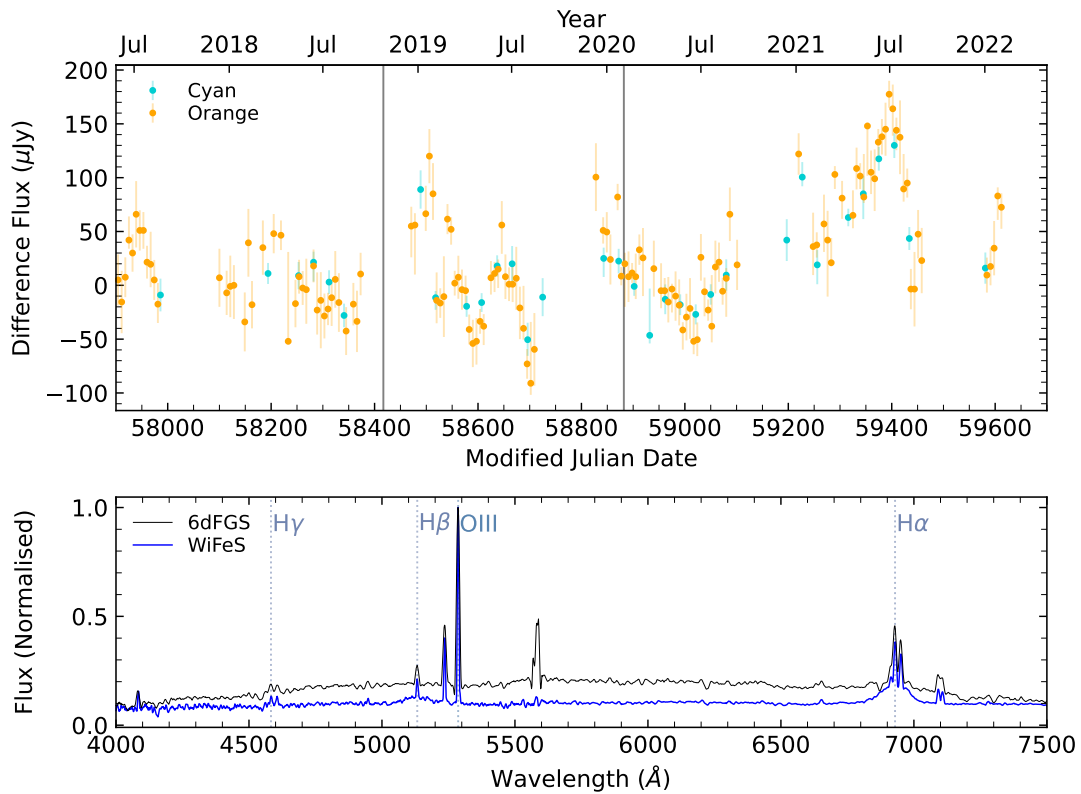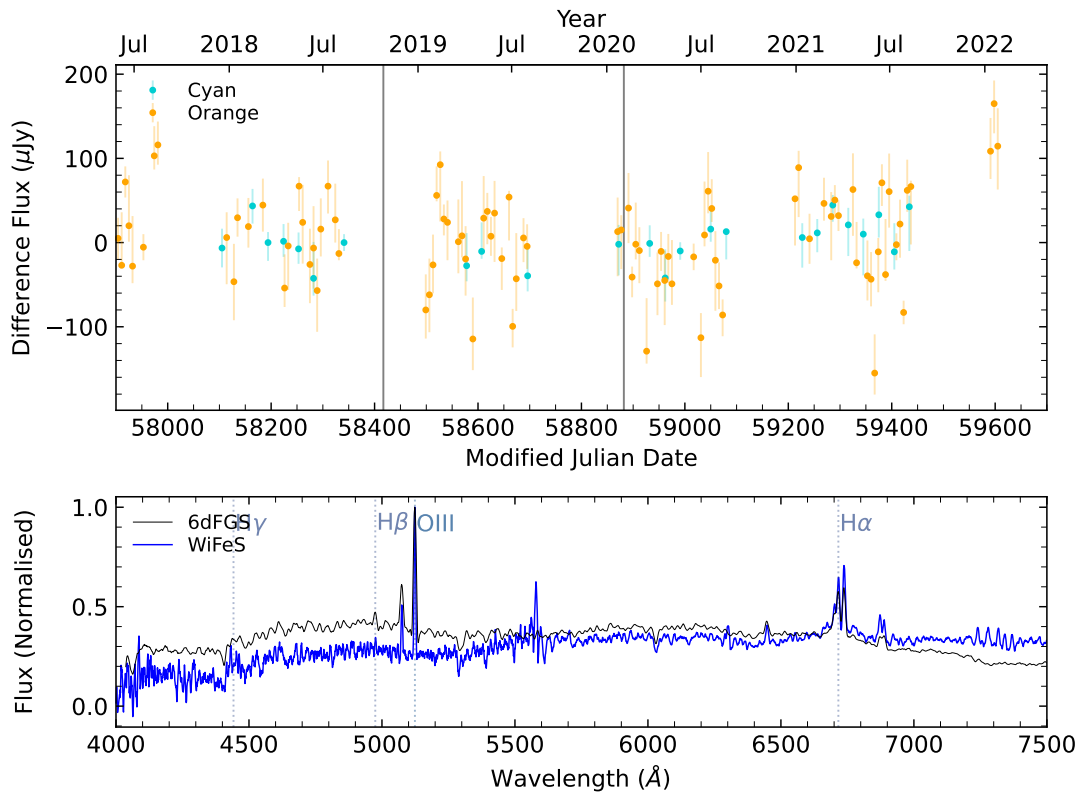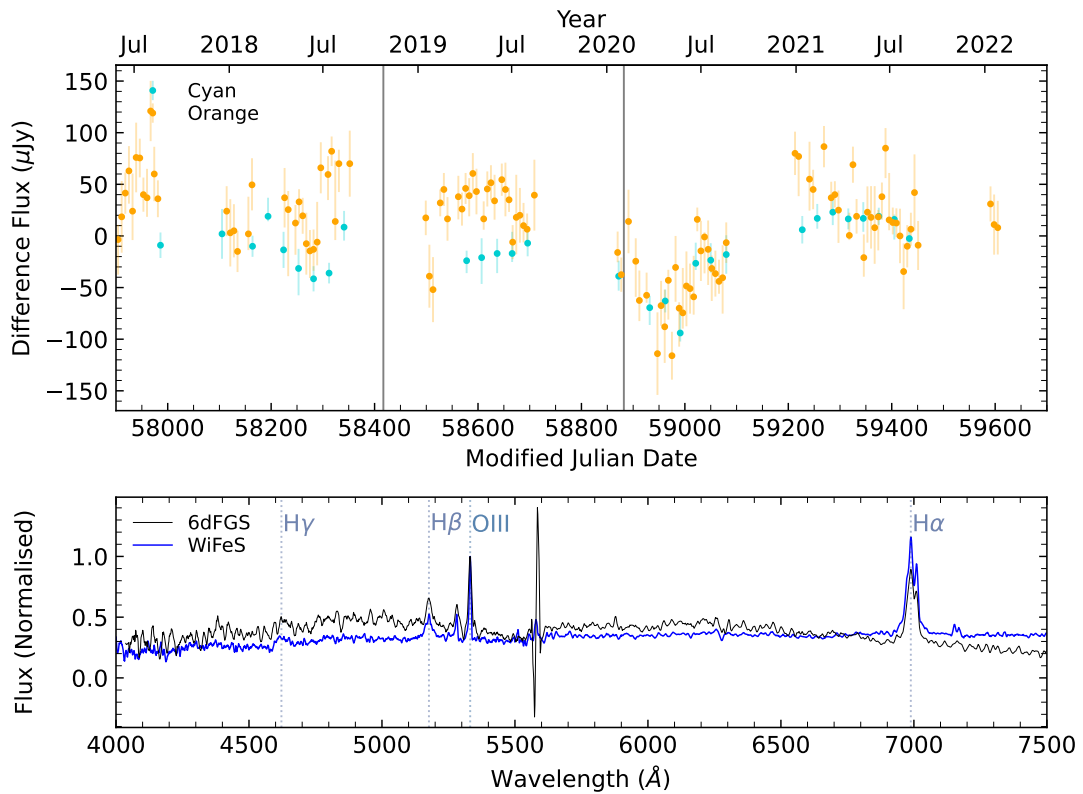

ATLAS lightcurve (top) and 6dFGS+WiFeS spectra (bottom) for **g0951550-064923** with **6dFAGN type-1.9**.
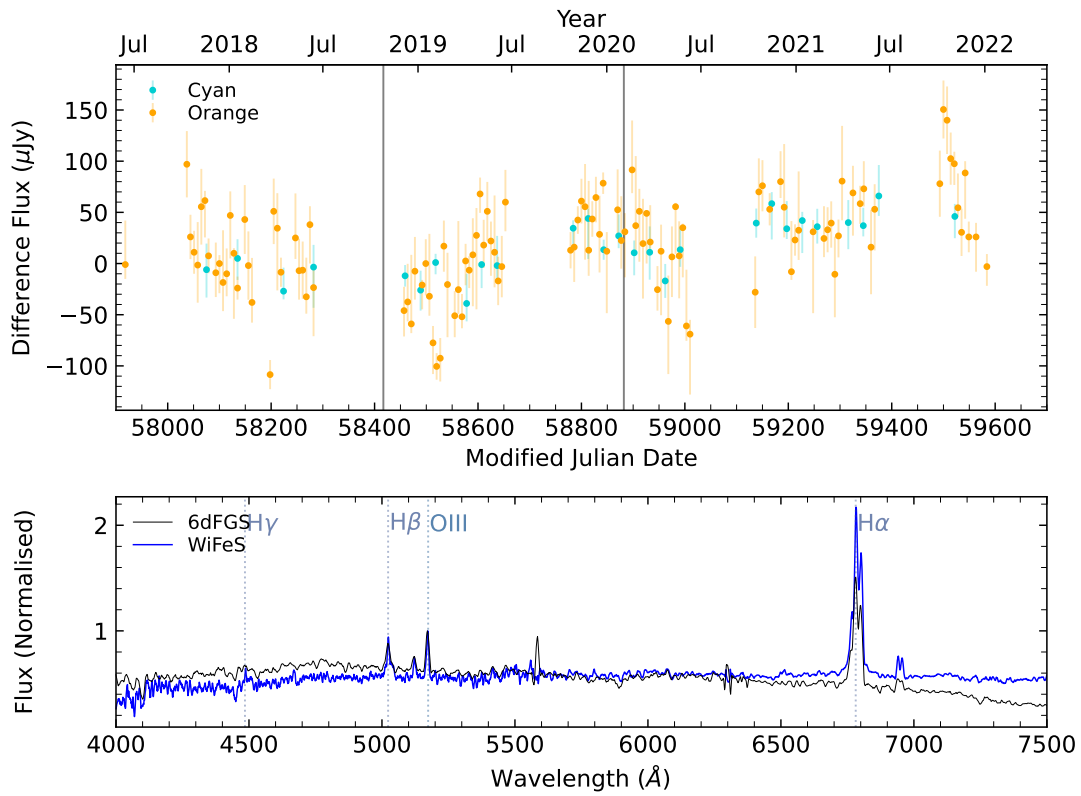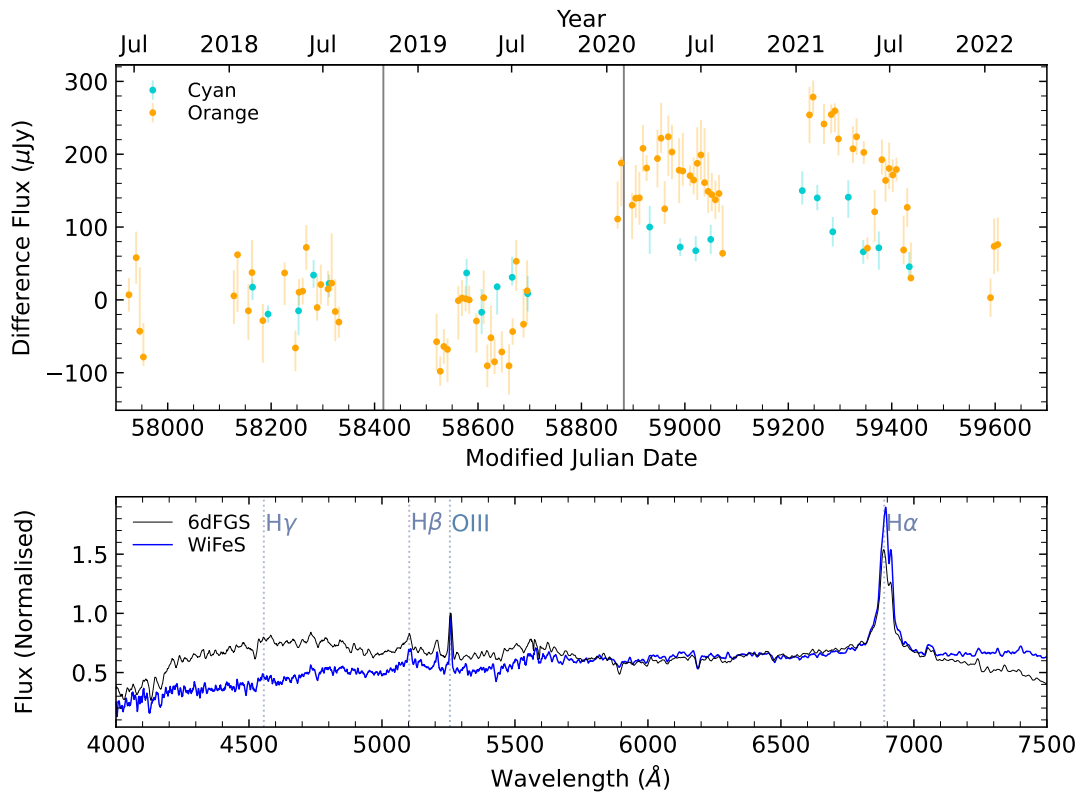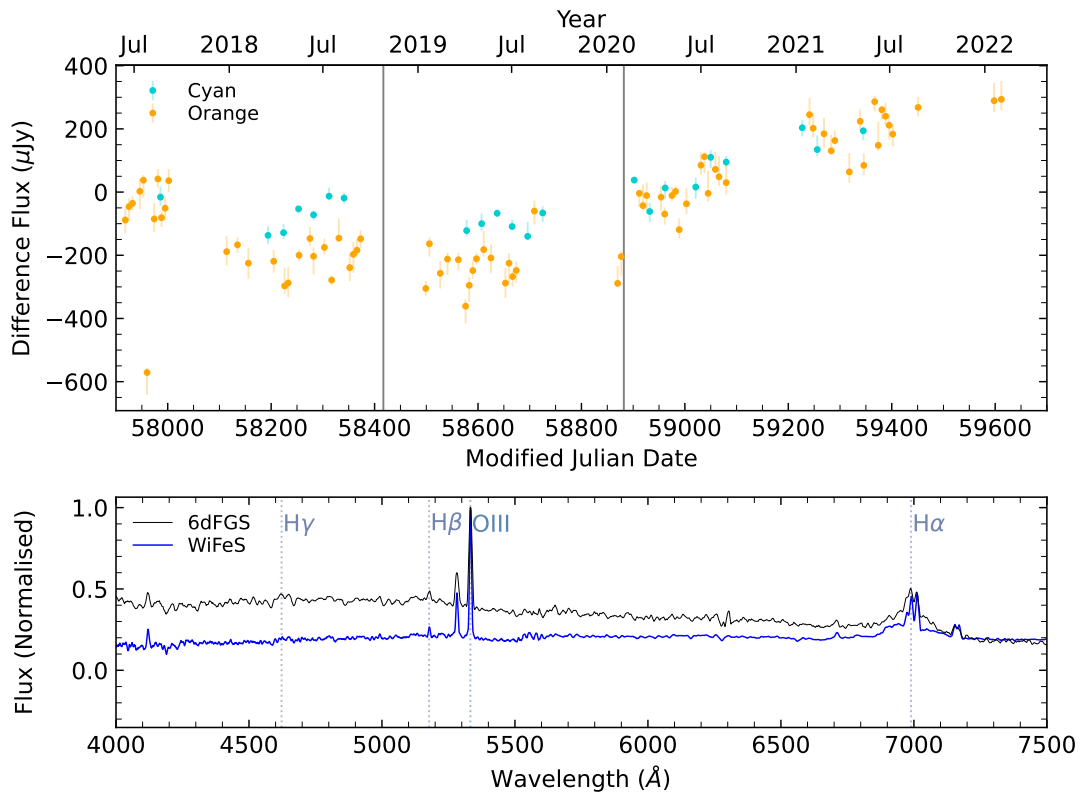
ATLAS lightcurve (top) and 6dFGS+WiFeS spectra (bottom) for **g1001422-103331** with **6dFAGN type-2**.
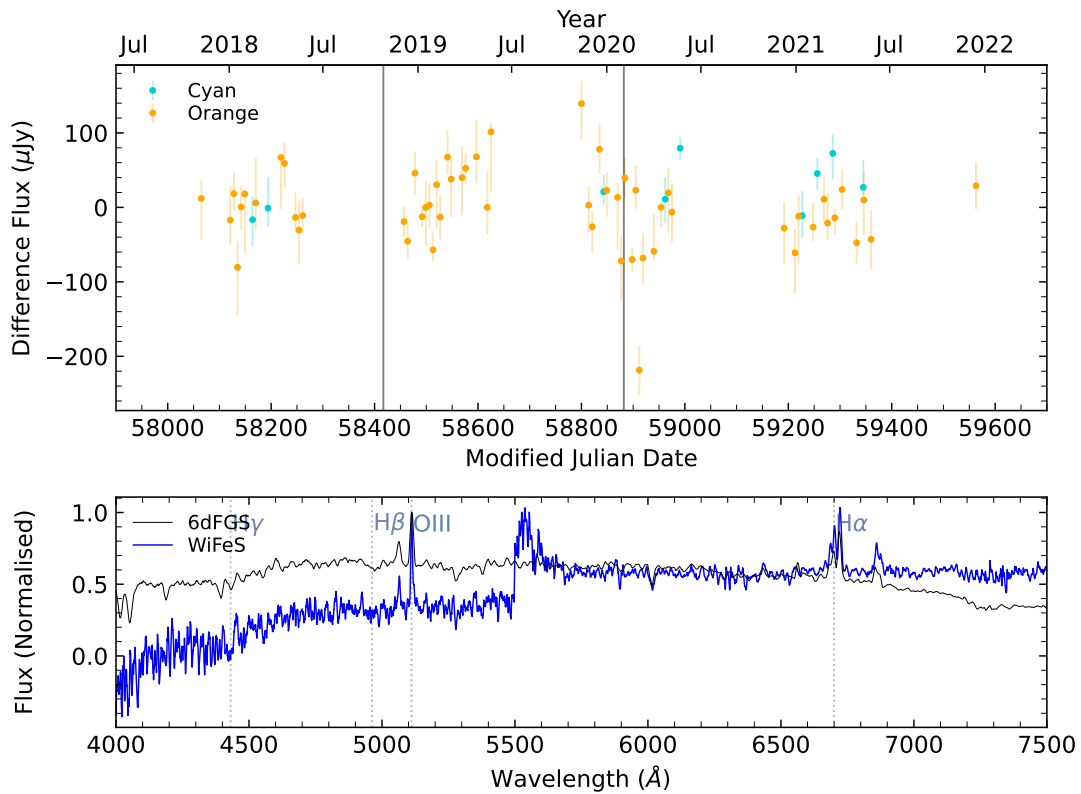
ATLAS lightcurve (top) and 6dFGS+WiFeS spectra (bottom) for **g1007009-430328** with **6dFAGN type-2**.
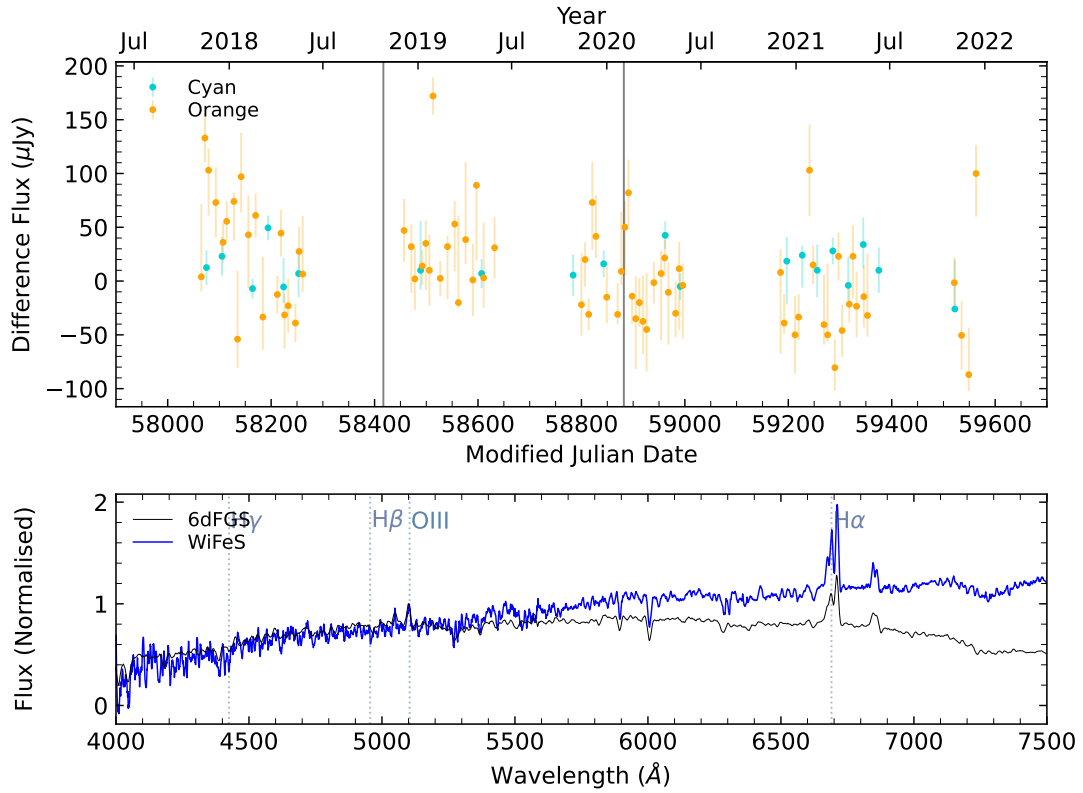
ATLAS lightcurve (top) and 6dFGS+WiFeS spectra (bottom) for **g1007450-411954** with **6dFAGN type-2**.
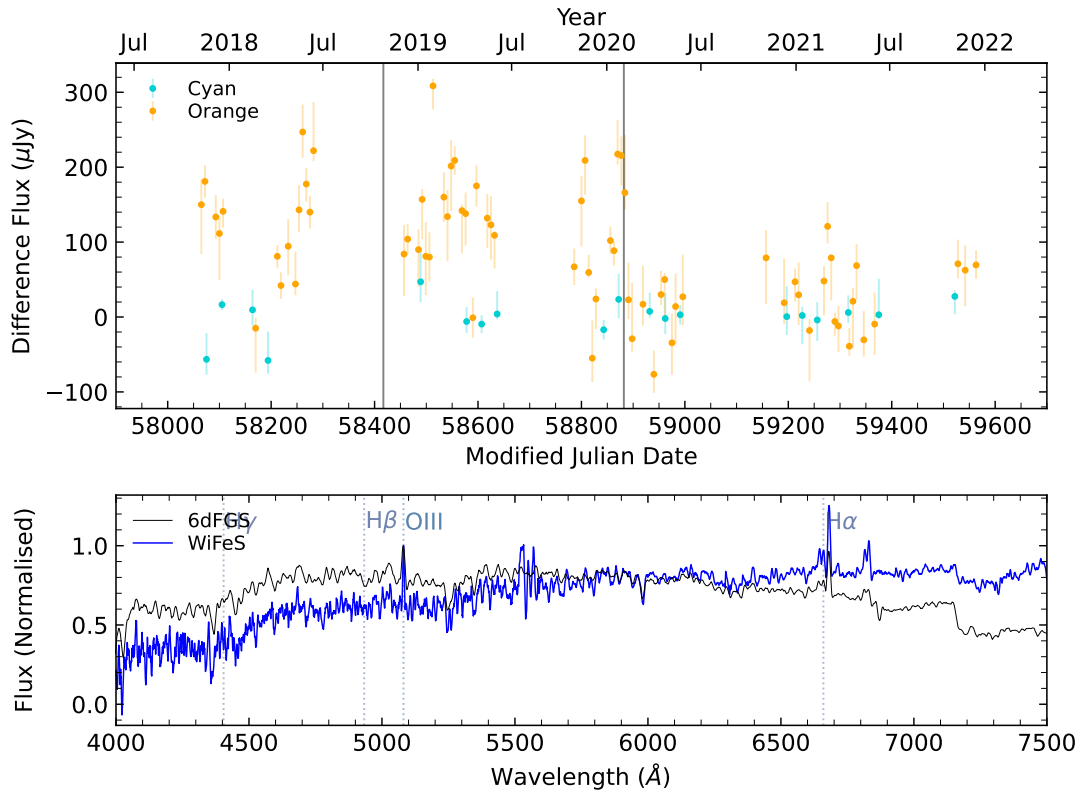
ATLAS lightcurve (top) and 6dFGS+WiFeS spectra (bottom) for **g1007550-351347** with **6dFAGN type-2**.
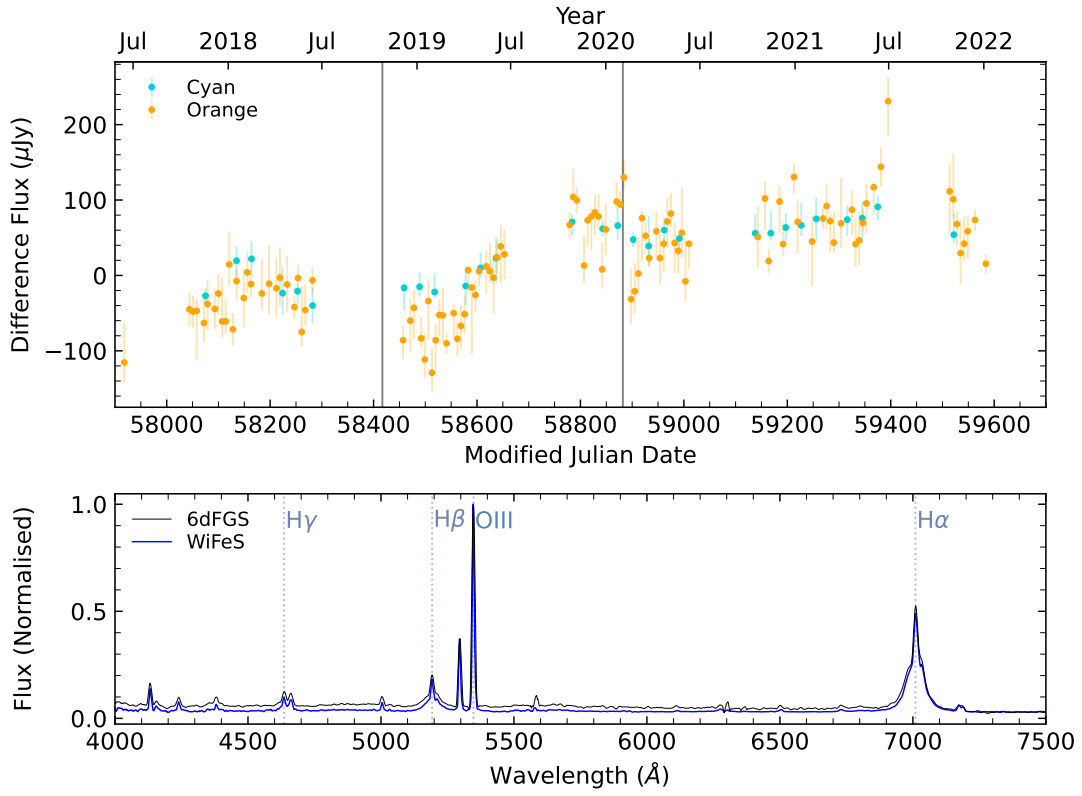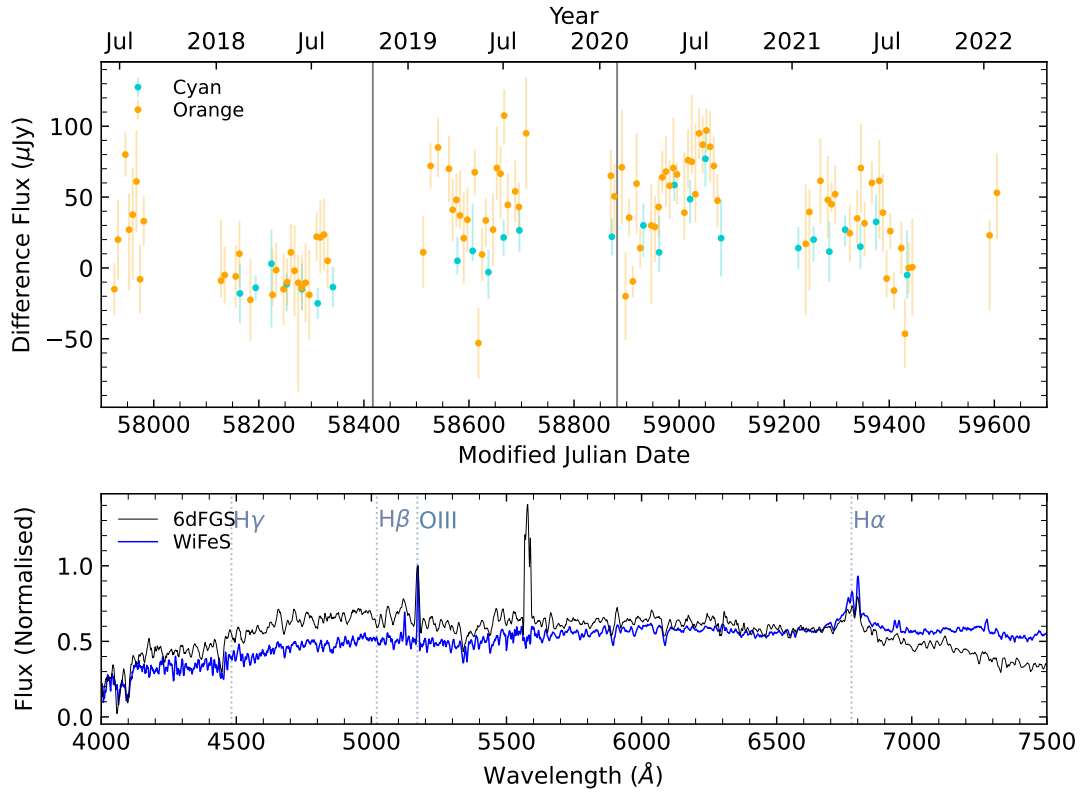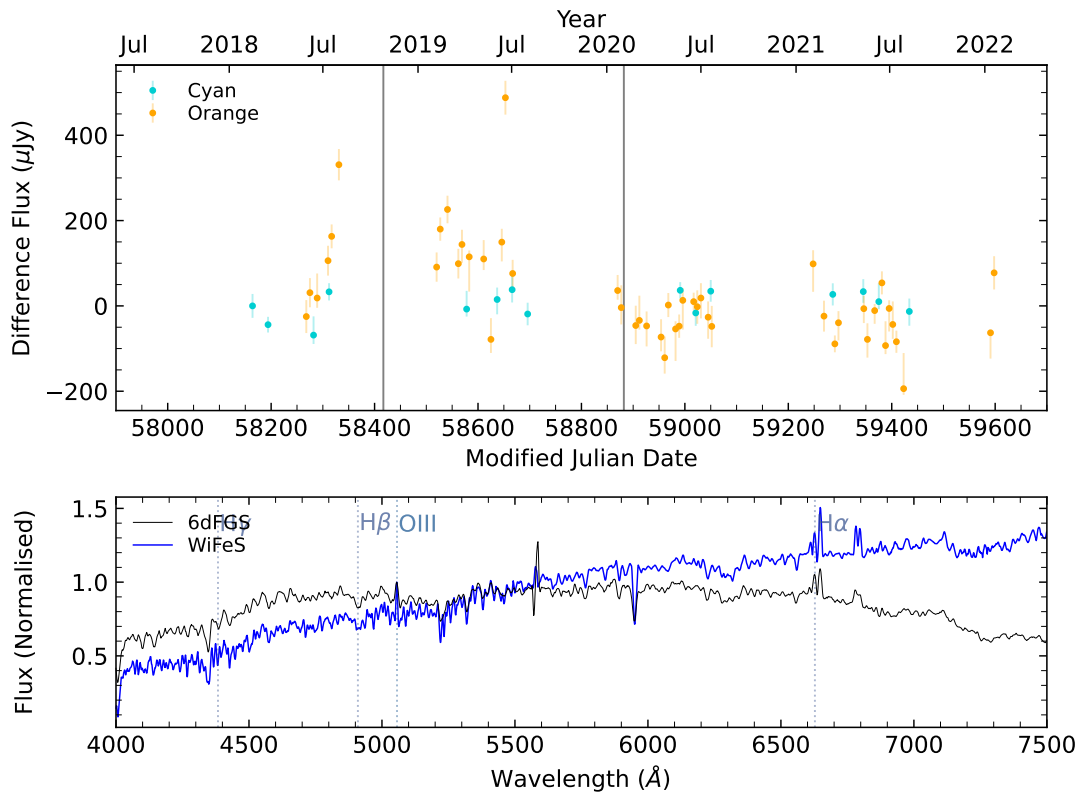
ATLAS lightcurve (top) and 6dFGS+WiFeS spectra (bottom) for **g1014116-124043** with **6dFAGN type-1.8**.
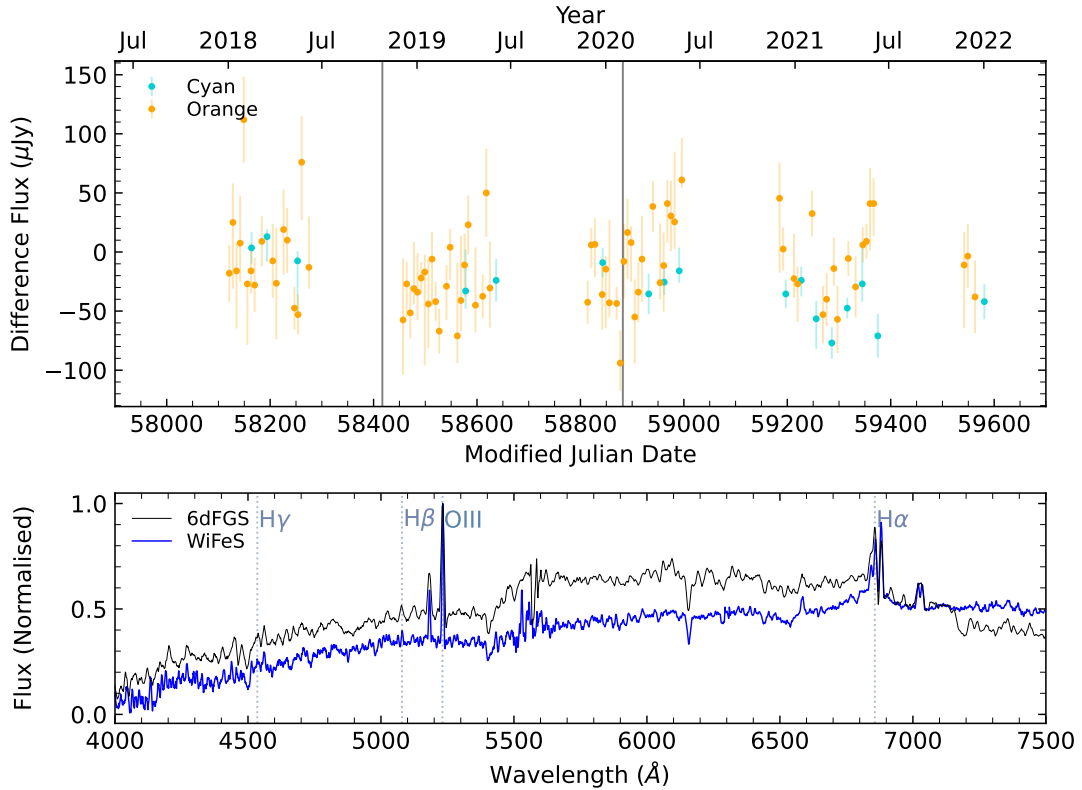
ATLAS lightcurve (top) and 6dFGS+WiFeS spectra (bottom) for **g1049464-434050** with **6dFAGN type-2**.
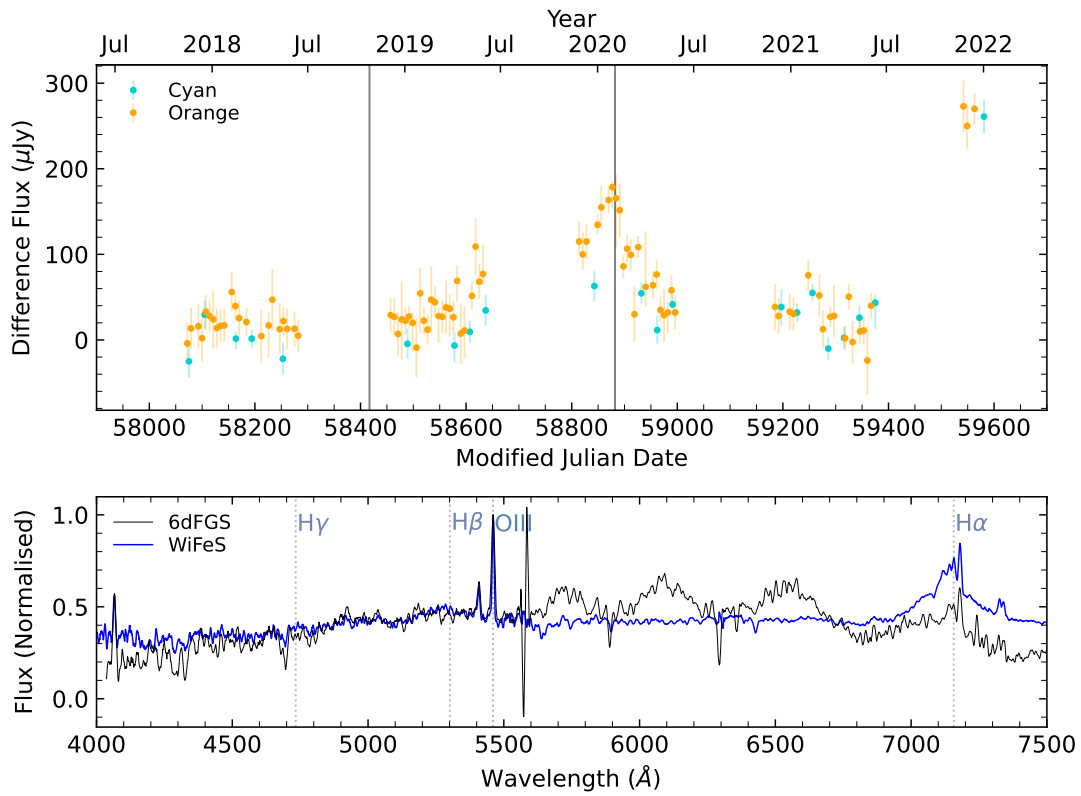
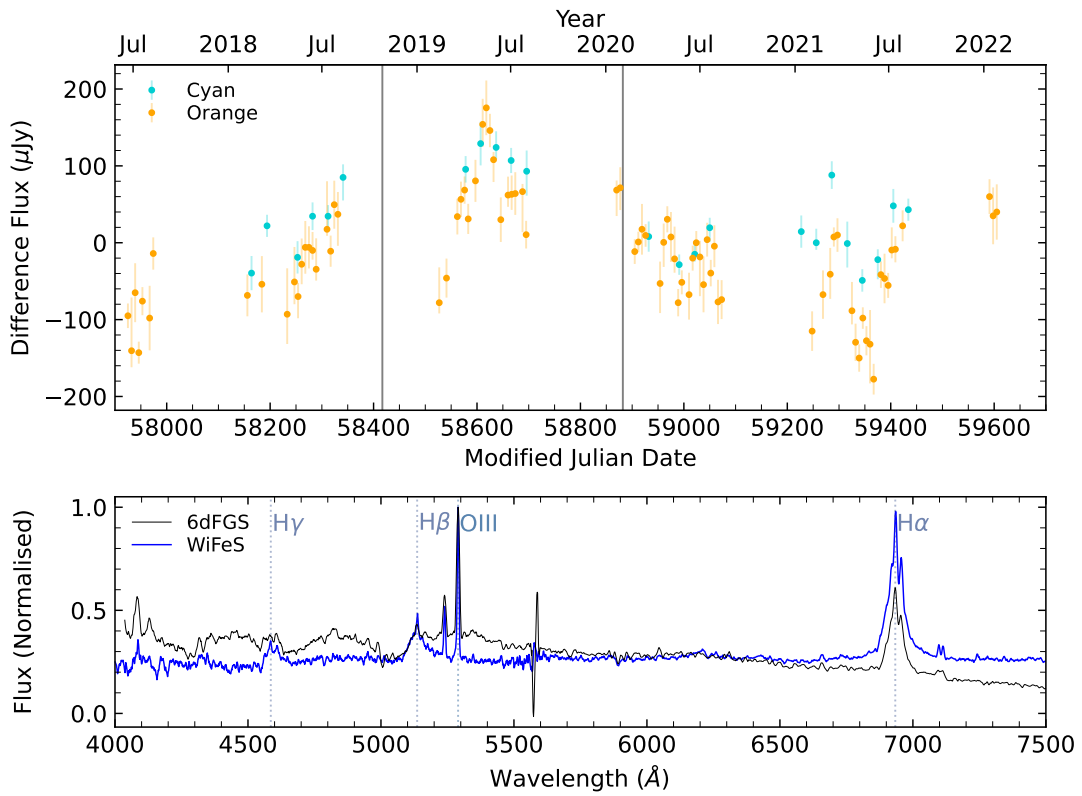ATLAS lightcurve (top) and 6dFGS+WiFeS spectra (bottom) for **g1051463-415947** with **6dFAGN type-2**.
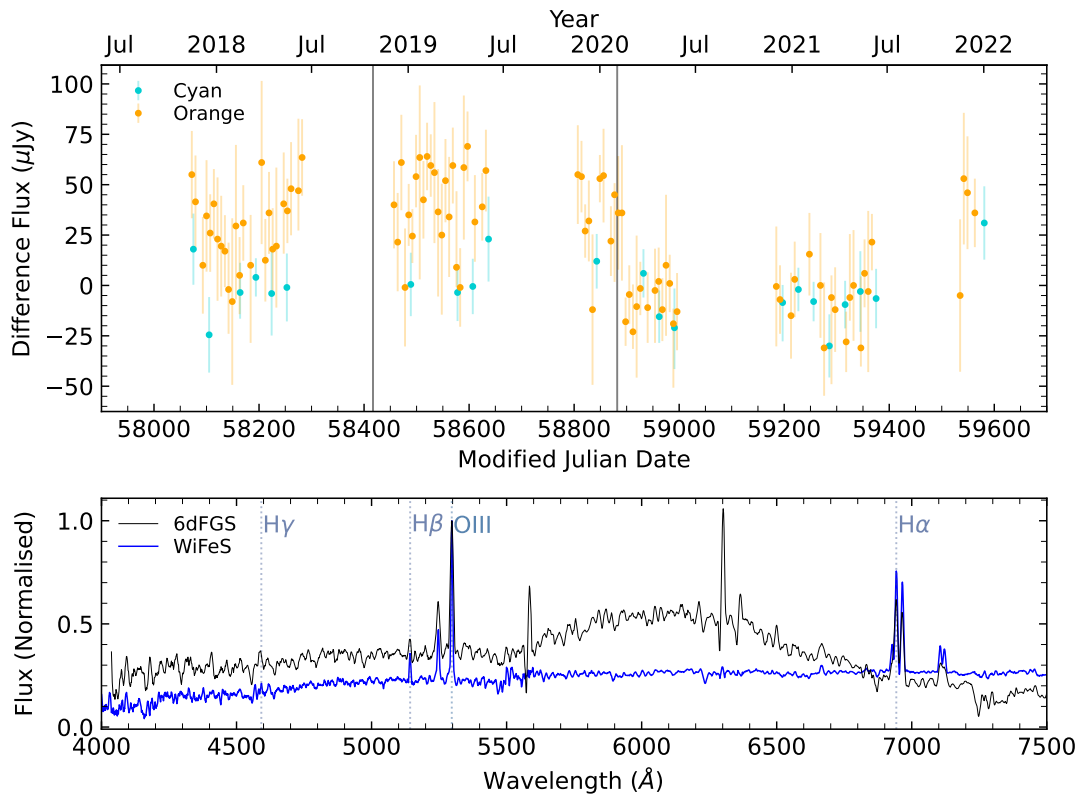
ATLAS lightcurve (top) and 6dFGS+WiFeS spectra (bottom) for **g1054326-413625** with **6dFAGN type-2**.
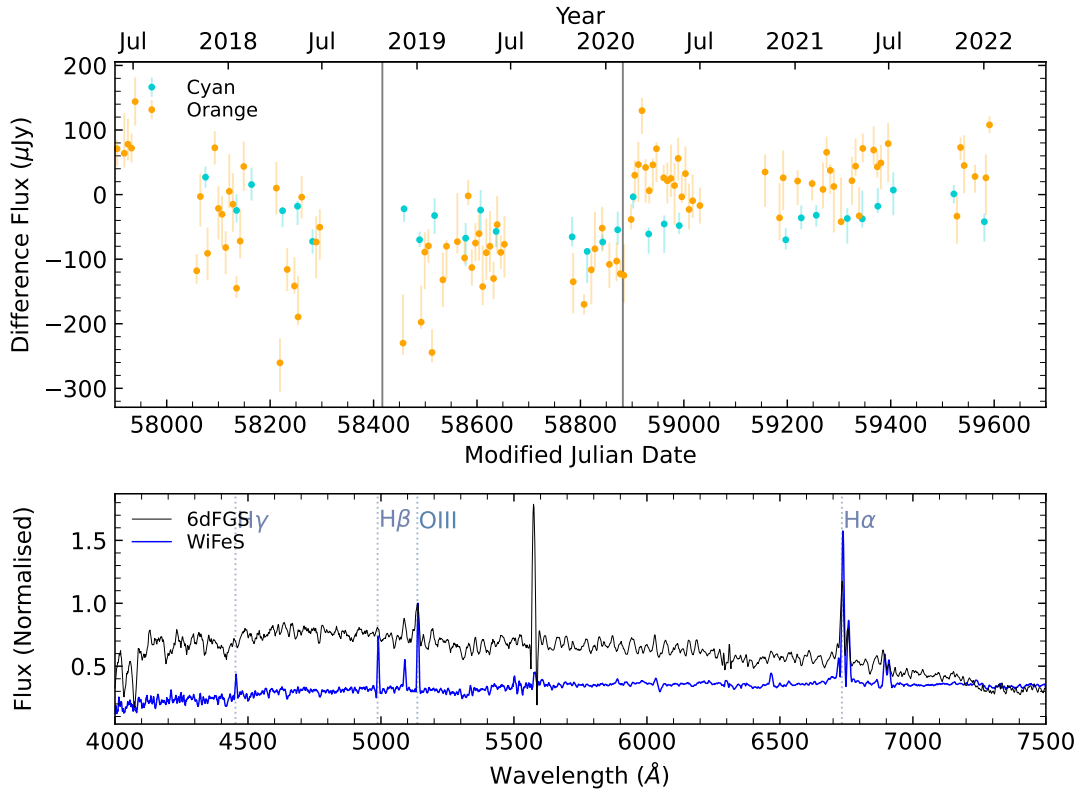
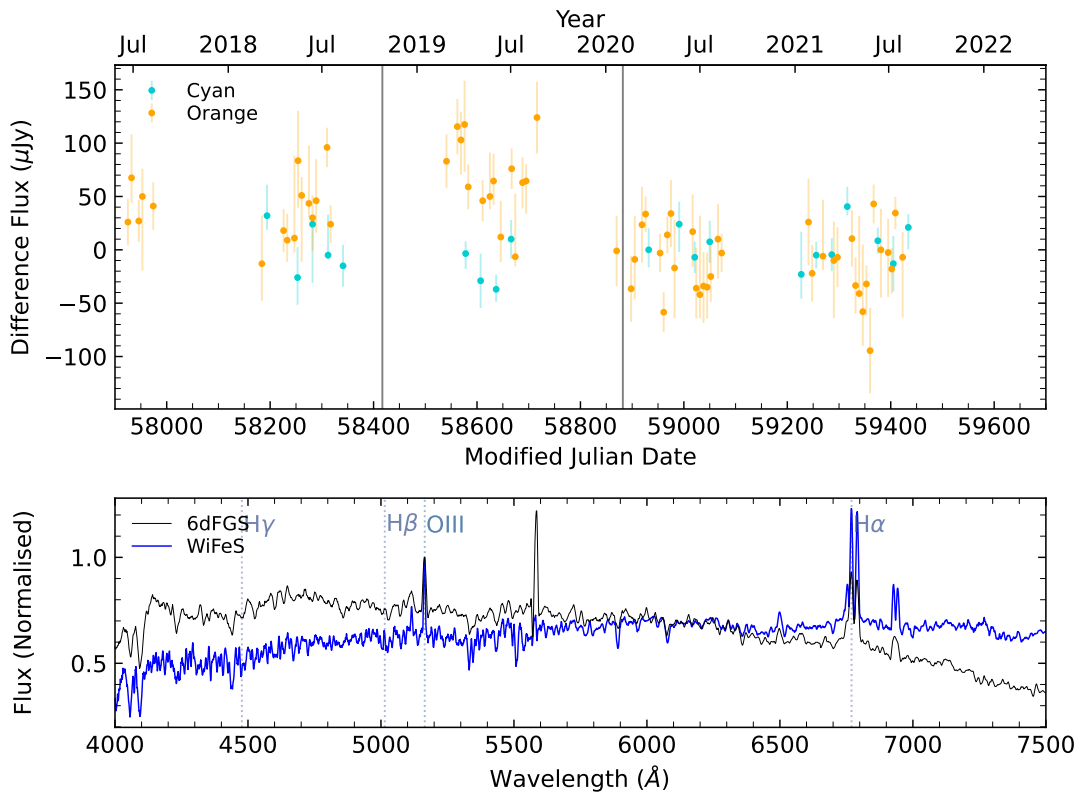ATLAS lightcurve (top) and 6dFGS+WiFeS spectra (bottom) for **g1101298-122659** with **6dFAGN type-2**.
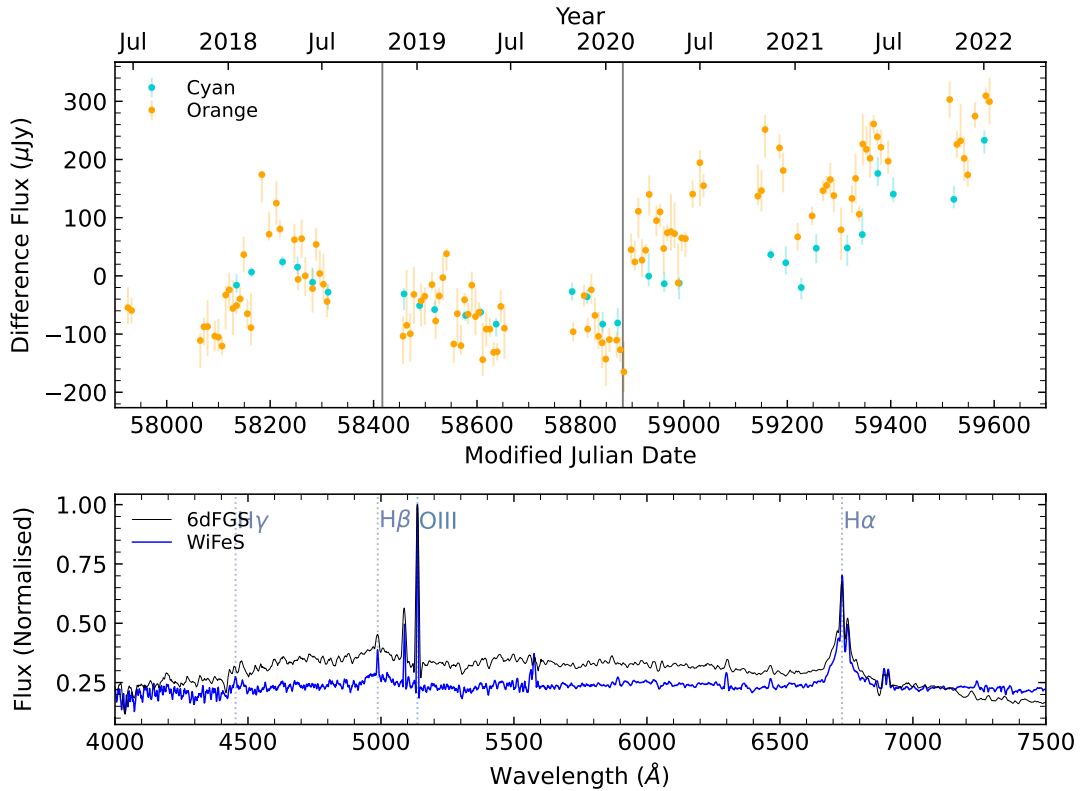
ATLAS lightcurve (top) and 6dFGS+WiFeS spectra (bottom) for **g1103168-065417** with **6dFAGN type-1.9**.
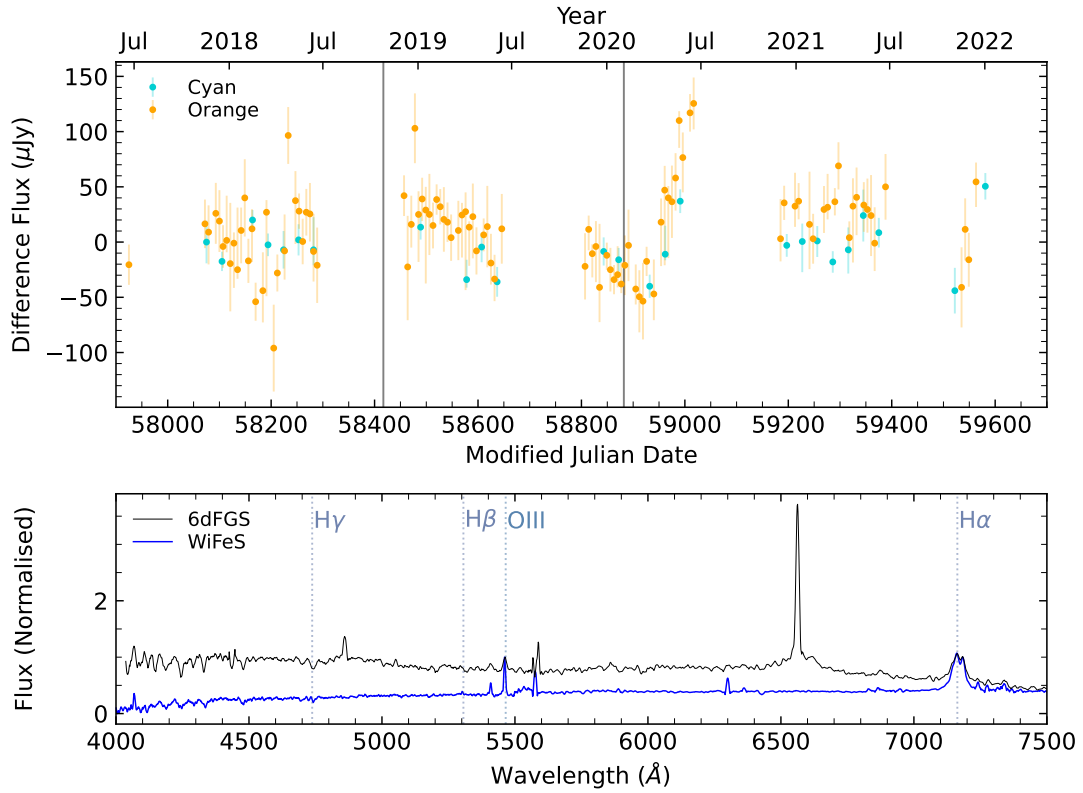
ATLAS lightcurve (top) and 6dFGS+WiFeS spectra (bottom) for **g1105372-364750** with **6dFAGN type-2**.
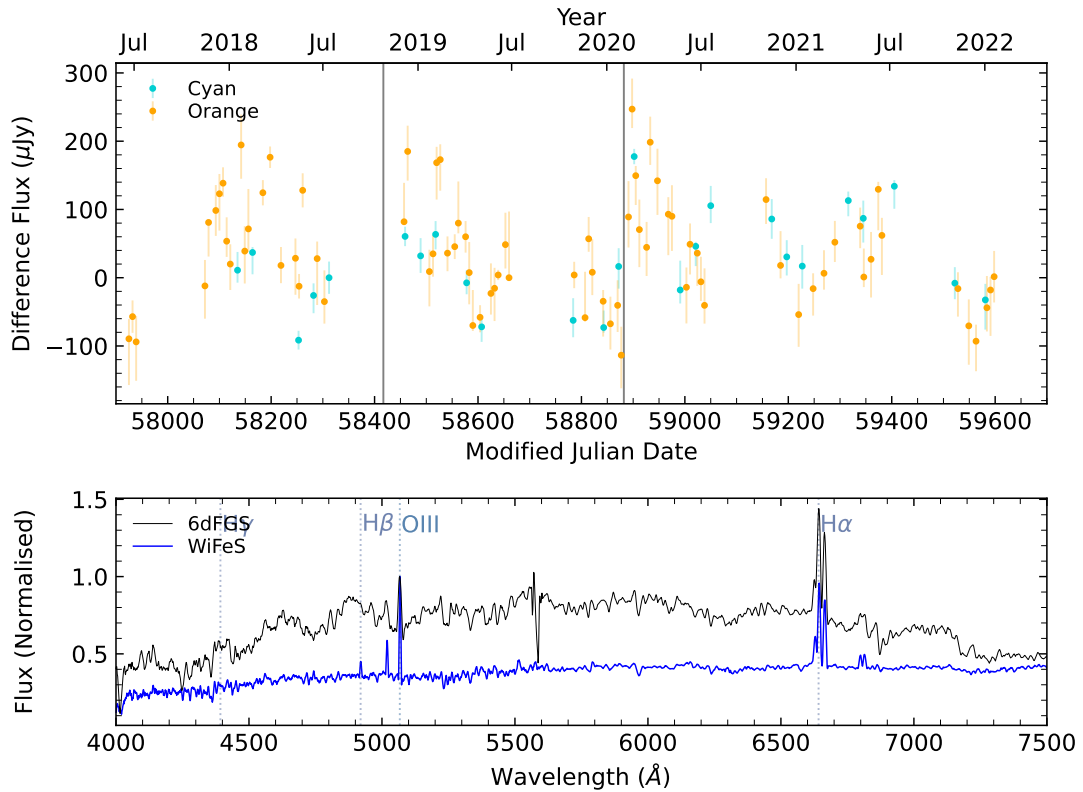
ATLAS lightcurve (top) and 6dFGS+WiFeS spectra (bottom) for **g1123323-083931** with **6dFAGN type-2**.
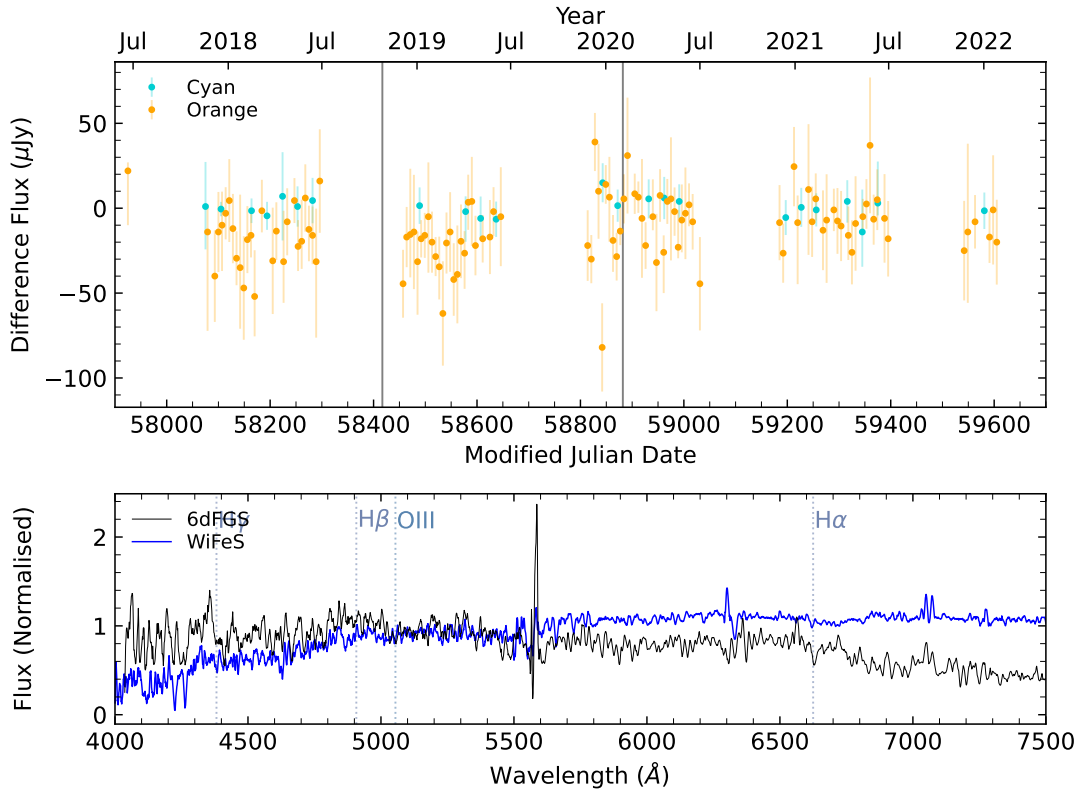
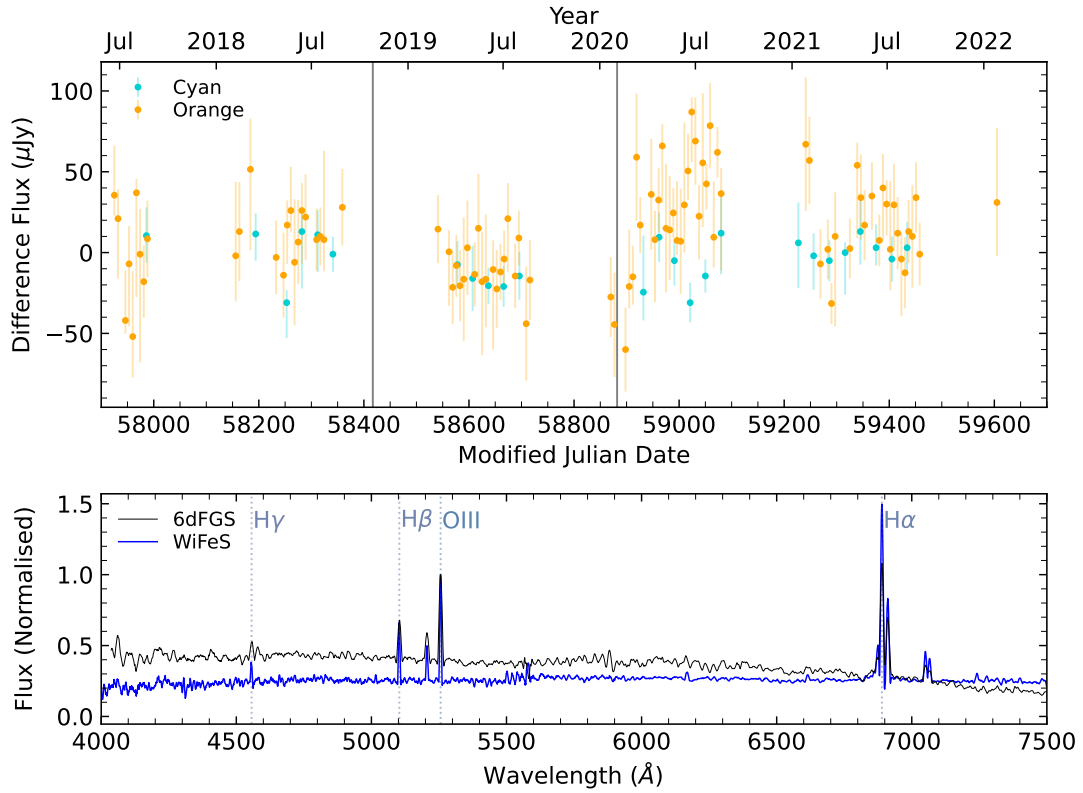ATLAS lightcurve (top) and 6dFGS+WiFeS spectra (bottom) for **g1134475-361011** with **6dFAGN type-1.5**.
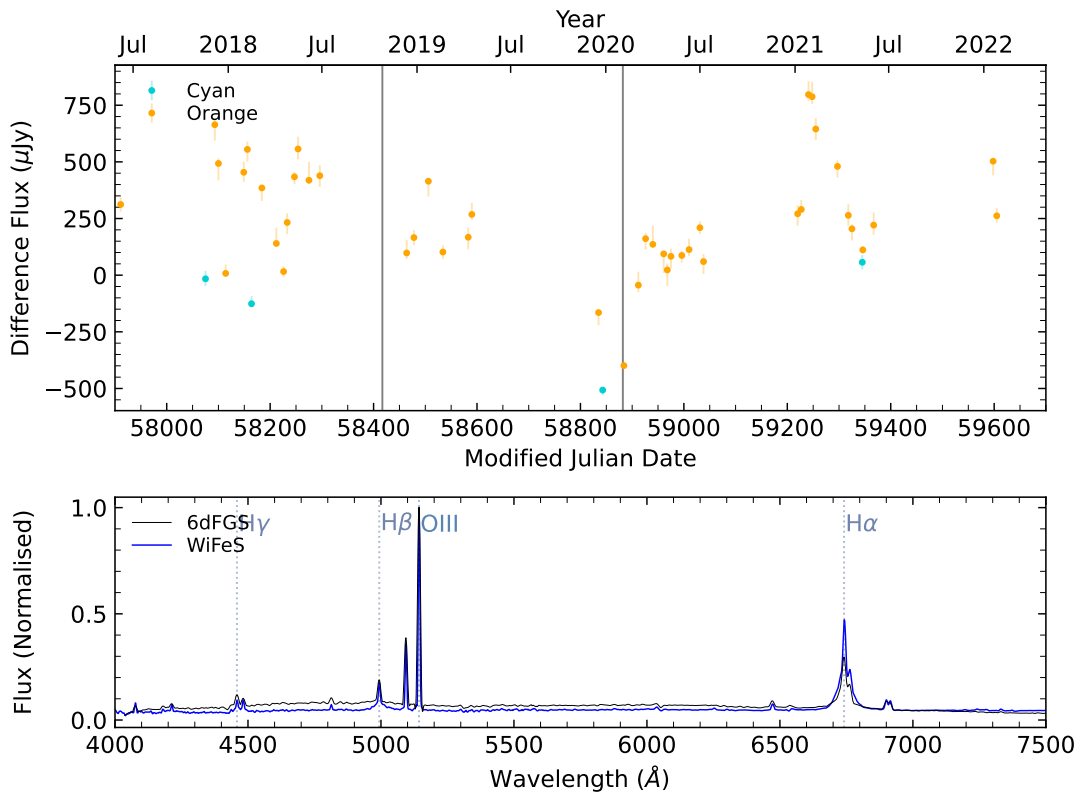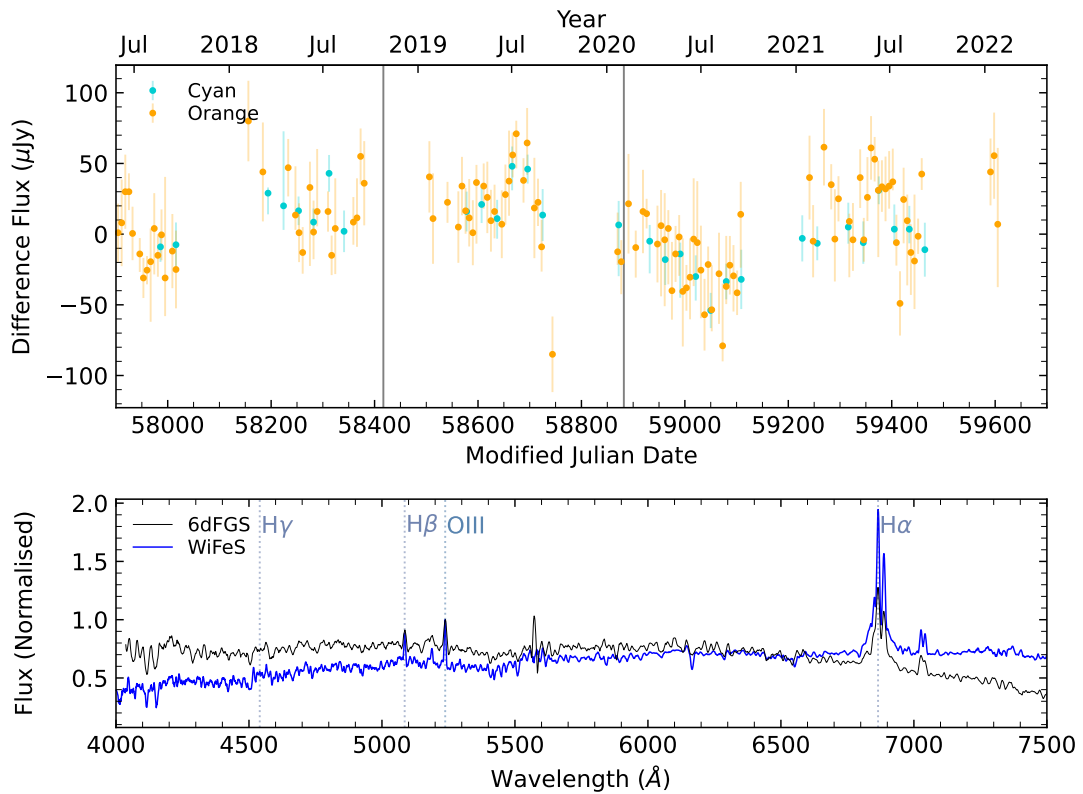

ATLAS lightcurve (top) and 6dFGS+WiFeS spectra (bottom) for **g1138510-232135** with **6dFAGN type-1.9**.
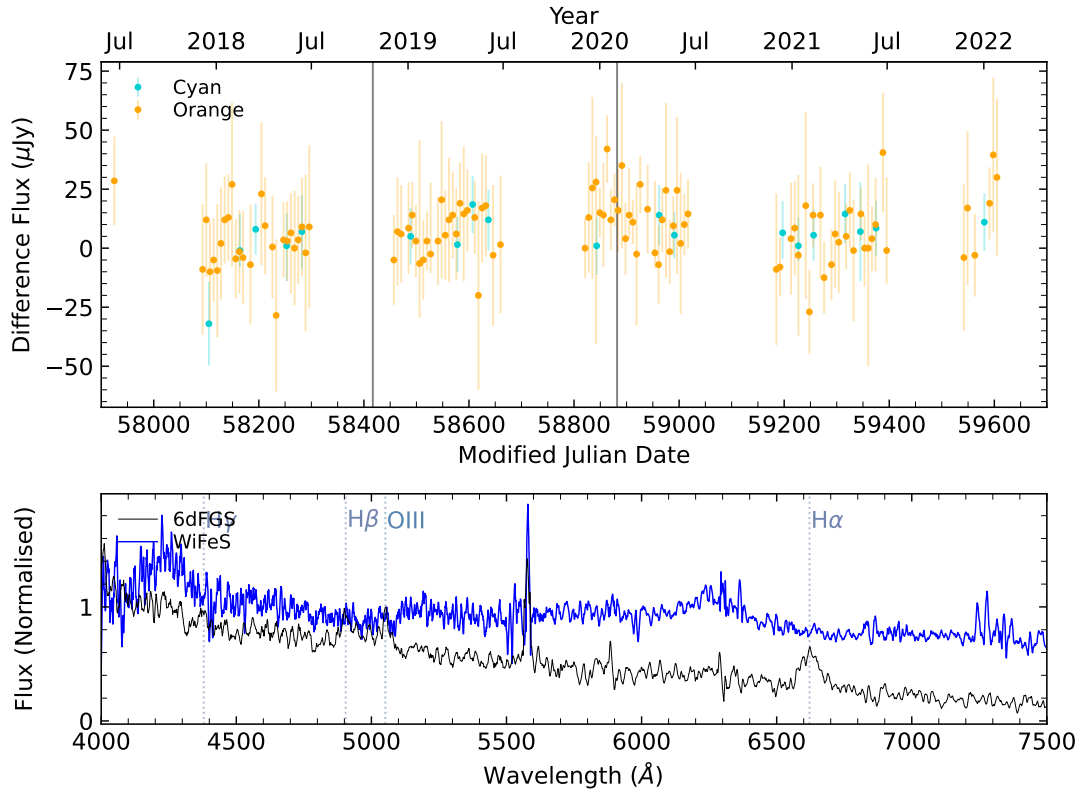
ATLAS lightcurve (top) and 6dFGS+WiFeS spectra (bottom) for **g1138589-380042** with **6dFAGN type-1**. Confirmed cross talk (see Table 2.1).
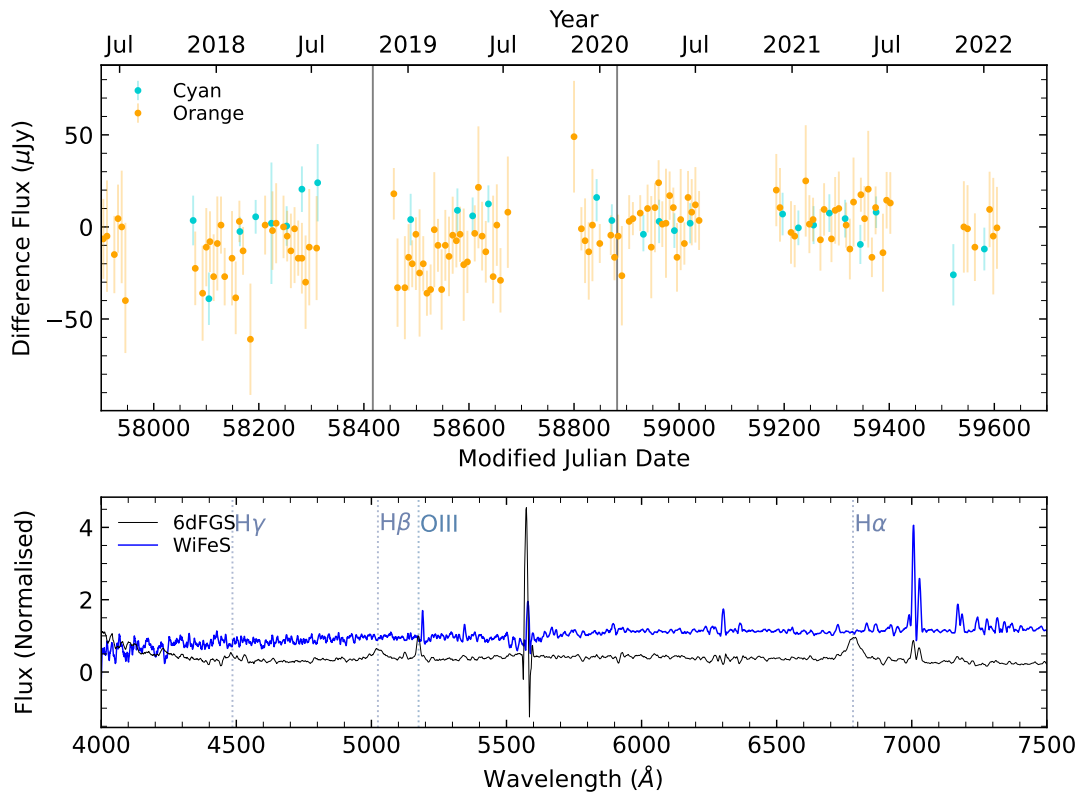
ATLAS lightcurve (top) and 6dFGS+WiFeS spectra (bottom) for **g1148026-184952** with **6dFAGN type-1.5**. Confirmed cross talk (see Table 2.1).
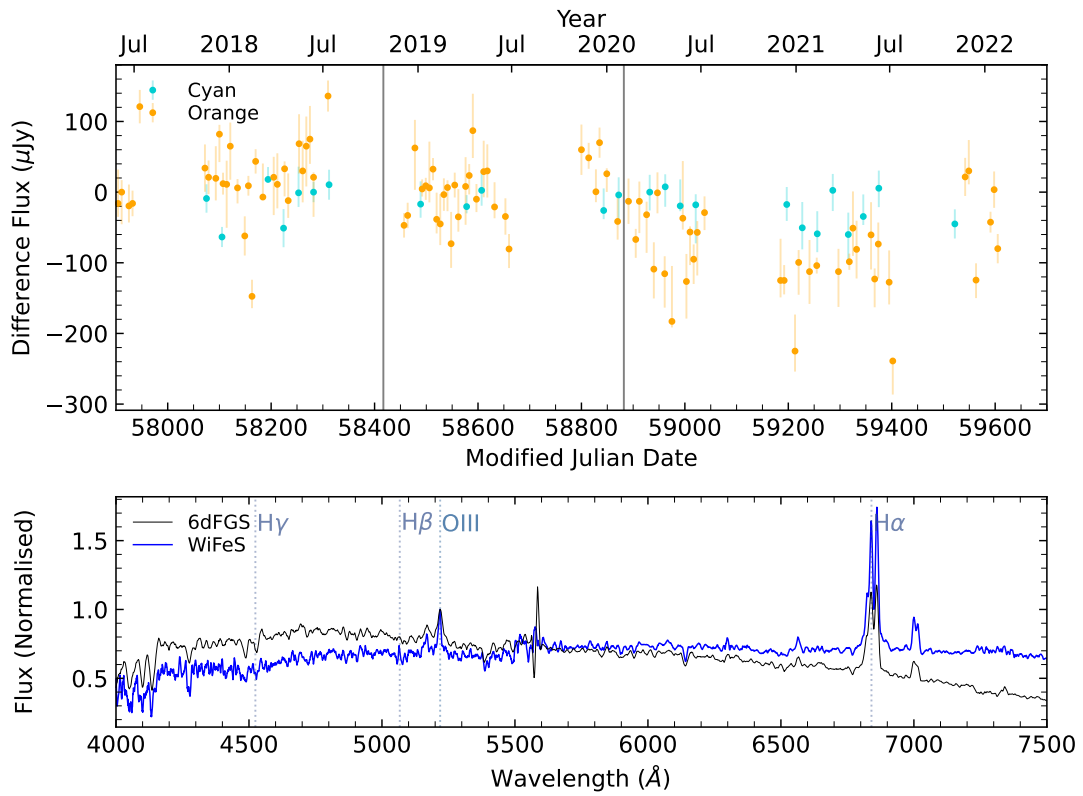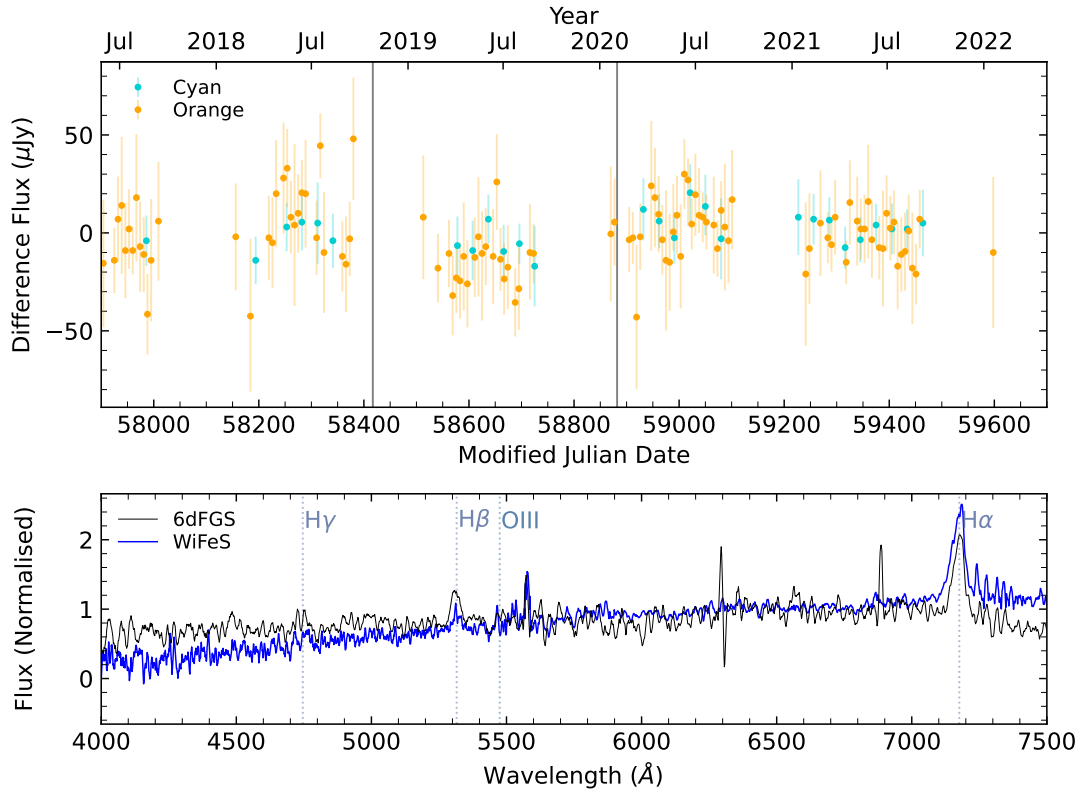
ATLAS lightcurve (top) and 6dFGS+WiFeS spectra (bottom) for **g1156158-205430** with **6dFAGN type-2**.
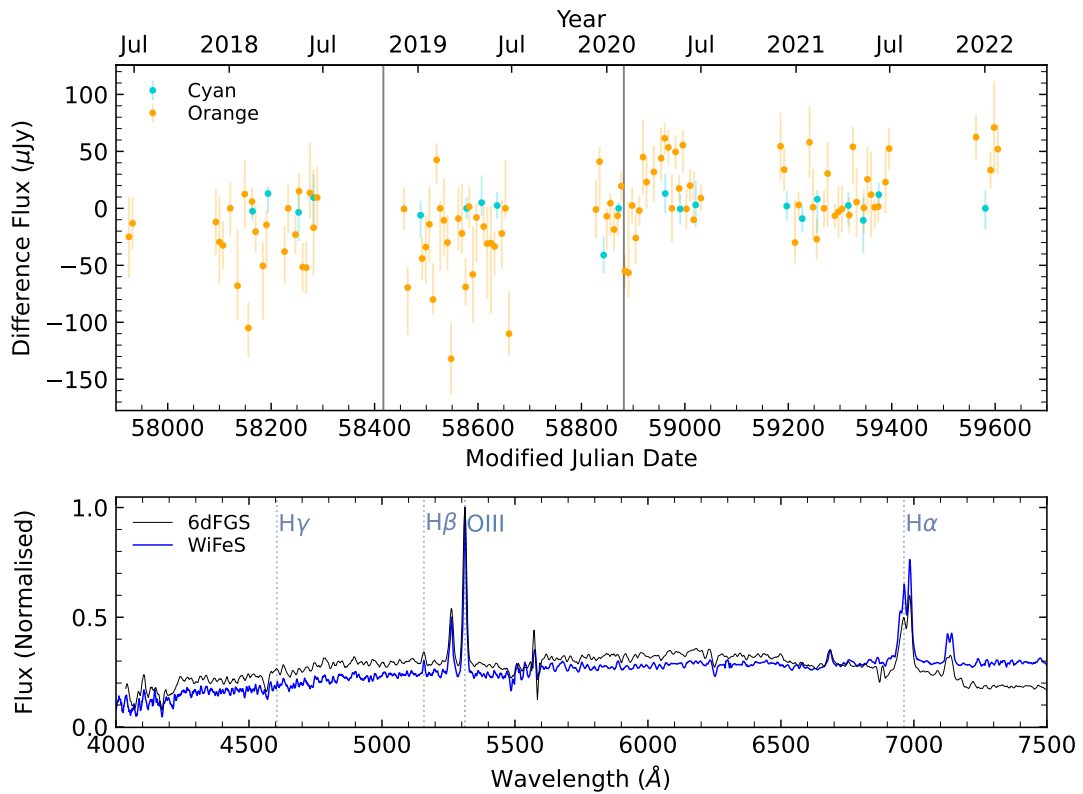
ATLAS lightcurve (top) and 6dFGS+WiFeS spectra (bottom) for **g1211143-393327** with **6dFAGN type-2**.
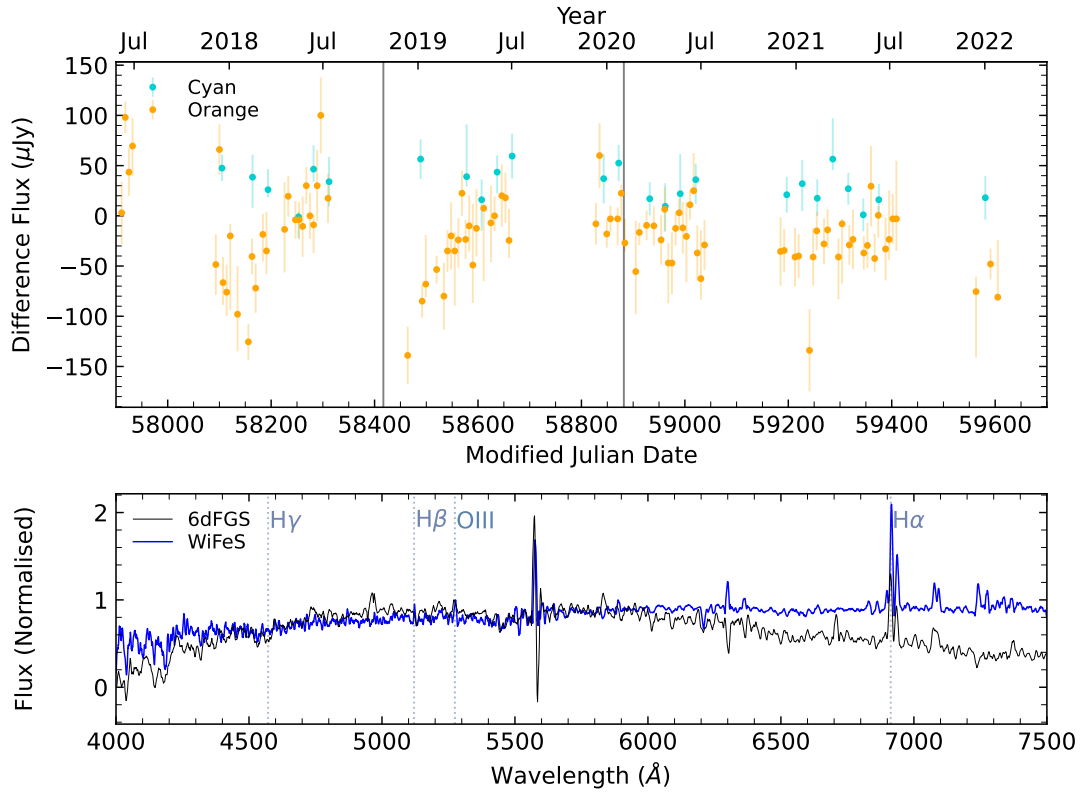
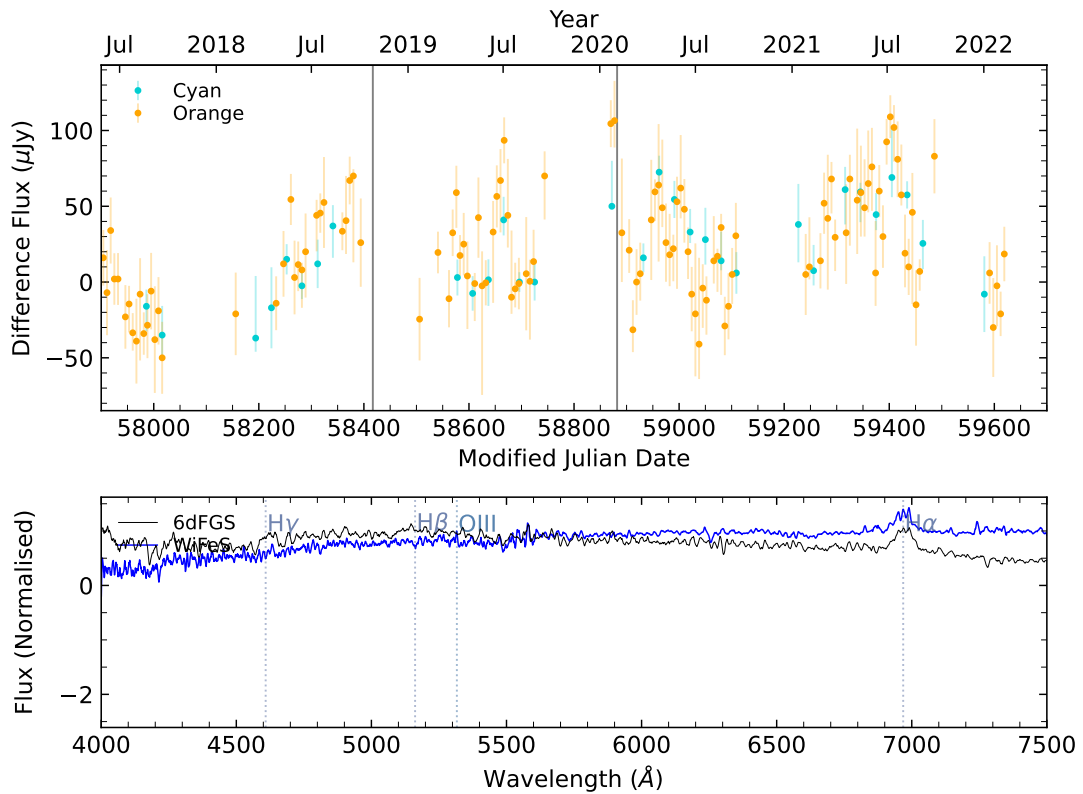ATLAS lightcurve (top) and 6dFGS+WiFeS spectra (bottom) for **g1235322-345447** with **6dFAGN type-2**.
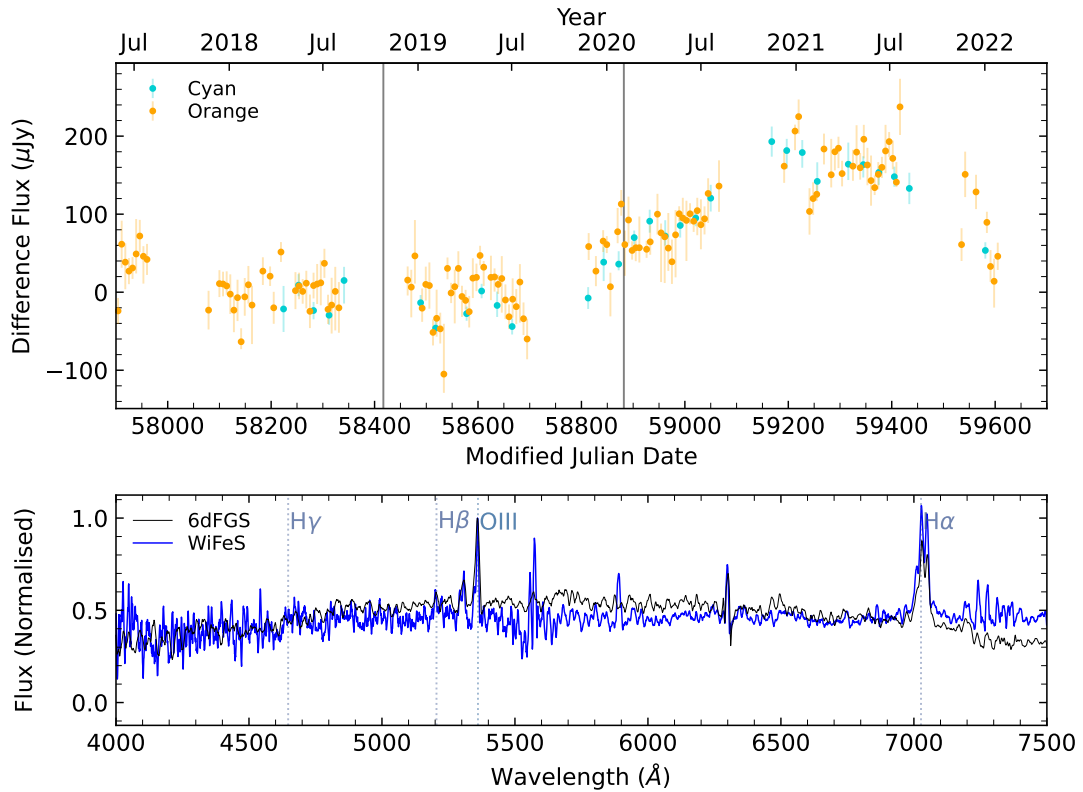
ATLAS lightcurve (top) and 6dFGS+WiFeS spectra (bottom) for **g1238084-091412** with **6dFAGN type-2**.
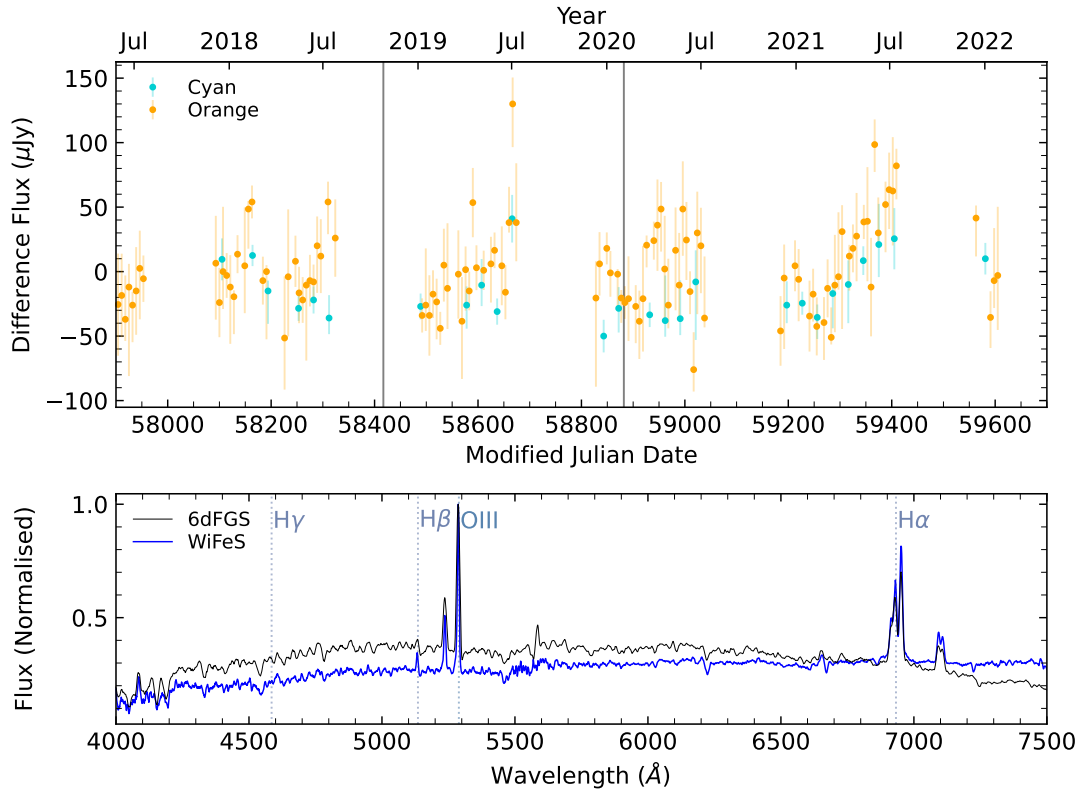
ATLAS lightcurve (top) and 6dFGS+WiFeS spectra (bottom) for **g1246107-314836** with **6dFAGN type-2**.
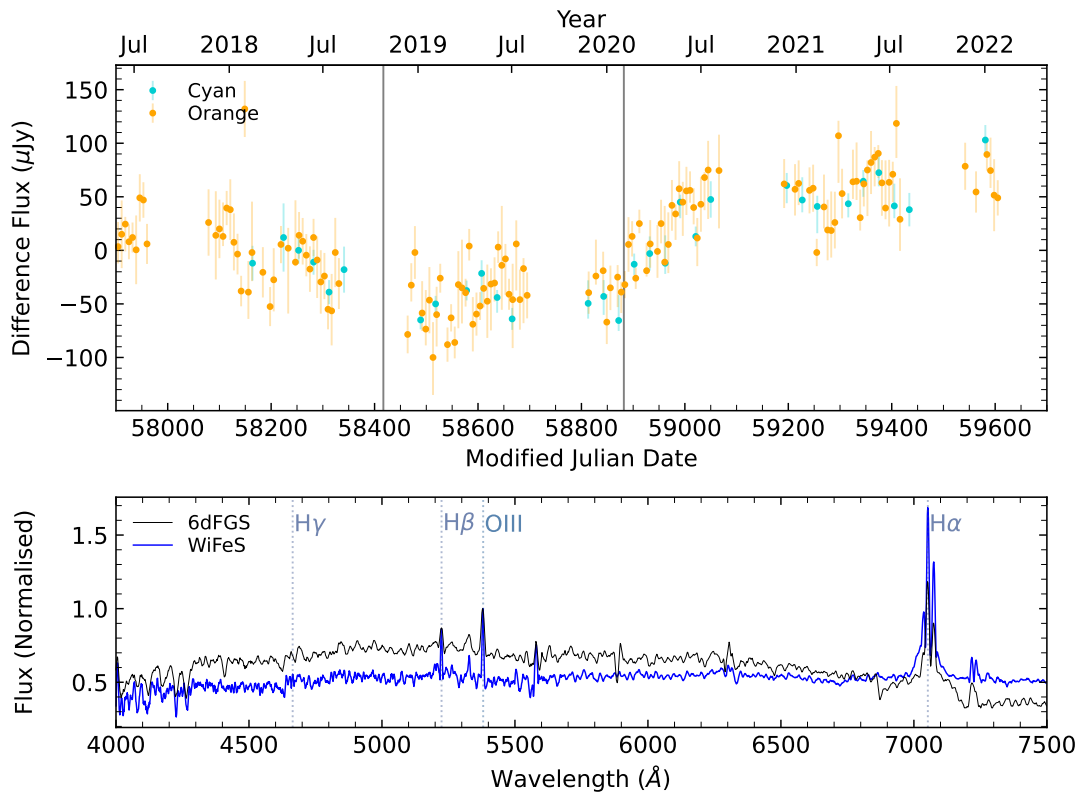
ATLAS lightcurve (top) and 6dFGS+WiFeS spectra (bottom) for **g1249104-114925** with **6dFAGN type-1.9**.
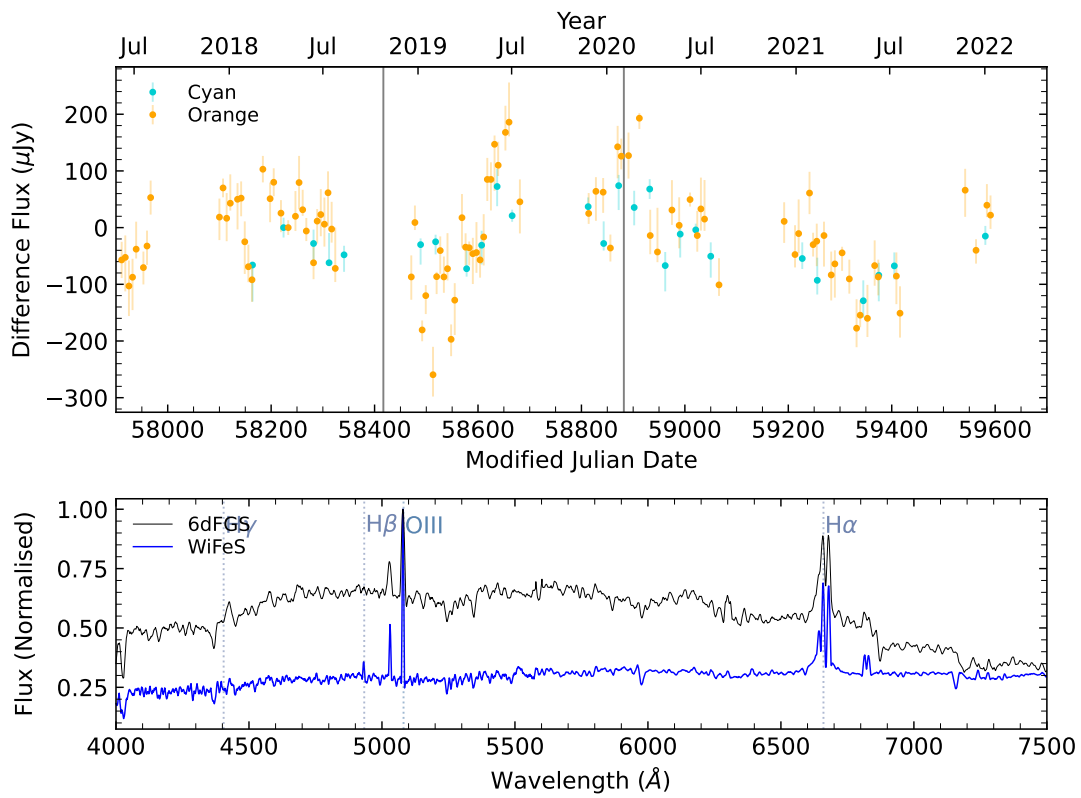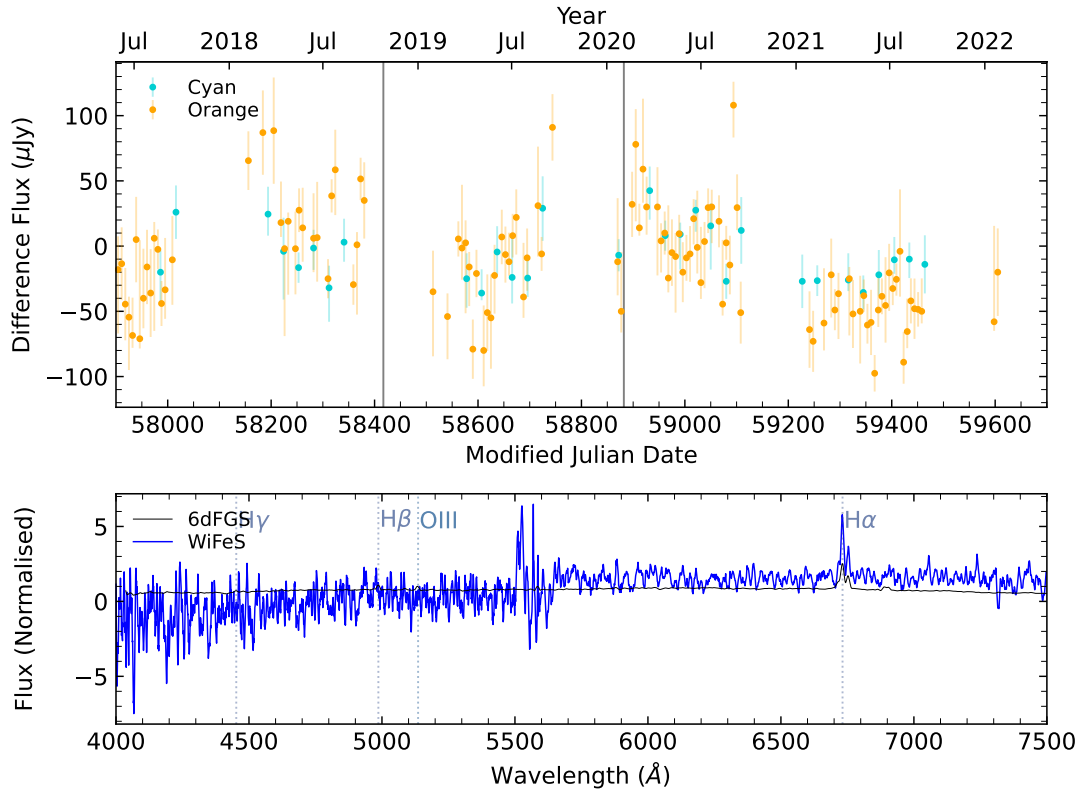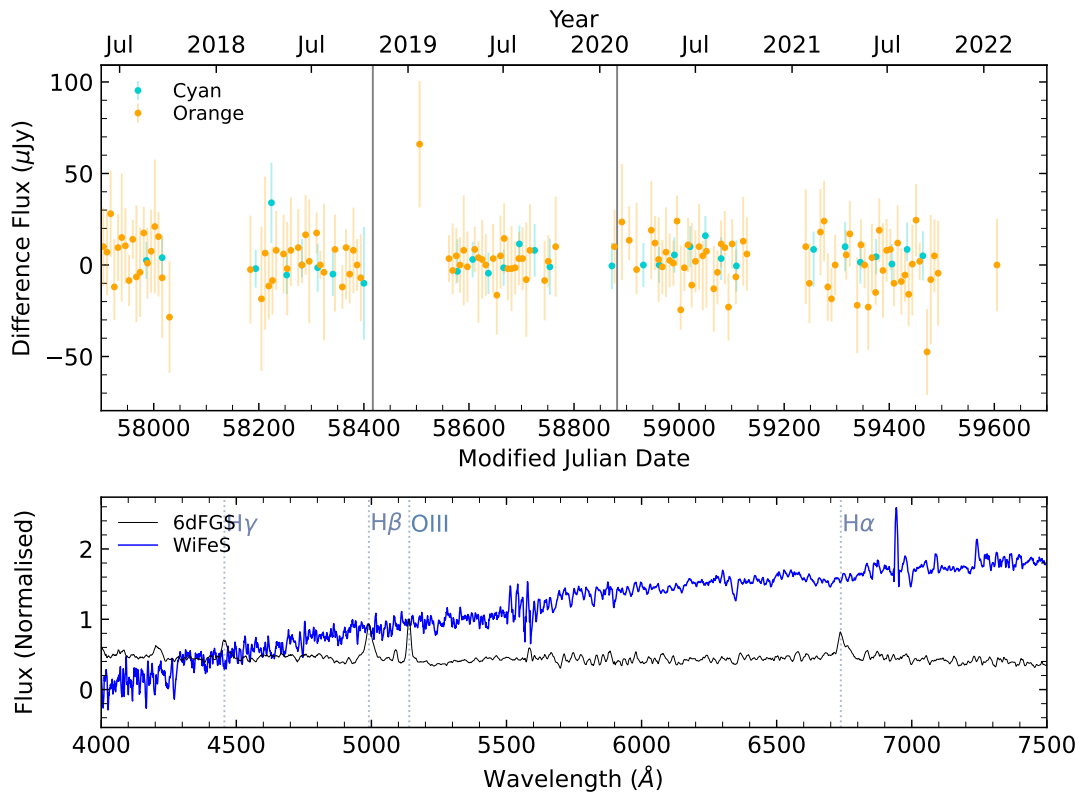
ATLAS lightcurve (top) and 6dFGS+WiFeS spectra (bottom) for **g1251324-141316** with **6dFAGN type-1.9**.
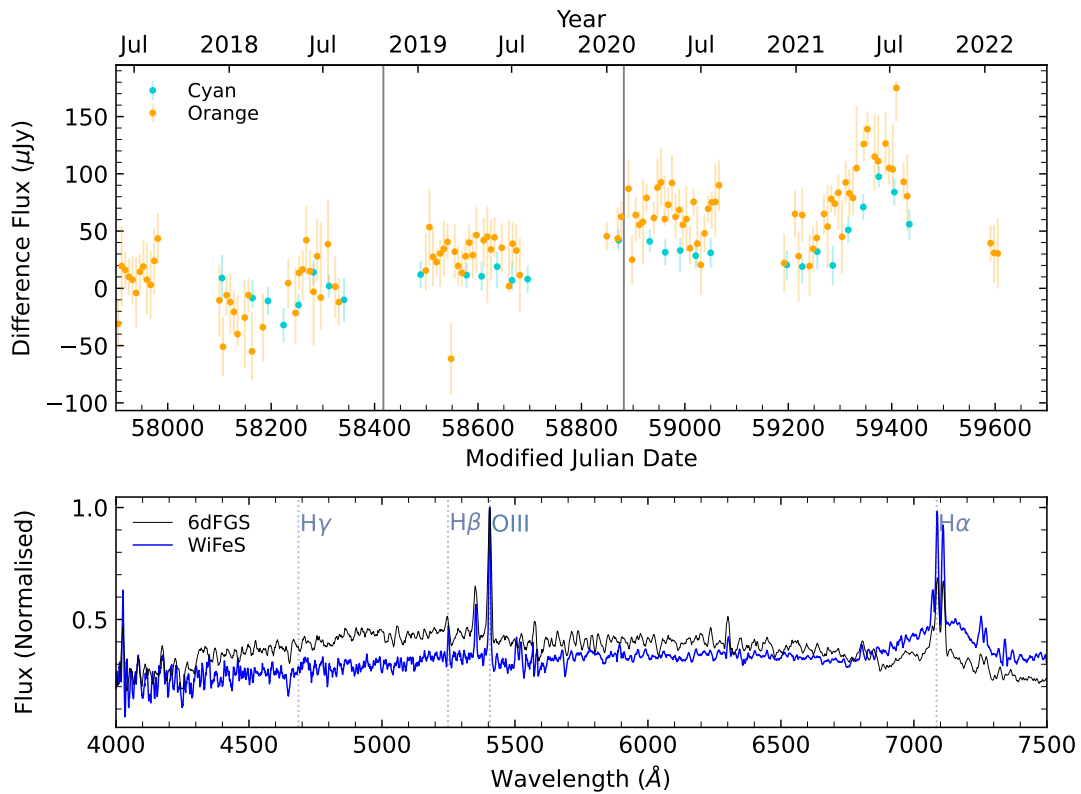
ATLAS lightcurve (top) and 6dFGS+WiFeS spectra (bottom) for **g1344330-225801** with **6dFAGN type-2**.
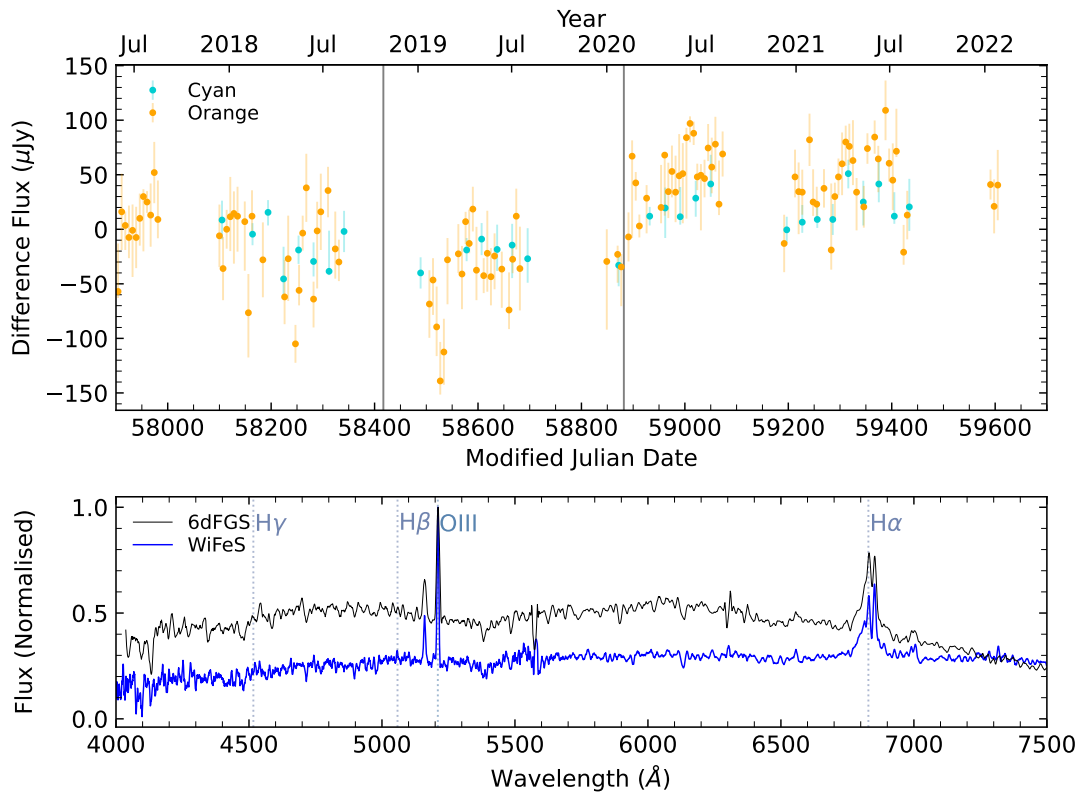
ATLAS lightcurve (top) and 6dFGS+WiFeS spectra (bottom) for **g1349195-230042** with **6dFAGN type-2**.
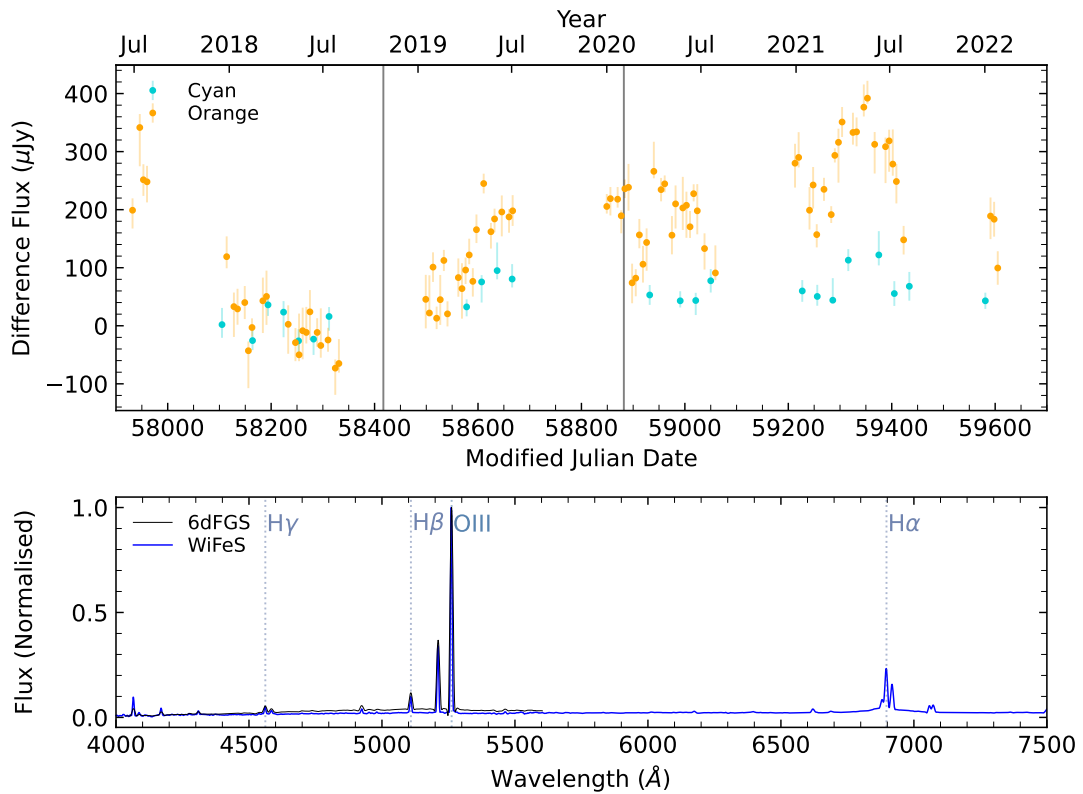
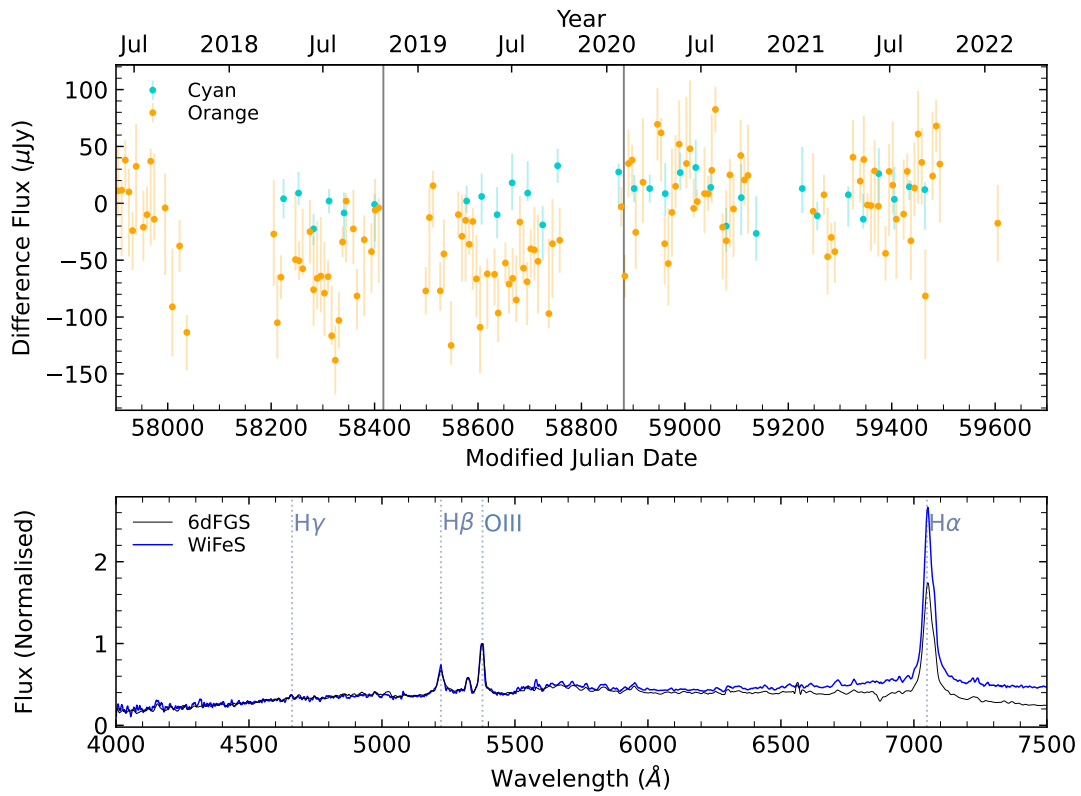ATLAS lightcurve (top) and 6dFGS+WiFeS spectra (bottom) for **g1354154-374633** with **6dFAGN type-2**.
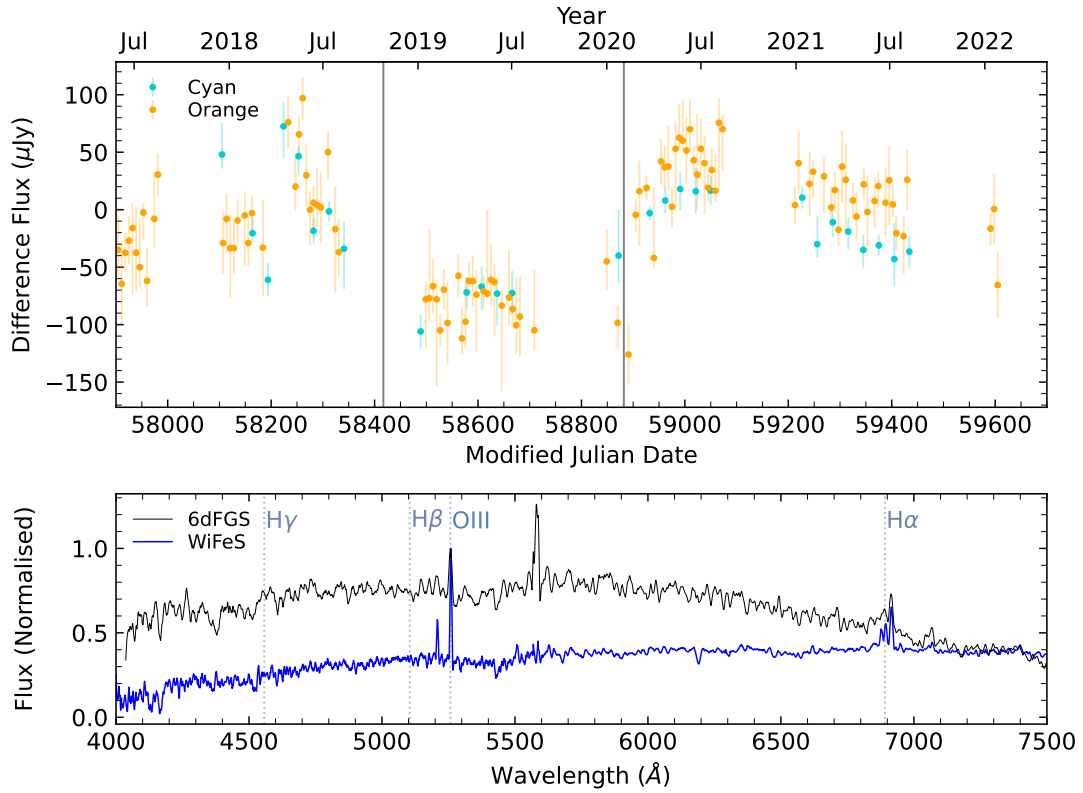
ATLAS lightcurve (top) and 6dFGS+WiFeS spectra (bottom) for **g1356131-274458** with **6dFAGN type-2**.
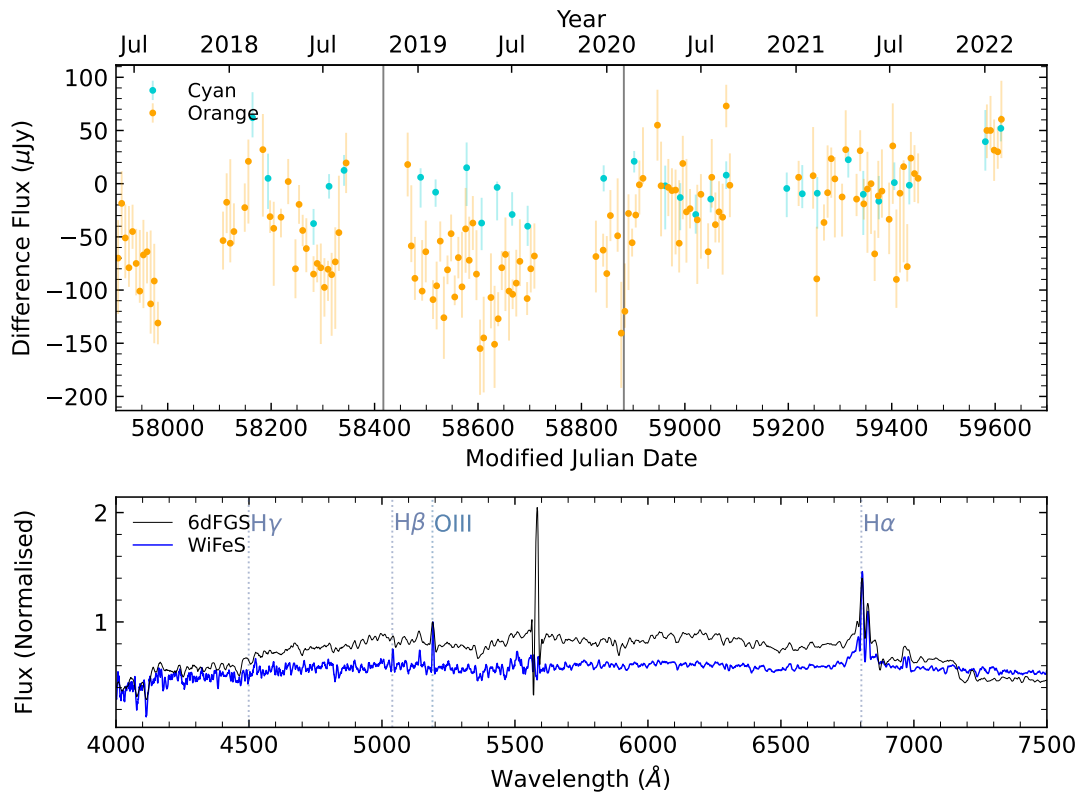
ATLAS lightcurve (top) and 6dFGS+WiFeS spectra (bottom) for **g1401018-111223** with **6dFAGN type-2**.
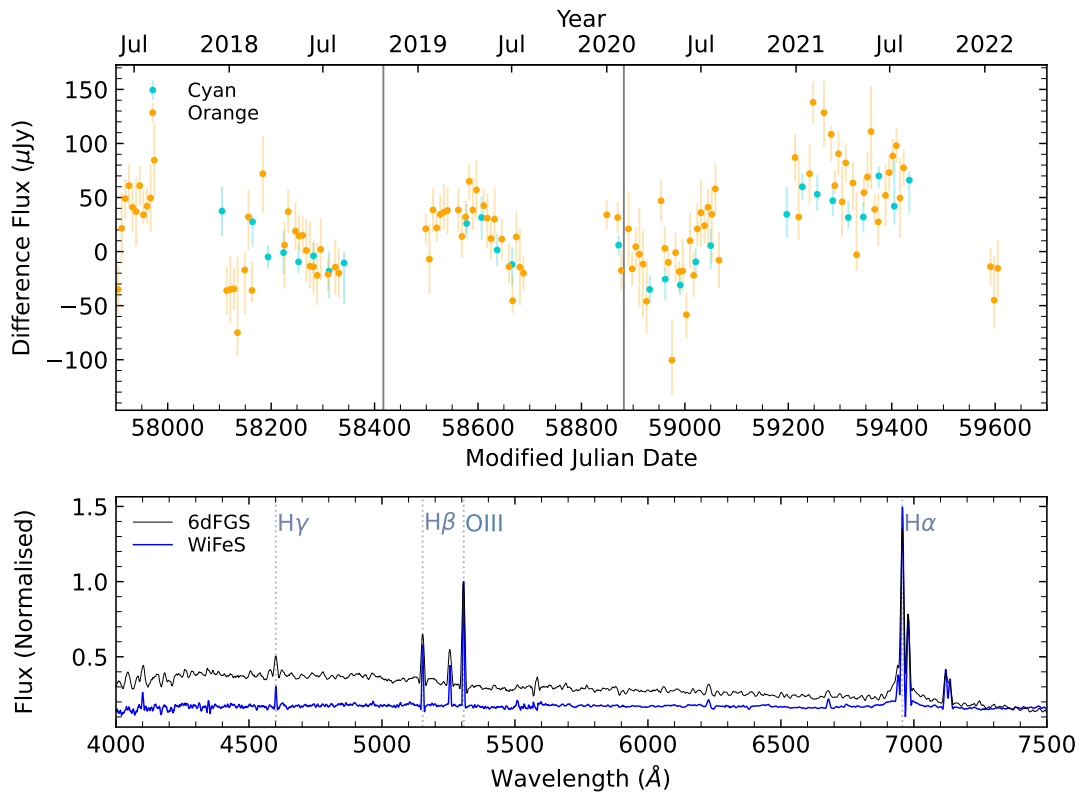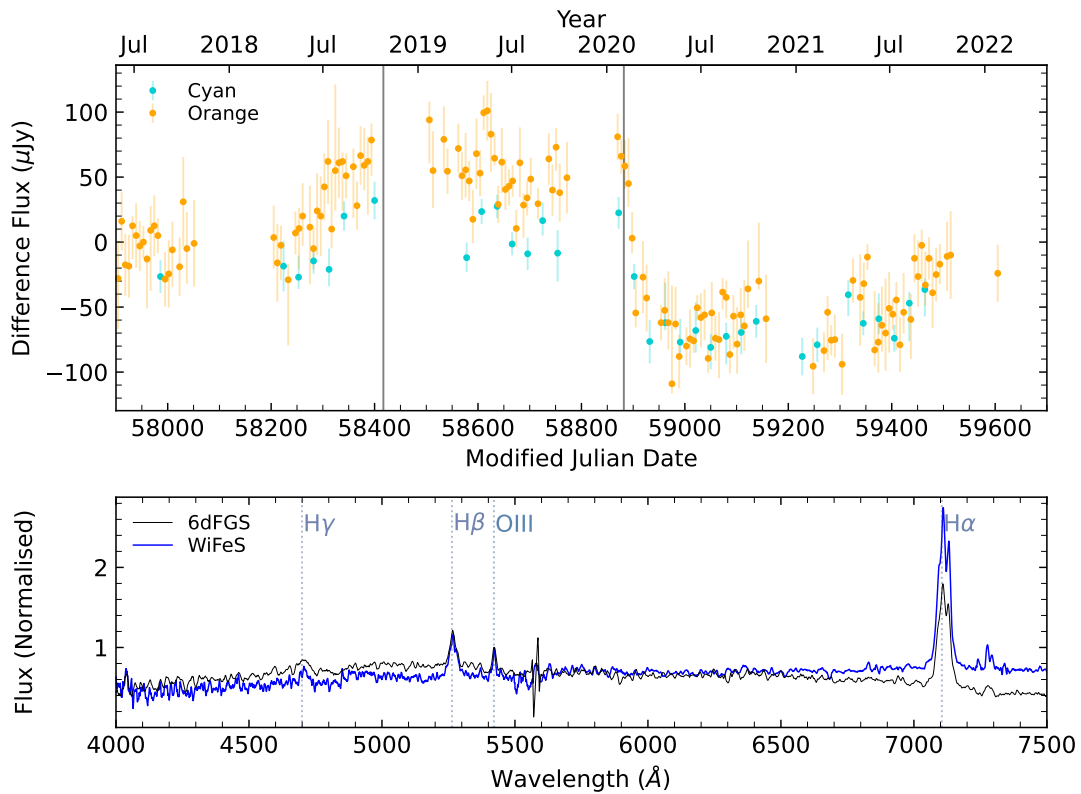
ATLAS lightcurve (top) and 6dFGS+WiFeS spectra (bottom) for **g1401157-322943** with **6dFAGN type-1.9**.
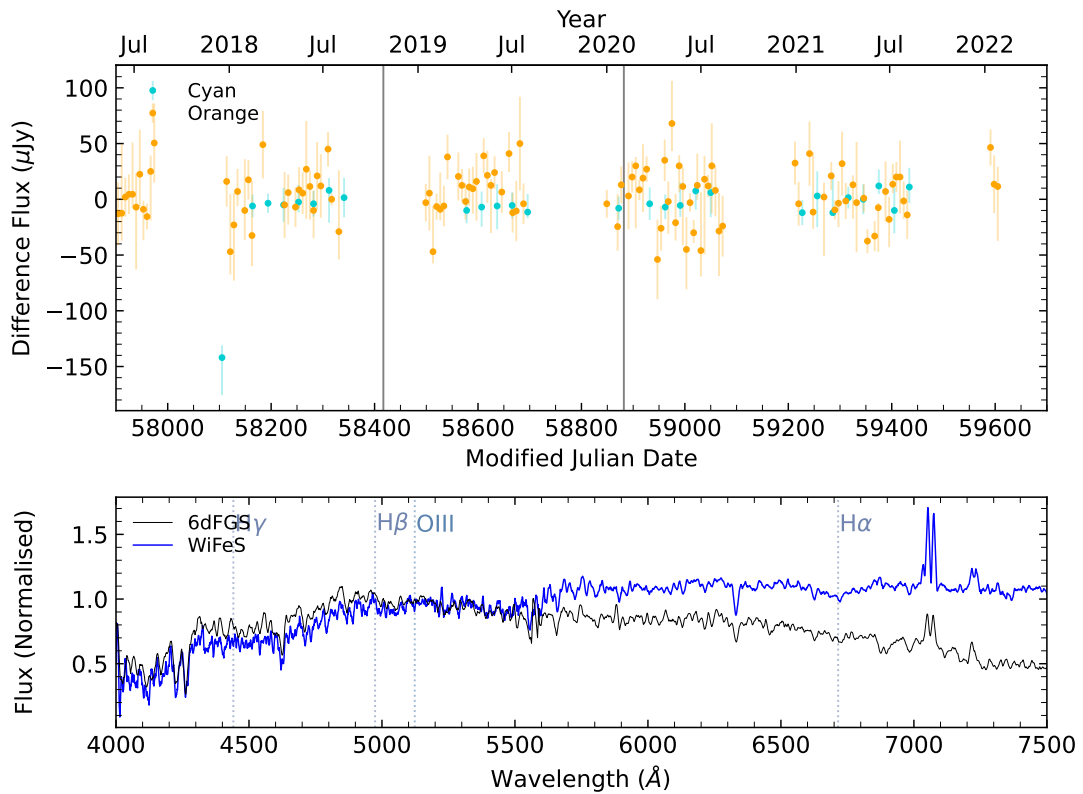
ATLAS lightcurve (top) and 6dFGS+WiFeS spectra (bottom) for **g1405106-310335** with **6dFAGN type-1.5**.

ATLAS lightcurve (top) and 6dFGS+WiFeS spectra (bottom) for **g1410293-241748** with **6dFAGN type-2**.

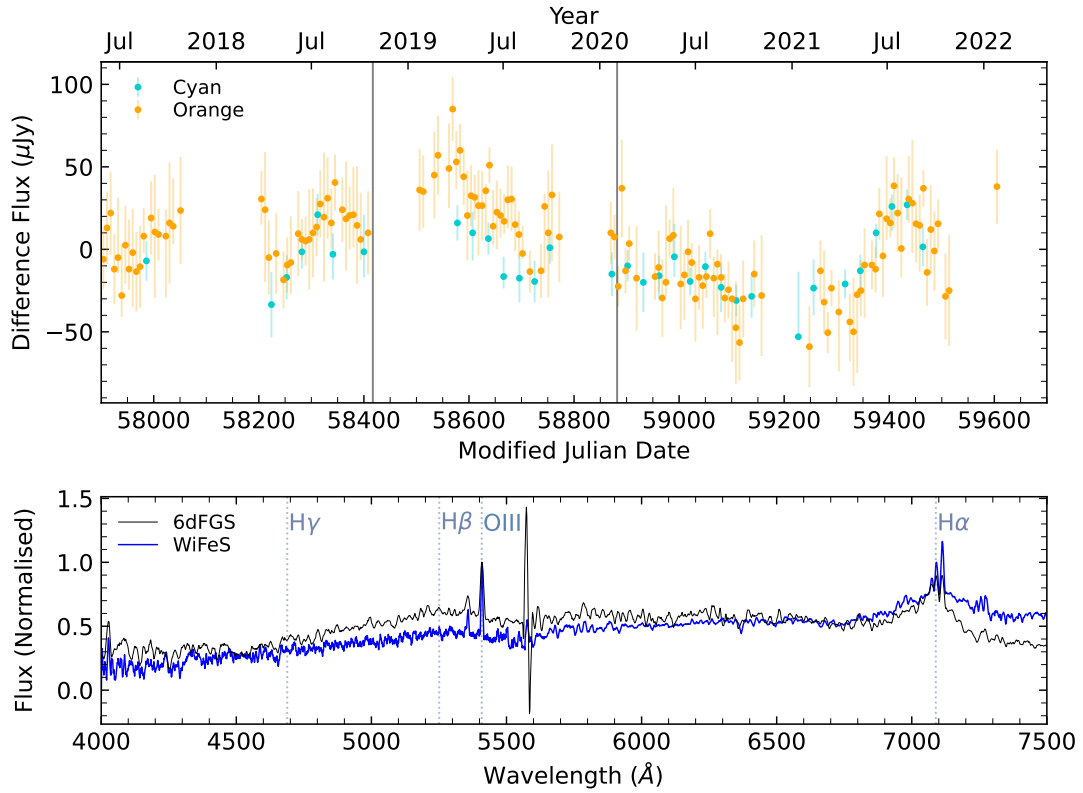ATLAS lightcurve (top) and 6dFGS+WiFeS spectra (bottom) for **g1412197-214708** with **6dFAGN type-2**.

ATLAS lightcurve (top) and 6dFGS+WiFeS spectra (bottom) for **g1412348-185625** with **6dFAGN type-2**.

ATLAS lightcurve (top) and 6dFGS+WiFeS spectra (bottom) for **g1423582-050009** with **6dFAGN type-2**.

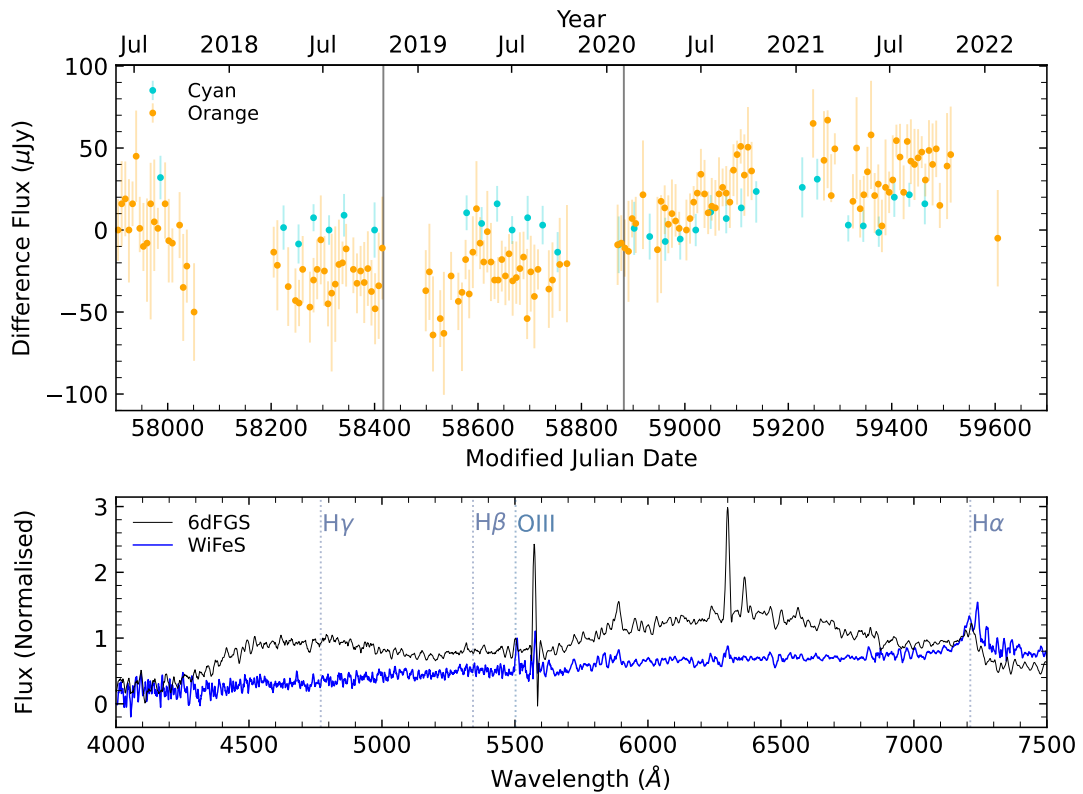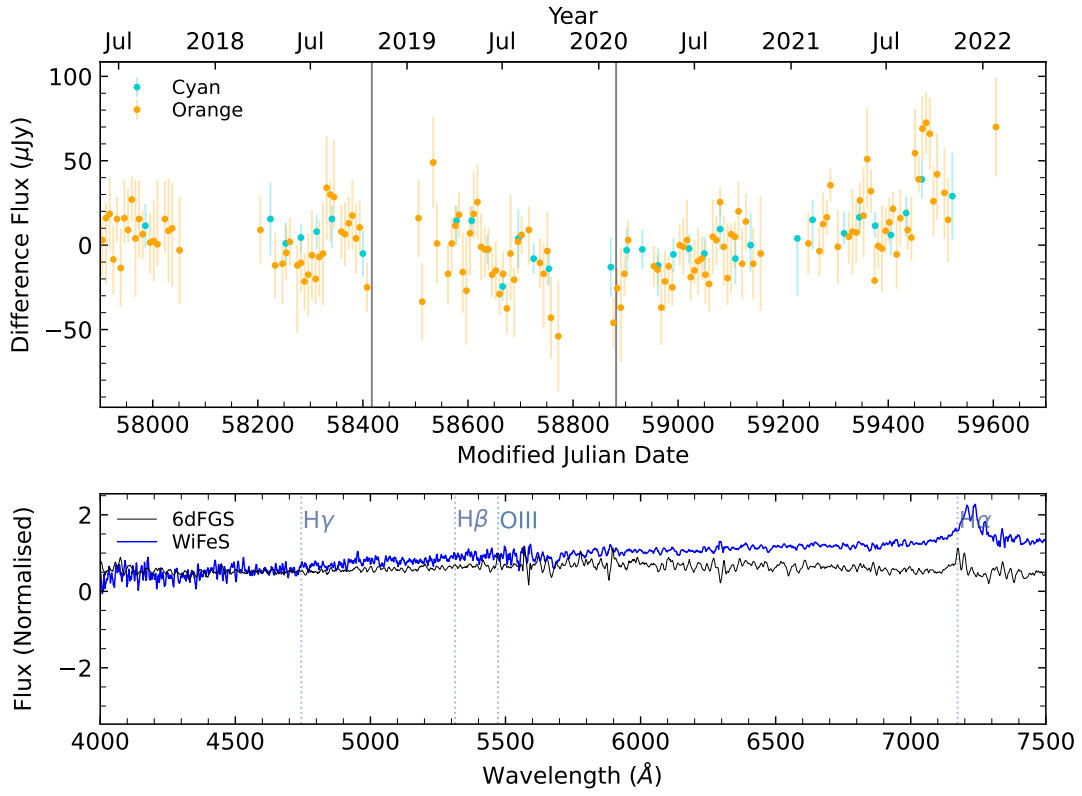ATLAS lightcurve (top) and 6dFGS+WiFeS spectra (bottom) for **g1428588-313935** with **6dFAGN type-2**.

ATLAS lightcurve (top) and 6dFGS+WiFeS spectra (bottom) for **g1437457-271803** with **6dFAGN type-1.9**.

ATLAS lightcurve (top) and 6dFGS+WiFeS spectra (bottom) for **g1452310-422625** with **6dFAGN type-1.9**.

ATLAS lightcurve (top) and 6dFGS+WiFeS spectra (bottom) for **g1453235-182615** with **6dFAGN type-1.9**.
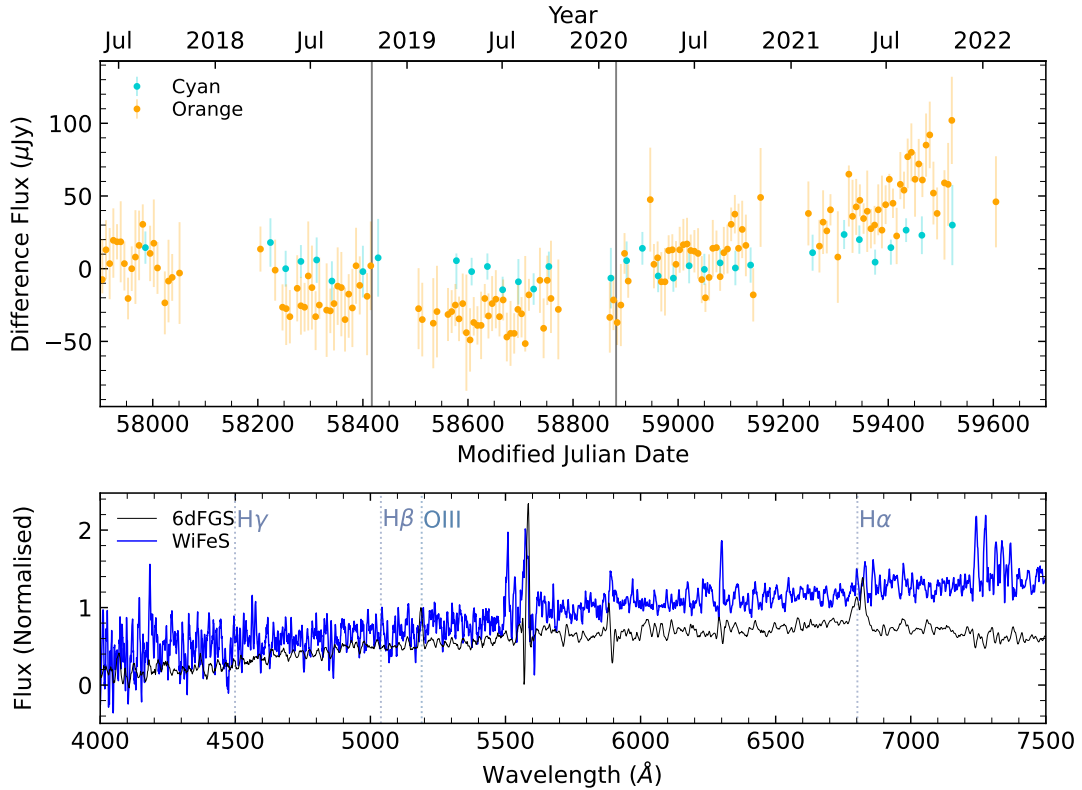
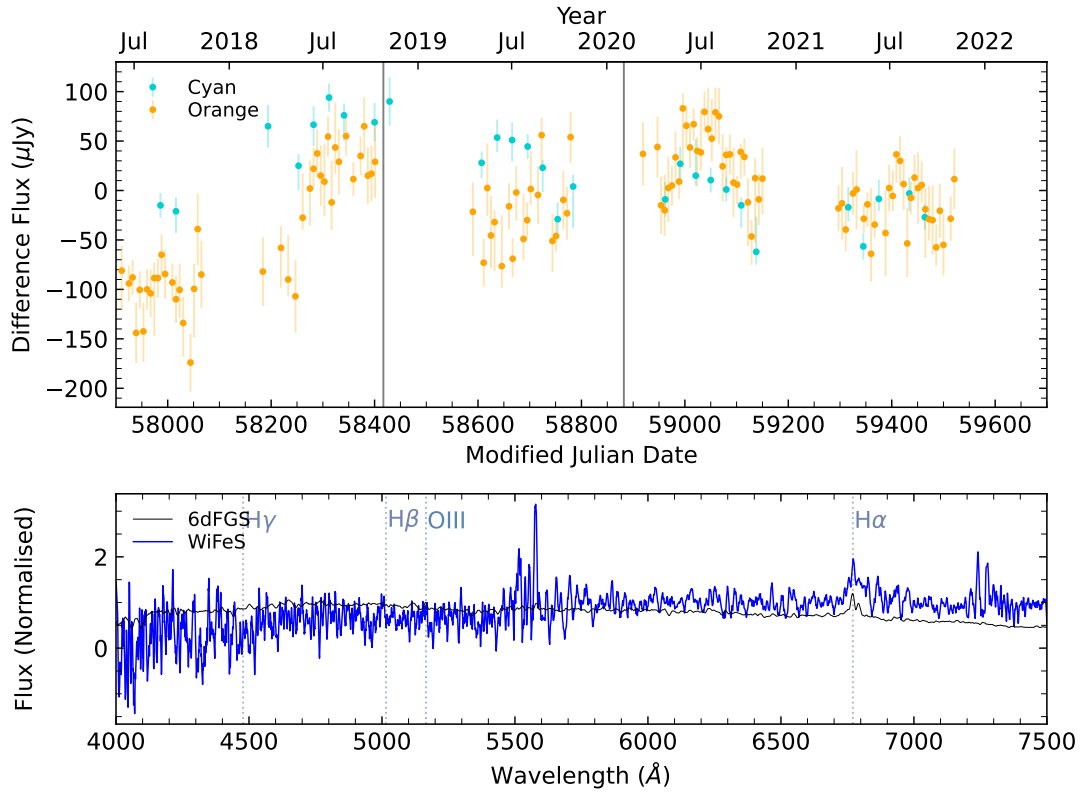ATLAS lightcurve (top) and 6dFGS+WiFeS spectra (bottom) for **g1457221-401359** with **6dFAGN type-1.9**.

ATLAS lightcurve (top) and 6dFGS+WiFeS spectra (bottom) for **g1459014-423454** with **6dFAGN type-2**.

ATLAS lightcurve (top) and 6dFGS+WiFeS spectra (bottom) for **g1508046-424445** with **6dFAGN type-2**.

ATLAS lightcurve (top) and 6dFGS+WiFeS spectra (bottom) for **g1515380-440648** with **6dFAGN type-2**.

ATLAS lightcurve (top) and 6dFGS+WiFeS spectra (bottom) for **g1526342-402821** with **6dFAGN type-2**.

ATLAS lightcurve (top) and 6dFGS+WiFeS spectra (bottom) for **g1550338-254349** with **6dFAGN type-1.9**.

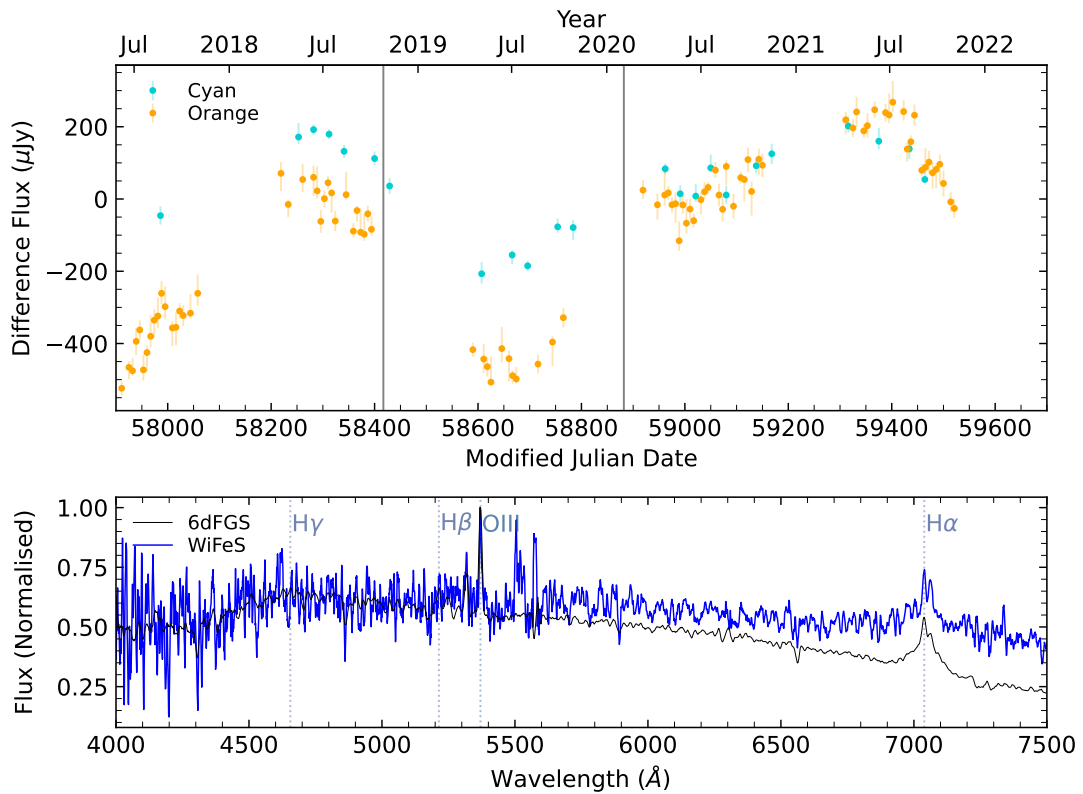ATLAS lightcurve (top) and 6dFGS+WiFeS spectra (bottom) for **g1554002-365535** with **6dFAGN type-1**.

ATLAS lightcurve (top) and 6dFGS+WiFeS spectra (bottom) for **g1556253-202829** with **6dFAGN type-1.9**.
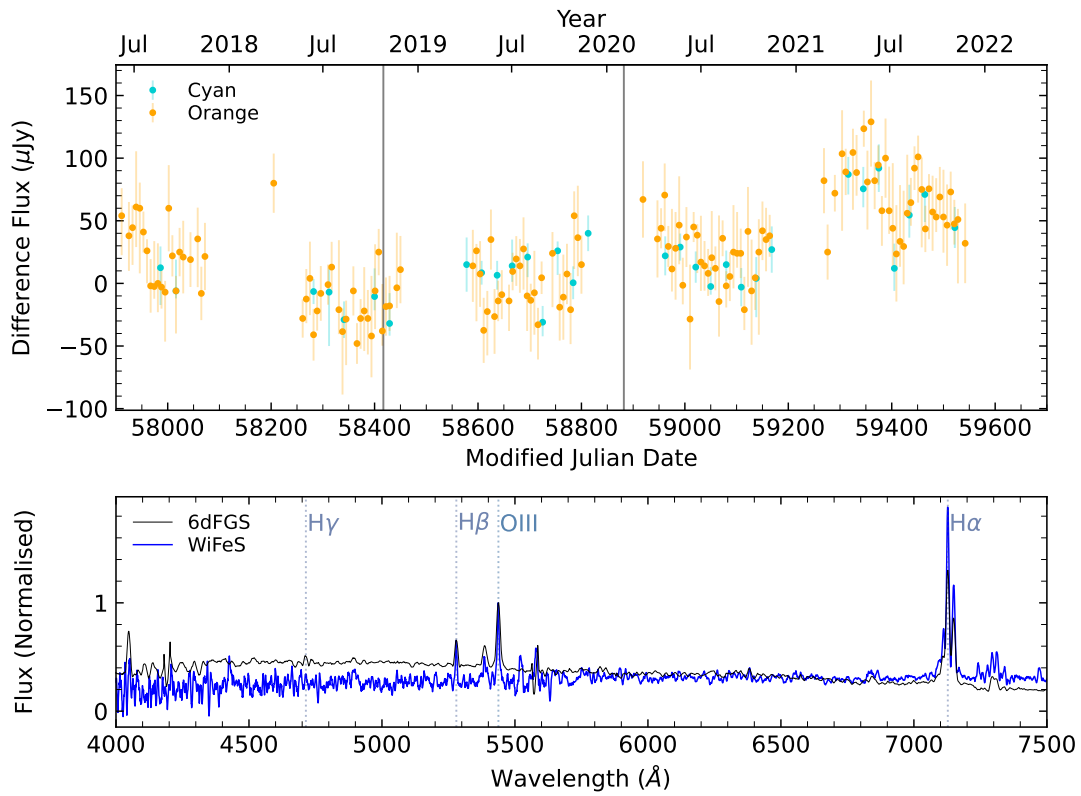
ATLAS lightcurve (top) and 6dFGS+WiFeS spectra (bottom) for **g1558468-320020** with **6dFAGN type-1.9**.

ATLAS lightcurve (top) and 6dFGS+WiFeS spectra (bottom) for **g1636268-211835** with **6dFAGN type-1.2**. Confirmed cross talk (see Table 2.1).

ATLAS lightcurve (top) and 6dFGS+WiFeS spectra (bottom) for **g1646104-112404** with **6dFAGN type-1.5**.
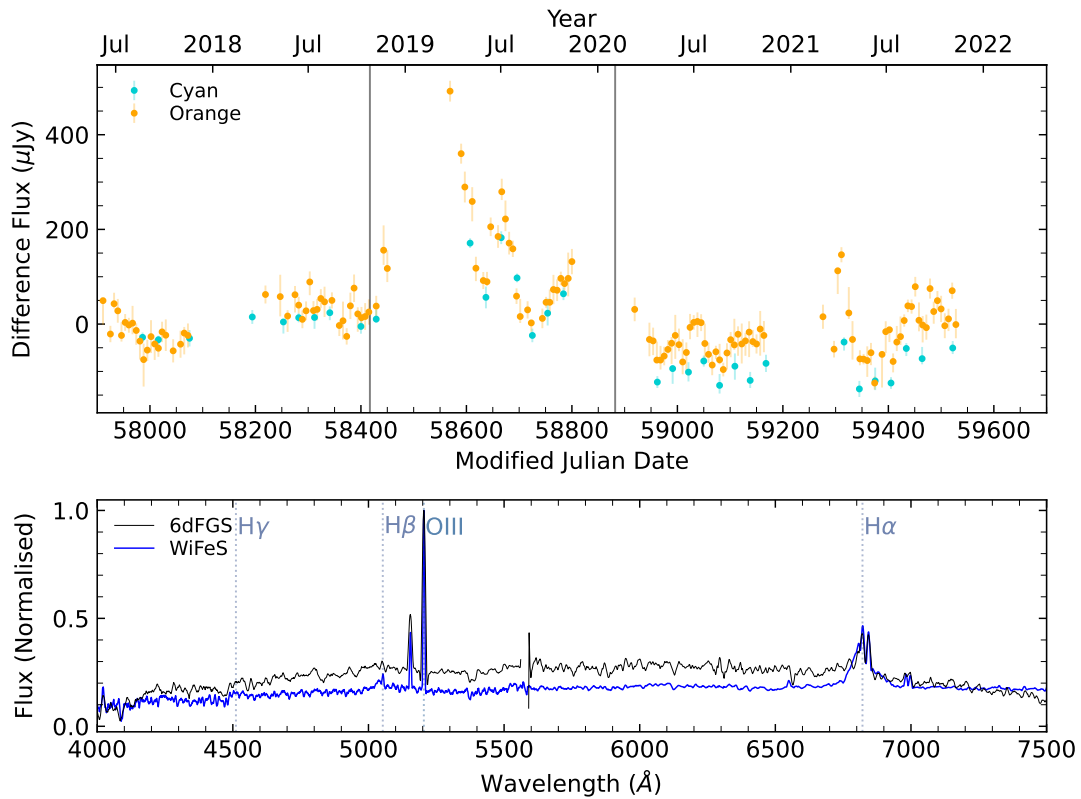

ATLAS lightcurve (top) and 6dFGS+WiFeS spectra (bottom) for **g1658419-031417** with **6dFAGN type-1.9**.

ATLAS lightcurve (top) and 6dFGS+WiFeS spectra (bottom) for **g1700567-030646** with **6dFAGN type-1.9**.
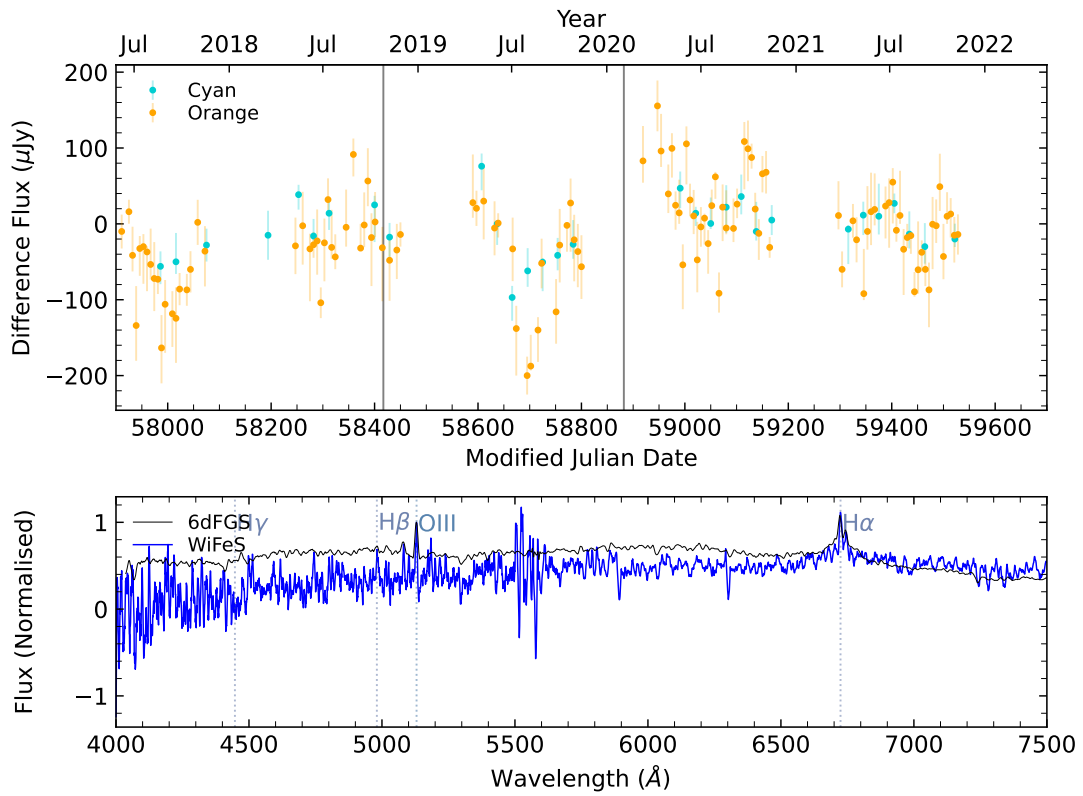

ATLAS lightcurve (top) and 6dFGS+WiFeS spectra (bottom) for **g1703359-101227** with **6dFAGN type-2**.

ATLAS lightcurve (top) and 6dFGS+WiFeS spectra (bottom) for **g1709224-014012** with **6dFAGN type-2**. This is a cross-talk candidate, but this object was not in our cross-talk list as we only searched for cross-talk in 6dFAGN types 1-1.9.

ATLAS lightcurve (top) and 6dFGS+WiFeS spectra (bottom) for **g1721290-070956** with **6dFAGN type-2**.

ATLAS lightcurve (top) and 6dFGS+WiFeS spectra (bottom) for **g1902376-375847** with **6dFAGN type-1.9**.

ATLAS lightcurve (top) and 6dFGS+WiFeS spectra (bottom) for **g1907504-392332** with **6dFAGN type-1.9**.
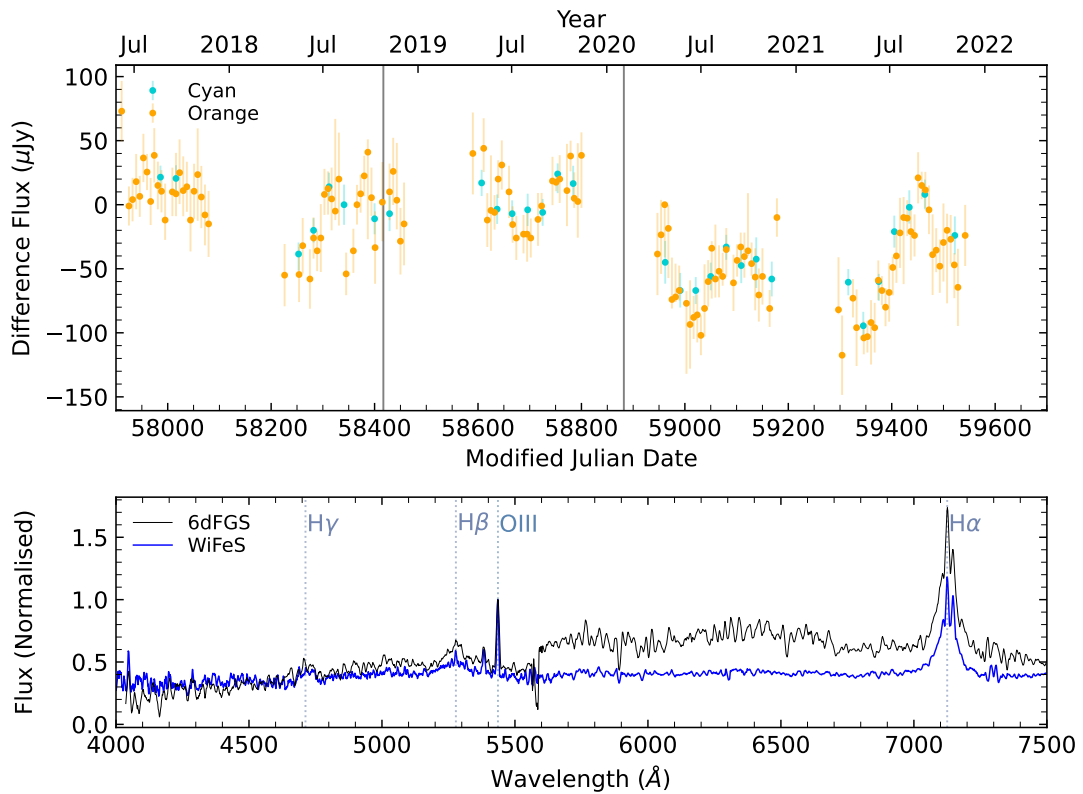
ATLAS lightcurve (top) and 6dFGS+WiFeS spectra (bottom) for **g1920272-162915** with **6dFAGN type-1.9**.
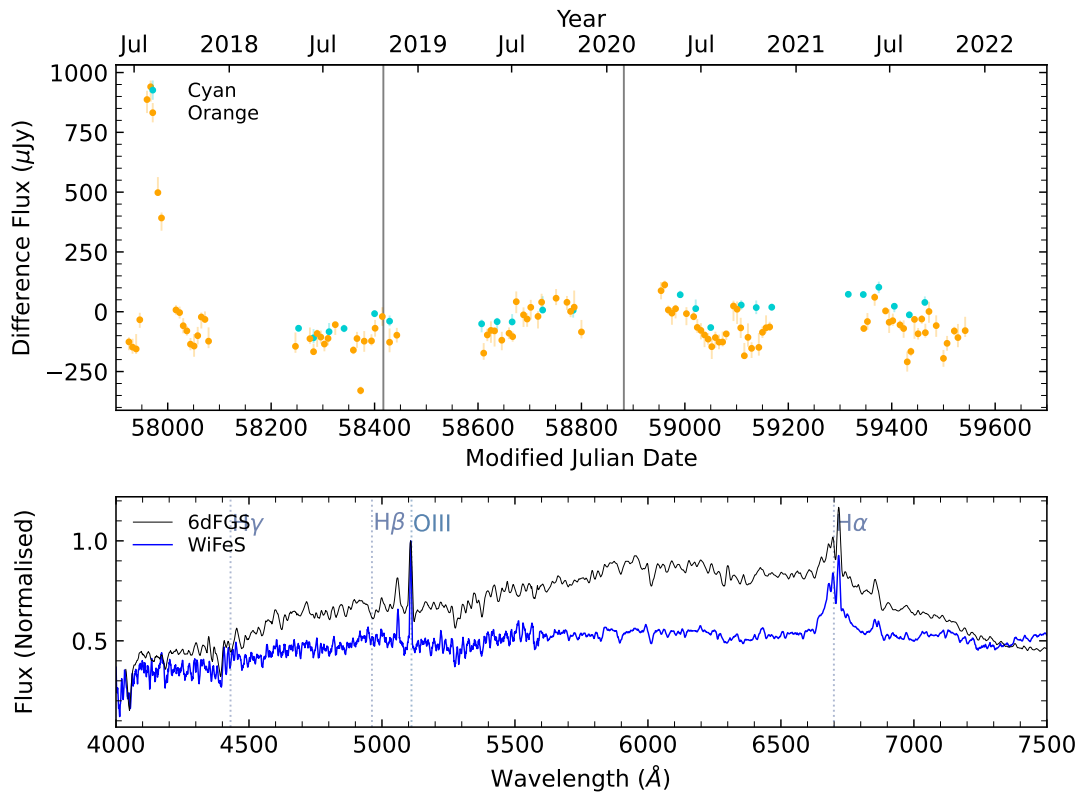

ATLAS lightcurve (top) and 6dFGS+WiFeS spectra (bottom) for **g1922540-185543** with **6dFAGN type-2**.
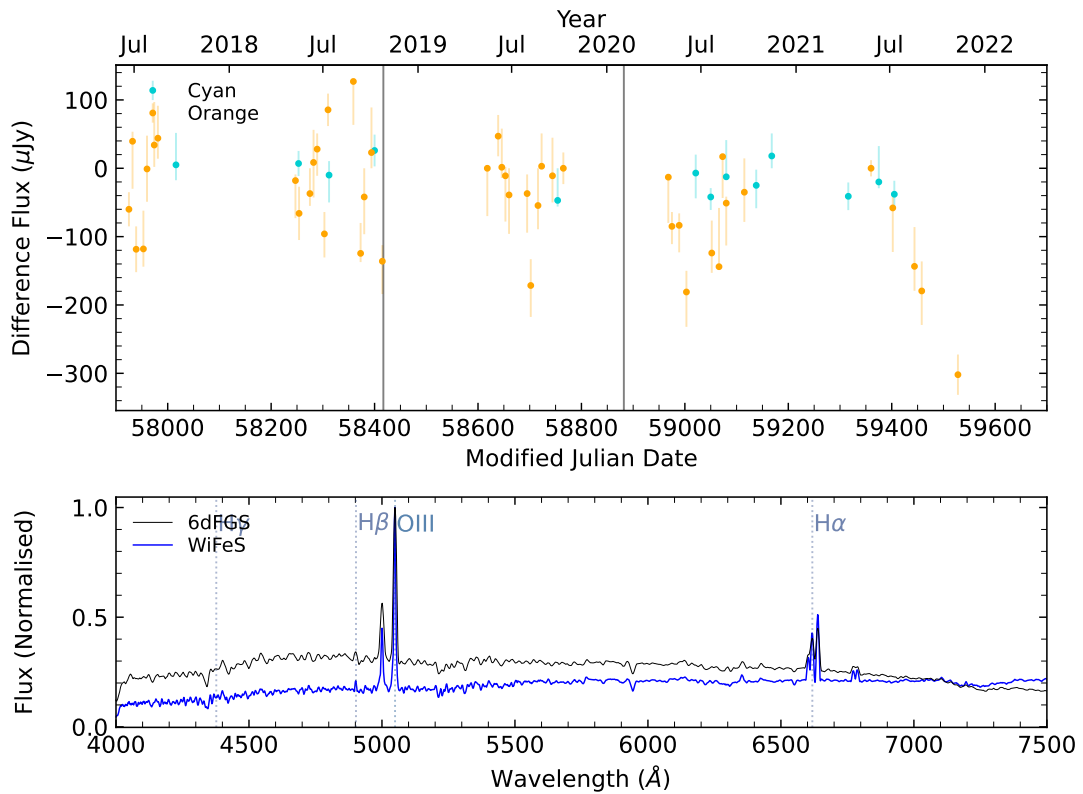
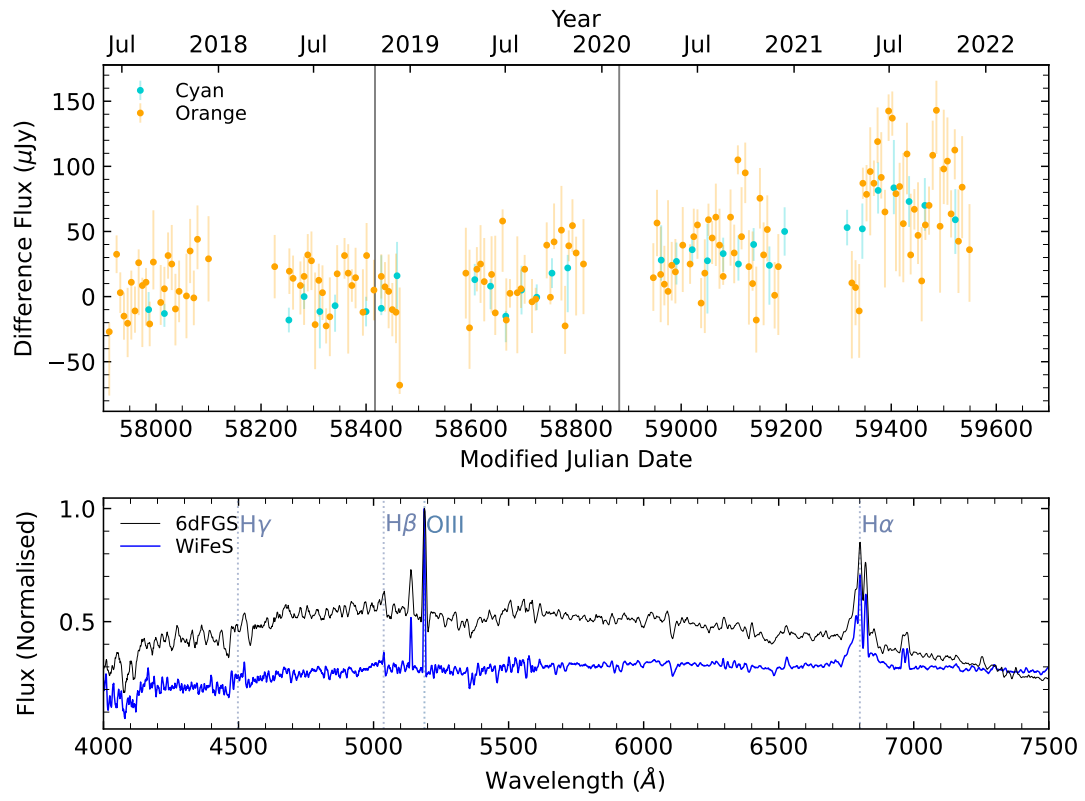ATLAS lightcurve (top) and 6dFGS+WiFeS spectra (bottom) for **g1944275-291211** with **6dFAGN type-1.9**.

ATLAS lightcurve (top) and 6dFGS+WiFeS spectra (bottom) for **g2010499-310931** with **6dFAGN type-1.9**.

ATLAS lightcurve (top) and 6dFGS+WiFeS spectra (bottom) for **g2015255-373043** with **6dFAGN type-2**.

ATLAS lightcurve (top) and 6dFGS+WiFeS spectra (bottom) for **g2018181-444825** with **6dFAGN type-2**.

ATLAS lightcurve (top) and 6dFGS+WiFeS spectra (bottom) for **g2038102-203149** with **6dFAGN type-1.9**.